EXPLORING THE CHEMISTRY OF METHOXIDE WITH OXYGEN THROUGH PHOTOELECTRON IMAGING SPECTROSCOPY

by

Christopher Charles Blackstone

A Dissertation Submitted to the Faculty of the

DEPARTMENT OF CHEMISTRY AND BIOCHEMISTRY

In Partial Fulfillment of the Requirements
For the Degree of

DOCTOR OF PHILOSOPHY

WITH A MAJOR IN CHEMISTRY

In the Graduate College of

THE UNIVERSITY OF ARIZONA

2020

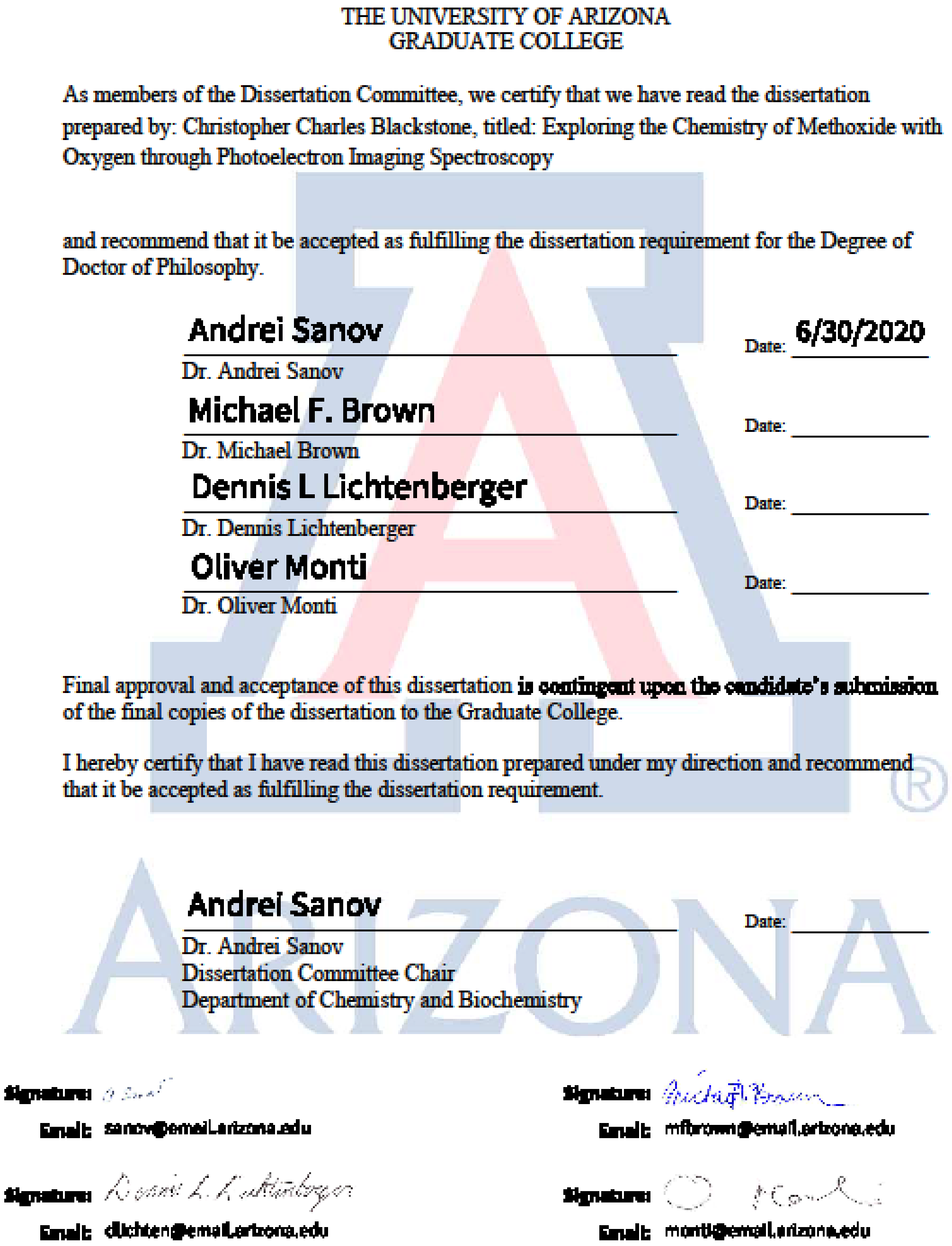

THE UNIVERSITY OF ARIZONA
GRADUATE COLLEGE

As members of the Dissertation Committee, we certify that we have read the dissertation prepared by: Christopher Charles Blackstone, titled: Exploring the Chemistry of Methoxide with Oxygen through Photoelectron Imaging Spectroscopy

and recommend that it be accepted as fulfilling the dissertation requirement for the Degree of Doctor of Philosophy.

Andrei Sanov
Dr. Andrei Sanov
Date: 6/30/2020

Michael F. Brown
Dr. Michael Brown
Date:

Dennis L Lichtenberger
Dr. Dennis Lichtenberger
Date:

Oliver Monti
Dr. Oliver Monti
Date:

Final approval and acceptance of this dissertation **is contingent upon the candidate's submission** of the final copies of the dissertation to the Graduate College.

I hereby certify that I have read this dissertation prepared under my direction and recommend that it be accepted as fulfilling the dissertation requirement.

Andrei Sanov
Dr. Andrei Sanov
Dissertation Committee Chair
Department of Chemistry and Biochemistry
Date:

Signature:
Email: sanov@email.arizona.edu

Signature: Michael F. Brown
Email: mfbrown@email.arizona.edu

Signature: Dennis L. Lichtenberger
Email: dlichten@email.arizona.edu

Signature:
Email: monti@email.arizona.edu

THE UNIVERSITY OF ARIZONA
GRADUATE COLLEGE

ACKNOWLEDGEMENTS

The pursuit of my PhD and the completion of the work in this dissertation was a long, often frustrating and arduous path. The support I had in completing it was invaluable, and I can say with certainty, that without the guidance, encouragement, and love of the people around me, the goal may have eluded me altogether.

First, I must acknowledge the National Science Foundation, who funded this work.

I would like to thank Professor Andrei Sanov, my research adviser. The open and welcoming discussions of group meetings—which were conducted without judgment so I could ask any question or make any proposal which occurred to me without embarrassment or regret—were invaluable in my learning about the methods we use, about chemistry and physics, and about the process of research in general. He gave me freedom to chase the projects which interested me, and to take them in the directions which most appealed to me, and joined me on even the most ambitious paths. But most importantly, he was present. He was always ready and willing to talk about anything which was bugging me; be it troubleshooting the instrument when it was down, making sense of data when their meaning was opaque, or encouraging and uplifting me during the many dark wells of plummeting confidence I fell into over the years. He was an excellent adviser, and I could ask for no one better. I am a better, more creative, more complete, and more confident scientist than I was when I started, by leaps and bounds.

I want to thank Lori Culberson for training me on the instrument and in this research in general, not only teaching me the technical details, but inspiring my interest in the work. I want to thank Dmitry Khuseynov, as well, for his mentorship in the group and

in the program, and for the very important advice to always keep this beard on my face so I don’t look like a child. I want to thank Adam Wallace for his near-constant presence to bounce ideas back and forth, and to vent our various frustrations, as well as his MATLAB mastery making all the work easier; and Yerbolat Dauletyarov and Beverly Ru, who were supportive co-workers, and with whom I’ve had conversations which deepened my own understanding of the work. All of you are my friends now, and I value each of you.

I want to further thank those who made the work possible at all; Kevin Bao and Justan Klaus, who repaired various broken electronics so the work could continue; Lee Macomber in the CBC machine shop, who repaired or made custom parts, and who taught me to machine some of them myself; the University machine shop, who prepared some other replacement parts integral to the completion of the work; Mikhail Ryazanov, who helped me understand run PyAbel despite no prior experience with Python; and Lori Boyd, who helped me navigate the specifics of completing the program when they were too confusing or overwhelming for me to handle on my own.

I want to thank my committee, Professors Oliver Monti, Dennis Lichtenberger, and Michael Brown, for their guidance and the fruitful discussions we have had, for their support through the PhD process, and for taking the time to read and evaluate this work. The last meeting we had before my defense was especially important, and I sincerely appreciate your investment in my success as a PhD student and as a scientist in general.

Professor Monti and Professor John Pollard also deserve specific acknowledgement for their role in shaping my philosophy as an educator and scientific communicator. Working with both of them on crafting new materials to shift the strategy of education from lecture and exercise to actual immersion in the material, and applying it to solve interesting problems, has taught me lessons I will carry with me if I remain as I am now on the academic path.

My personal support structure was also broad (and I am both sentimental and verbose, so keeping this section to a reasonable length is a legitimate challenge). The close friends I made early in my PhD, with whom I remain in touch even after they have graduated and moved away, and have helped to keep me going throughout the writing of this dissertation; the Pima Street Hockey League, who kept me in touch with my Northern origins through the sport; the Tucson Swing Dance Club community, who helped me overcome some elements of my social anxiety, and gave me yet another means of escaping the stress of science, especially Susan Brudos, who besides being a good friend with "bad" jokes, was a comforting presence when I needed it; the friends from college who were always willing to lend their ears to my troubles, especially Roma Panganiban and John Milligan; and the Oddballs softball team—especially Mark Ross, who invited me in the first place—who welcomed me (and eventually made me their manager, even) who gave me a much-needed outlet for my stress, and who surrounded me with relentless positivity (and some exciting championship seasons besides!). These friendships and these outlets kept me sane even at the height of my frustrations.

Some friends were especially valuable. The combination of escape and near-constant encouragement I have received from Zach Lachance, Andrew Dixon, Cody Corbin, Robb Bagge, and Ryan Eismin on the "Smash Chat" text message thread—and the Super Smash Bros. games the message group was originally made to coordinate—have turned stress to relief and even joy. Thank you to Marta Schoenle, who not only inspires me to bake increasingly ambitious treats (which my research group also appreciated, I think), but who was always ready with an understanding ear when something was bothering me, in particular during this stressful final phase of the work. Those friends with whom I have lived, Zach and Andrew first in the Hall of Justice, who gave me a warm home; and Paulina Ibarra, who gave me a second family in Tucson, and introduced me to the cat, Sawyer, who I now love (and who supplies the only worthwhile part of my limited social media presence, for whatever that is worth).

Finally, I want to thank my family, whose love for me and pride in me were bedrocks of my sanity and achievements. Mom and Dad, our weekly video calls grounded me, and kept me from losing sight of myself through the course of this work. Aunt Jean, your little notes of support were always encouraging. Patrick, you have been an excellent brother, who has given me opportunity to talk things out or simply have a laugh. Thank you to all of you, and to the rest of my family and friends who are not listed here specifically. Every one of you was integral in the completion of the work described in this dissertation.

DEDICATION

To Mom and Dad, who, to quote Fred Rogers, have "loved me into being." Your support and encouragement of me and pride in me have made the man I am, the man who was able to complete this work.

In loving memory of Pappy, my memories of whom are among my earliest and happiest.

In loving memory of Grandma, a model of love without nonsense, and who taught me a new word every day for years. I most vividly remember the day you taught me "tenacious," and it seems a fitting word to remember right now.

TABLE OF CONTENTS

CHAPTER 3:

CHAPTER 6:

LIST OF FIGURES

LIST OF TABLES

ABSTRACT

In this dissertation, photoelectron imaging spectroscopy is employed to probe the gas-phase chemistry between methoxide (CH_3O^-) and oxygen, including evidence of previously unexplored reaction paths and providing further insight into the fundamentals of chemical bonding. First, the known reaction of CH_3O^- and O_2 to produce the hydroperoxide anion (HO_2^-) is leveraged to investigate the photoelectron angular distributions as a function of electron kinetic energy, corresponding to photodetachment to each the ground $X\ ^2A''$ and excited $A\ ^2A'$ electronic states of the neutral HO_2 radical. These are modeled with the *p-d* variant of the generalized mixed-character model, and the results are compared to O_2^- and NO^- to gain insights into the effect on electronic structure of the breaking of molecular symmetry through the addition of a new bond. The results are also compared to predictions based on the qualitative *s*&*p* symmetry model—which reduces the properties of a molecular orbital to its symmetry character only—in order to further elucidate the role of symmetry in photoelectron angular distributions. Second, evidence of novel chemistry between methoxide and oxygen is presented, as the photoelectron spectrum corresponding to detachment from the formate anion (CHO_2^-) is reported. The agreement of both the spectral information and the photoelectron angular distribution with previous work done on the system confirms the identity of the anion, and introduces evidence of previously unknown chemistry by which CHO_2^- is formed by a reaction between CH_3O^- and O_2. Finally, further evidence of this novel chemistry is explored through interrogation of the anionic species which appeared in the mass spectrum at a mass-to-charge ratio of 63 amu, corresponding to a molecular formula of $CH_3O_3^-$. The identity of this molecule is not unambiguously assigned in this work, but

the existence of a bound structure with this molecular formula consequent of the interaction between methoxide and oxygen provides significant insight into an otherwise unknown reaction path. Future directions both to build on this work and to improve of the experimental apparatus are presented in the final chapter.

CHAPTER 1: INTRODUCTION

The diverse chemistry of the atmosphere is a rich source of both academic and practical interest. It is an ever-changing chemical environment through the interplay of natural processes, industrial pollution, and conscious efforts to mitigate environmental harm. While a large share of the public consciousness focuses on the trapping of heat by greenhouse gases leading to Climate Change, this is far from the only global effect caused by the emission of pollutant molecules. The same molecules which drive the warming of the planet also participate in chemistry which produces acid, which falls into lakes and onto farmland with rainwater, or toxic molecules like ozone in the troposphere affecting public health, or simply perturbing the natural reaction cycles in which the atmosphere is constantly engaged.

In this work, we focus on a very narrow slice of these myriad chemistries, looking at the reactions between methoxide (CH_3O^-) and molecular oxygen. Methoxide is a simple case of oxygenated volatile organic compounds (OVOC), and understanding its chemistry in full can give insight into how similar, but possibly more complex, molecules might behave when introduced into the atmosphere. We pursue this chemistry through negative ion photoelectron imaging spectroscopy, a powerful technique for assessing the properties of unstable neutral molecules, also providing information about the electronic structure of the parent anion. A survey of the time-of-flight mass spectrometry (TOF-MS) we use to isolate and target the ion of interest can also provide insight into the chemistry we explore.

This introduction is separated into three parts. First, we set up the chemical problem, outlining what is known about the chemistry of methoxide and molecular oxygen. Second, we detail the pertinent experimental and fundamental aspects of photoelectron spectroscopy in general and photoelectron imaging in particular. Finally, we discuss the history and concepts underpinning the analysis of photoelectron angular distributions (PADs). Altogether, this Introduction sets the stages for the specific experimental and theoretical studies discussed in the rest of the dissertation.

1.1 Chemistry of Methoxide and Molecular Oxygen in the Atmosphere

Methoxide and its neutral counterpart, the methoxy radical (CH_3O), play important roles as organic atmospheric pollutants.[1-6] They also serve as the simplest examples of their respective classes of species—alkoxides (RO^-) and alkoxy radicals ($RO^\bullet$)—which gives them interest in modeling a wide range of relevant chemistry. The methoxy radical can be produced either by the photodissociation of the O–H bond of methanol, or attachment of an oxygen atom to a methyl radical. Methoxide can be produced through either deprotonation of methanol or dissociation of species such as $CH_3CO{-}^{-}CO$. These species can further react to form peroxides and carbonyls, which in turn participate in further atmospheric chemistry.

It is well known that methoxy radicals in the atmosphere can react with oxygen to form hydroperoxy radicals (HO_2) and formaldehyde (CH_2O) by a hydrogen abstraction mechanism[7,8], described by the reaction:

$$CH_3O^\bullet + O_2 \rightarrow HO_2^\bullet + CH_2O \qquad (1.1a)$$

The analogous reaction with the methoxide anion proceeds by hydride transfer to produce hydroperoxide anions and formaldehyde:[5,9]

$$CH_3O^- + O_2 \rightarrow HO_2^- + CH_2O \quad (1.1b)$$

In each the neutral and the anion reaction, this process is slow—with rate constants at 298 K on the order of 10^{-15} cm^3 s^{-1} for the neutral,[2] and for the anion, 10^{-12} cm^3 s^{-1} on the triplet surface and 10^{-10} cm^3 s^{-1} on the singlet surface[9]—but it remains the dominant mechanism for loss of CH_3O/CH_3O^- in the atmosphere. Known alternate chemistry of the methoxy radical include isomerization and unimolecular decomposition, appearing in reactions 1.2a and 1.2b, respectively[8]:

$$CH_3O^\bullet \rightarrow {}^\bullet CH_2OH \quad (1.2a)$$

$$CH_3O^\bullet \rightarrow CH_2O^\bullet + H \quad (1.2b)$$

The product of the isomerization in Eq. 1.2a is likely to rapidly engage in a similar hydride transfer reaction to that in Eq. 1.1a. However, aside from scattered computational efforts, the potential energy surfaces of methoxy radicals with oxygen, and especially methoxide anions with oxygen, remain poorly understood[5,8], and the identities of alternate reaction paths are largely unexplored.

Given the typical mechanistic complexity of reactions in the atmosphere, it seems likely there are alternate channels for methoxide to be oxidized by molecular oxygen. The comprehensive computational survey of the $CH_3O^- + O_2$ potential energy surface indicates a number of stable intermediates and possible products, each for reaction of methoxide with the ground $X^3\Sigma_g^-$ and the excited $A^1\Delta_g$ states of oxygen by Lin, *et al,* in 2012[5], but so far there has been little computational and virtually no experimental follow-up.

The combination of the varied chemistry possible in the source chamber of our TOF-MS and the intrinsic ability of negative ion photoelectron spectroscopy to access metastable, transient intermediates provides an opportunity to push the boundary of what is currently known about the oxidation of methoxide by molecular oxygen.

1.2 Overview of Negative Ion Photoelectron Imaging Spectroscopy

The foundational principle of photoelectron spectroscopy is the photoelectric effect[10], measuring the kinetic energy of photoejected electrons, and giving insight into the electronic structure of the remaining molecule. In the case of photodetachment from a negative ion, the spectrum accessed corresponds to the remaining neutral core, often giving access to unstable species via their corresponding stable or metastable anions.

A negative ion in the ground electronic and vibrational state absorbs a photon of known, sufficient energy to detach an electron to the translational continuum, leaving a neutral molecule in some electronic and vibrational state. By conservation of energy, the kinetic energy of the electron and the energy required to remove the electron must sum to the photon energy, i.e.

$$h\nu = \varepsilon + \mathrm{eBE} \tag{1.3}$$

where ε is the kinetic energy of the photodetached electron and eBE is the electron binding energy[10]. The eBE spectrum corresponds necessarily to states of the neutral molecule, giving access to a full electronic spectrum of the neutral molecule, as diagramed in Figure 1.1.[11]

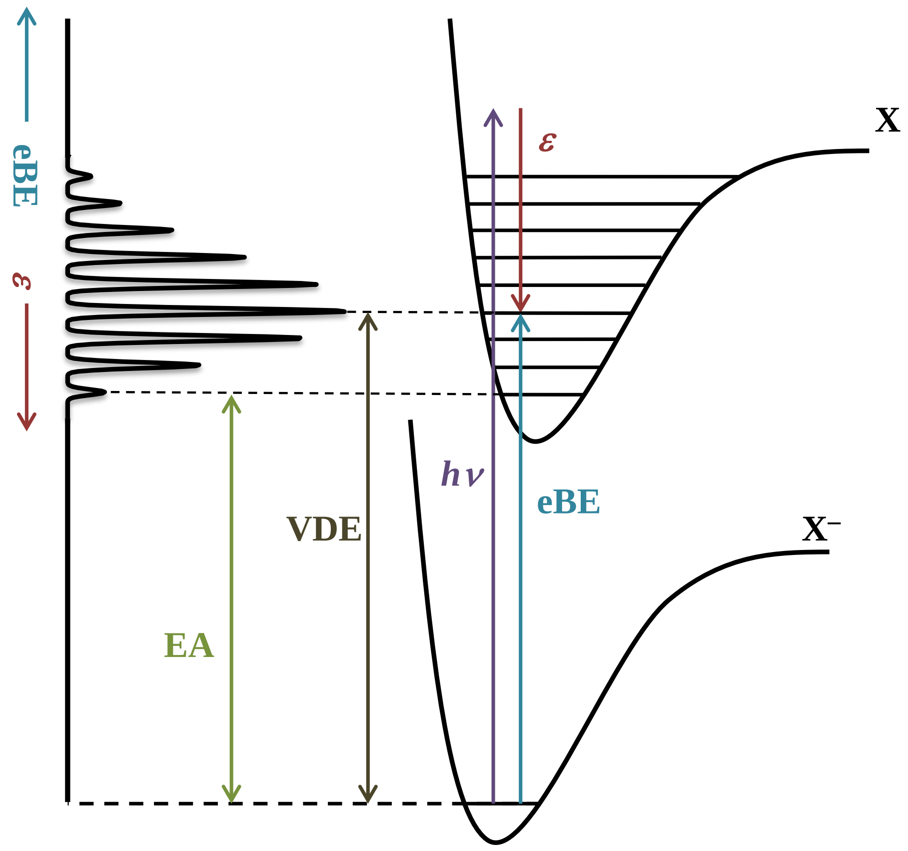

Figure 1.1. Schematic outline of photoelectron spectroscopy. A photon of energy $h\nu$ (purple) is absorbed by negative ion, X^-, in its ground electronic and vibrational state, leading to photodetachment of an electron with kinetic energy ε (red), corresponding to the difference between the photon energy and the energy required to access the state of the neutral molecule (X), eBE (blue), i.e. $h\nu$ = eBE + ε. The adiabatic electron affinity, EA (green), corresponds to detachment to the ground vibrational state of the neutral molecule, and the vertical detachment energy, VDE (tan), corresponds to detachment to the vibrational state of the neutral with the greatest Franck-Condon overlap with the ground vibrational state of the anion. The corresponding photoelectron spectrum appears rotated to its side to the left.

The electrons are also photoemitted with preferential directions with respect to the electric field vector of the photon, governed by the nature of the parent molecular orbital. This photoelectron angular distribution (PAD) can be used to give insight into that parent orbital[12,13], to make assignment decisions in the photoelectron spectrum, etc. The analysis of PADs will be developed in some detail in section 1.3. One of the key advantages of photoelectron imaging over other photoelectron spectroscopy detection techniques, though, is the complete detection of all angular information in a single image.

Chandler and Houston developed the first gas-phase charged particle imaging technique in 1987[14], and its resolution was drastically increased in 1997 with the development of velocity map imaging (VMI) by Eppink and Parker[15,16]. Thereafter, the fields of photoelectron and photofragment-ion imaging expanded widely, proving powerful tools for a variety of research interests[17-21]. The application of photoelectron imaging to negative ions gained traction in the early 2000s[22,23], and has continued to grow since, accessing diverse understandings of myriad types of systems.

1.3 Generalized Mixed Character Model for Photoelectron Angular Distributions

The outgoing free electron waves reflect the properties of electronic states of both the parent anion and the resulting neutral molecule[12,13]. Within the molecular-orbital approximation, the photoelectron angular distributions (PADs) reflect the properties of the parent anion’s orbital from which the electron was photoejected. In the case of anion photodetachment, the remaining neutral core interacts weakly with the photodetached electron[24], removing a complicating factor in probing the anion orbitals through analysis of the angular distribution of the outgoing electron. In this section, we explain how PADs are modeled, starting with the Cooper-Zare equation based on the central-potential model—applicable to detachment from atomic orbitals—and ending with the development of the Generalized Mixed Character Model developed in our group. The latter model describes photodetachment from molecular orbitals as photodetachment from a model function expanded in the basis set of atomic orbitals.

For one-photon photodetachment using linearly polarized light, the PAD is described by[25]

$$\sigma'(\theta) = \left(\frac{\sigma}{4\pi}\right)[1 + \beta P_2(\cos\theta)] \tag{1.4}$$

where θ is the angle between the photoelectron velocity vector and the photon electric field vector, σ is the total photodetachment cross section, σ' is the differential cross section with respect to the solid angle, $\sigma'(\theta) = \frac{\partial\sigma}{\partial\Omega}$, where $\partial\Omega = \sin\theta d\theta$, $P_2(\cos\theta)$ = $(1/2)(3\cos^2\theta - 1)$ is the second-order Legendre polynomial, and β is the anisotropy parameter, with values ranging from −1 (for fully perpendicular transitions) to 2 (for fully parallel). The values of β completely describe the photoelectron angular distribution.

For detachment from atomic anions, for which l is a good quantum number, the anisotropy will be determined by the interference of the $l + 1$ and $l - 1$ outgoing waves in accordance with the electric-dipole selection rule $\Delta l = \pm 1$ for atomic transitions. The derivations of Bethe[26], generalized by Cooper and Zare[27,28], give the Cooper-Zare central-potential formula:

$$\beta_l = \frac{l(l-1)\chi_{l,l-1}^2 + (l+1)(l+2)\chi_{l,l+1}^2 - 6l(l+1)\chi_{l,l+1}\chi_{l,l-1}\cos\delta_{l+1,l-1}}{(2l+1)\left[l\chi_{l,l-1}^2 + (l+1)\chi_{l,l+1}^2\right]} \tag{1.5}$$

where $\chi_{l,l\pm 1}$ are the magnitudes of the radial transition dipole matrix elements for the $l \pm 1$ partial waves consequent of photodetachment from the parent orbital described by the orbital angular-momentum quantum number l, and $\delta_{l+1,l-1}$ is the phase shift resulting from the interactions of the $l + 1$ and $l - 1$ outgoing waves with the remaining neutral species. Using the approximation of Hanstorp, *et al.*[24], which assumes the Wigner-law[29] scaling of the partial-wave cross-sections, the Cooper-Zare equation for detachment from negative ions can be rewritten explicitly as a function of electron kinetic energy, ε:

$$\beta_l(\varepsilon) = \frac{l(l-1)+(l+1)(l+2)A_l^2\varepsilon^2-6l(l+1)A\varepsilon\cos\delta_{l+1,l-1}}{(2l+1)\left[l+(l+1)A_l^2\varepsilon^2\right]} \tag{1.6}$$

where A_l gives the relative scaling of the outgoing $l + 1$ and $l - 1$ waves, defined according to the Wigner law as[24,29]:

$$A_l^2\varepsilon^2 = \frac{\chi_{l,l+1}^2}{\chi_{l,l-1}^2} \tag{1.7}$$

While the Cooper-Zare equation is rigorously correct only for atomic systems, for which the potential is spherically symmetric and l is a good quantum number[30,31], it has also been shown to perform well for detachment from anions whose orbitals sufficiently resemble atomic orbitals. One example is the "*d*-like" π_g^*-HOMO of O_2^-. The PADs in the photodetachment from this anion are famously well described by Eq. (1.6) with $l = 2$.[32-34] However, the Cooper-Zare equation cannot be used when treating photodetachment from molecular systems in general.

For decades after the publication of the Cooper-Zare central-potential formula in 1968, there was no experimentally-friendly formalism way to model the PADs in molecular-anion photodetachment in general. While many theoretical treatments of the problem have been developed,[35] despite their computational rigor, they did not provide the same level of straightforward conceptual insight as that given by the Cooper-Zare central-potential model in the case of atomic systems. In short, these treatments evaluate the complete three-dimensional PADs by directly computing the interactions of the anion with the light field and the overlap between the initial and final electronic states.

The first notable attempt to provide a *conceptual*, if not quantitative, insight in the PADs in molecular-anion photodetachment was made by our group in 2003 with the introduction of the *s*&*p* model[36]. This model described molecular-anion photodetachment by representing the outgoing free-electron waves as a superposition of symmetry-allowed spherical waves, and limiting the description to the $l = 0, 1$ (*s* and *p*) waves only. Although purely qualitative in nature, the *s*&*p* model was well received for the tutorial and pedagogical insights it provided. This model will be explored in more detail in Chapter 3.

The next conceptual and quantitative approach was initiated by our group in 2011, with the development of the first mixed-character model, specifically the *s*-*p* model[37]. The *s*-*p* model, while similar in name to the earlier *s*&*p* model, involved a different conceptual framework. While the *s*&*p* model considers the superposition of the symmetry-allowed free-electron *s* and *p* waves[36], it did not attempt to expand the parent molecular orbitals in any basis set. The mixed *s*-*p* model, meanwhile, launched us on the path of expanding the parent molecular orbitals as superpositions of atomic-like basis functions (*s*, *p*, etc.).[37,38] The photodetachment from each component of the parent MO is then treated in a manner consistent with the Cooper-Zare central-potential model, but the overall PAD is determined by considering the interference of the multiple pathways attributed to the different *l* components of the parent wavefunction.

The first application of the mixed *s*-*p* model was the description of the solvent-induced perturbation (polarization) 1*s* orbital of a solvated H^- anion, and the similar perturbation of the non-bonding N 2*p* orbital of solvated NH_2^-.[38] In the first case, the 1*s* orbital of H^- was augmented using a diffuse 2*p* polarization term attributed to the interaction with the solvent within the cluster. In the second, the distortion of the unperturbed 2*p* wavefunction was described by introducing a small (perturbative) *s* term. In both cases, the challenge was to adequately describe the initial state of the electron as a superposition of *s* and *p* functions, giving rise to the general mixed *s*-*p* treatment of the problem. Although in both of the above cluster cases the effect of the solvent on the parent electron orbitals could be viewed as a perturbation, the mixed *s*-*p* treatment that emerged from these projects was *non-perturbative* in nature. (The approximate nature of the treatment stemmed only from the fact that the mathematical expansions of the initial states were truncated to the *s* and *p* terms only.)

The non-perturbative nature of the mixed *s*-*p* model allowed for its seamless application to hybrid sp^x orbitals in organic systems. It was successfully applied to the σ systems of heterocyclic aromatic molecules, allowing for experimental probes of aromaticity and fractional hybridization character (x).[39-42]

For both cluster systems and heterocyclic aromatic, the mixed *s-p* model describes the PADs using the following expression for the anisotropy dependence on eKE:[37,43]

$$\beta_{sp}(\varepsilon) = \frac{2\left(1-\gamma_p\right)B_1\varepsilon+\gamma_p\left(2A_1^2\varepsilon^2-4A_1\varepsilon cos\delta_{2,0}\right)}{\left(1-\gamma_p\right)B_1\varepsilon+\gamma_p\left(1+2A_1^2\varepsilon^3\right)} \tag{1.8}$$

which should be compared to the Cooper-Zare equation (Eq. 1.6). In the mixed *s-p* model, Eq. 1.8, A_1 is the $l = 1$ case of the A_l parameter defined in Eq. 1.7 above, γ_p is the fractional *p*-character in the *s-p* model function:

$$\left|\psi_{sp}\right\rangle = \sqrt{1-\gamma_p}\left|s\right\rangle + \sqrt{\gamma_p}\left|p\right\rangle \tag{1.9}$$

and B_1 is the relative scaling of the $s \rightarrow p$ and $p \rightarrow s$ photodetachment channels, defined as:

$$B_1\varepsilon = \frac{\chi_{0,1}^2}{\chi_{1,0}^2} \tag{1.10}$$

The empirical observation can be made that, at least for the *s-p* case, the equation can be broken down into the sum of the Cooper-Zare numerators for $l = 0$ and $l = 1$ divided by the sum of Cooper-Zare denominators for $l = 0$ and $l = 1$. We have later demonstrated this to be true, in general, for any molecular orbital expanded as a superposition of atomic orbitals.[44] That is, for a model function expressed in the form:

$$|\psi_{MO}\rangle = \sum_l \sqrt{\gamma_l}|l\rangle \tag{1.11}$$

the anisotropy parameter, β, as a function of electron kinetic energy, ε, is expressed as[44]

$$\beta(\varepsilon) = \frac{\sum_l \gamma_l \upsilon_l}{\sum_l \gamma_l \omega_l} \tag{1.12}$$

where υ_l is the numerator of the Cooper-Zare central potential formula in Eq. 1.5:

$$\upsilon_l = \frac{l(l-1)\chi_{l,l-1}^2 + (l+1)(l+2)\chi_{l,l+1}^2 - 6l(l+1)\chi_{l,l+1}\chi_{l,l-1}\cos\delta_{l+1,l-1}}{2l+1} \tag{1.13a}$$

and ω_l is the denominator of the Cooper-Zare central potential formula in Eq. 1.5:

$$\omega_l = l\chi_{l,l-1}^2 + (l+1)\chi_{l,l+1}^2 \tag{1.13b}$$

Further, in the case of binary mixing between consecutive *l* quantum numbers, i.e.:

$$|\psi_{l-1,l}\rangle = \sqrt{1-\gamma_l}|l-1\rangle + \sqrt{\gamma_l}|l\rangle \tag{1.14}$$

we can apply the Hanstorp approximation to yield a convenient form of Eq. 1.12. First, we define:

$$\upsilon_l = \chi_{l,l-1}^2 V_l \tag{1.15a}$$

$$\omega_l = \chi_{l,l-1}^2 W_l \tag{1.15b}$$

where

$$V_l = \frac{l(l-1) + (l+1)(l+2)A_l^2\varepsilon^2 - 6l(l+1)A_l\varepsilon\cos\delta_{l+1,l-1}}{2l+1} \tag{1.16a}$$

$$W_l = l + (l+1)A_l^2\varepsilon^2 \tag{1.16b}$$

Further, we generalize Eq. 1.10 to apply to any *l*:

$$B_l\varepsilon = \frac{\chi_{l-1,l}^2}{\chi_{l,l-1}^2} \tag{1.17}$$

Using the definitions outlined in Eqs. 1.15-1.17, we can rewrite Eq. 1.12 for this binary mixing case as[44]

$$\beta_{l-1,l}(\varepsilon) = \frac{(1-\gamma_l)B_l\varepsilon V_{l-1}+\gamma_l A_{l-1}^2\varepsilon^2 V_l}{(1-\gamma_l)B_l\varepsilon W_{l-1}+\gamma_l A_{l-1}^2\varepsilon^2 W_l} \tag{1.18}$$

In addition to being able to probe the nature of anion molecular orbitals through the precise modeling of the PADs, the intuition about PADs the model provides can aid in other analysis, like assigning multiple electronic states in convoluted spectra, where anisotropy provides resolution the spectrum cannot.[45]

1.4 Conspectus of the Dissertation

The theme and goal of this dissertation is to explore both known and new methoxide oxidation chemistry in the presence of oxygen, both expanding and applying understanding of PADs developed in this group in recent years.

In Chapter 2, the experimental details are outlined. The instrument is described in detail, and the chemistry of ion generation is explained. The laser systems are described, and the means of selectively photodetaching from the ion of interest. Finally, the process of data analysis is described, from concepts to software.

Chapter 3 details the experiment on HO_2^-. The anion is generated using reaction 1.1b, and photoelectron images collected at eight wavelengths. The PADs are analyzed, and the anisotropy parameter, β, is plotted as a function of ε for detachment each from the HOMO and HOMO−1 of the anion, and modeled with the *p*-*d* case of the Generalized Mixed Character Model described in section 1.3 above. The results are compared to PADs from O_2^- and NO^- to explore how symmetry-breaking chemical differences are reflected in PADs.

In Chapter 4, previously unexplored chemistry is accessed, with a product of the reaction between methoxide and oxygen appearing in the TOF-MS with a mass of 63 amu. This system is imaged at four wavelengths, and the spectra compared to calculations. Two hypotheses for the identity of the molecule are made, and each the supporting evidence and the potential disqualifiers are discussed in detail for each of these proposed structures.

Chapter 5 explores the separation of the electronic states in the photoelectron spectrum of the formate anion by their PADs. Photoelectron images collected at 306 nm contain two nearly degenerate electronic states which cannot be resolved experimentally, but one state has a parallel PAD, and the other an isotropic PAD. Separating the spectrum into parallel and isotropic components can allow for the individual study of each of these states, with their assignments informed by our understanding of the connection between parent orbitals and the PADs consequent of detachment from them.

The dissertation is summarized in Chapter 6, and then preliminary results and other future directions are presented. The chapter contains discussions of superoxide adduct species, HO_3^-, HO_4^-, and HO_5^-, including TOF-MS evidence of producing HO_4^- and a weak photoelectron image of the species. A second question of the identity of a new molecule, generated at 62 amu, will also be explored, including photoelectron spectra at three wavelenghts, and a mass spectrometry experiment using CD_3OD. Third, a direction studying higher-mass products of methoxide—oxygen chemistry is proposed. Finally, there is discussion on the instrument modifications necessary to improve experimental resolution in order to probe these and other species in greater detail.

Ultimately, this dissertation aims to push the boundaries of the collective knowledge of gas-phase methoxide oxidation through the experiments completed, and well as providing future direction toward that goal.

CHAPTER 2: INSTRUMENTATION AND EXPERIMENTAL DESIGN

Described here in detail are the experimental methods consistent throughout all projects contained in this dissertation. The instrument has been described in detail elsewhere,[46,47] and is comprised of three main regions: the source chamber, in which ions are generated; the time of flight mass spectrometer (TOF-MS)[23], in which the ions are separated by mass; and the detection region, in which both the mass spectrum is collected and the ions of interest are explored by photoelectron velocity map imaging spectroscopy[14-16,19,22,23]. The entire instrument is held at varying levels of vacuum by differential pumping. A schematic of the instrument appears in Figure 2.1. Now we describe each section in detail.

2.1 Vacuum System

Each of the three sections of the instrument is kept at a different pressure through differential pumping, as demonstrated in Figure 2.1, with the source chamber connected to the TOF region by a 4 mm aperture, and the TOF region connected to the detection region by a 4” pneumatic gate valve through a 1” aperture.

During typical experimental operation, the source chamber is held at a pressure of 2-8 × 10^{-5} Torr by a 10" diffusion pump (Varian VHS-10, 3,650 L/s) backed by a Welch Duoseal Vacuum pump (model 1373). This latter pump is also used to evacuate the chamber and TOF region when they are vented to atmosphere for maintenance and experimental modifications. A pneumatic gate valve (Vacuum Research Ltd model LP10) is used to separate the diffusion pump from the chamber when the instrument is not in use, and the diffusion pump is turned off.

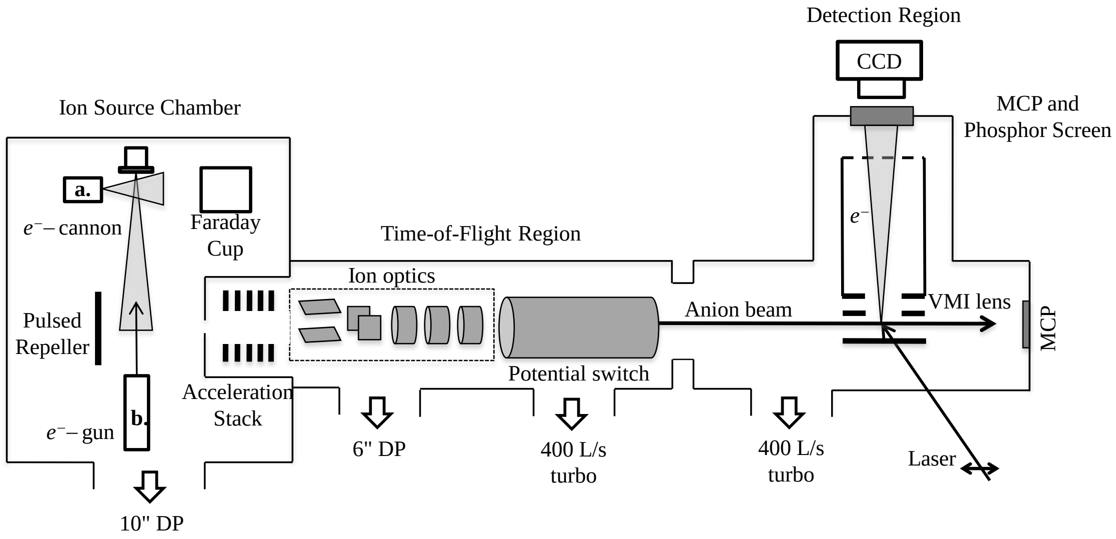

Figure 2.1. Schematic representation of the tandem TOF-MS photoelectron VMI used for all experiments detailed in this dissertation. The instrument was run with two different source chamber configurations, labeled a. and b. In setup a., an electron cannon is used to initiate the source chemistry, a diffuse wash of electrons passing perpendicular to the expansion over the face of the nozzle, with a grounded Faraday cup to catch the high kinetic energy electron cone out of the cannon. In setup b., an electron gun fires a focused beam of electrons parallel to the expansion at the face of the nozzle. The nozzle is grounded in both setups.

The TOF region is maintained at a pressure from 1-4 × 10^{-7} Torr by a 10" diffusion pump (Varian VHS-10, 3,650 L/s) backed by a Welch Duoseal Vacuum Pump (model 1397), as well as a turbomolecular pump (Oerlikon Leybold Turbotronik 361, 400 L/s) backed by a Leybold Trivac Mechanical Pump. A pneumatic gate valve (Chicago Allis Manufacturing, 6" model) is used to separate the diffusion pump from the TOF region when the instrument is not in use, and the diffusion pump is turned off.

The operating pressure of the detection region is 5-10 × 10^{-9} Torr, achieved by a turbomolecular pump (Oerlikon Lybold Turbotronik 361, 400 L/s) backed by the same Leybold Trivac Mechanical Pump used for the TOF region turbomolecular pump. The forelines to the mechanical pump from each turbomolecular pump are separated by a valve so the TOF region and the detection region can be vented separately, and the mechanical pump is used to evacuate each at the completion of repairs which require venting the region to atmosphere. When the instrument is not in use, the detection region is separated from the rest of the instrument by the aforementioned 4" pneumatic gate valve.

All diffusion pumps and turbomolecular pumps are water-cooled using a Neslab System 3 closed-loop liquid-to-liquid heat exchanger.

2.2 Source Chamber

A carrier gas, typically Ar, N_2O, or O_2 is flowed over a precursor sample contained in a stainless steel sample holder positioned just outside of the source chamber, and is pulsed into the chamber in a supersonic expansion through a solenoid-driven pulsed nozzle (Parker, General Valve Series 9 with a Kel-F poppet). Backing pressures of the carrier gas typically range from 15-30 psi, depending on the gas, and the nozzle is open with a 28 V square wave pulse over the solenoid with a width between 160 and 280 μs. This supersonic expansion is intersected at the source (roughly 2 mm from the nozzle orifice) by either a focused beam of high energy (1 keV) electrons from an electron gun or a diffuse wash of 0.1–0.5 keV electrons from an electron "cannon." Both the gun and cannon are described in detail in subsection 2.2.1.

At the intersection of the electrons and the expansion, a plasma is created, wherein the following chemistry begins.[48] High kinetic energy electrons collide with molecules and eject slower electrons. These slow electrons can then attach to neutral molecules, forming metastable negative ions and starting a cascade of chemistry by which anions of interest are formed. These negative ions can be stabilized by collisional extraction of energy (Eq. 2.1a), bond dissociation (dissociative attachment, Eq. 2.1b), or evaporative cooling (Eq. 2.1c), demonstrated in the chemical equations below:[48-51]

$$\mathrm{A} + \mathrm{e}^- + \mathrm{M} \rightarrow \mathrm{A}^{-*} + \mathrm{M} \rightarrow \mathrm{A}^- + \mathrm{M}^* \tag{2.1a}$$

$$\mathrm{MA} + \mathrm{e}^- \rightarrow \mathrm{MA}^{-*} \rightarrow \mathrm{A}^- + \mathrm{M}^* \tag{2.1b}$$

$$\mathrm{M}_n + \mathrm{e}^- \rightarrow \mathrm{M}_n^{-*} \rightarrow \mathrm{M}_{n-x}^- + x\mathrm{M} \tag{2.1c}$$

Further negative ion formation can be achieved through deprotonation (Eq. 2.2a) and H_2^+ abstraction (Eq. 2.2b) reactions when O^- radical anions are present in the system.

$$\mathrm{HA} + \mathrm{O}^- \rightarrow \mathrm{A}^- + \mathrm{HO}^\bullet \tag{2.2a}$$

$$\mathrm{H_2A} + \mathrm{O}^- \rightarrow \mathrm{A}^- + \mathrm{H_2O} \tag{2.2b}$$

In the work contained in this dissertation, all ions of interested are generated with the same precursor conditions: O_2 carrier gas at ~20 psig is flowed over a precursor of HPLC-grade methanol. The methanol is gently heated to ~40°C by heat tape wrapped around the sample holder, with current controlled by a variac.

2.2.1 Electron Gun and Electron Cannon

The electron gun and electron cannon are described in Figure 2.2. They work under nearly identical principles, with the distinction coming entirely from the presence of electron focusing optics in the gun, and their absence in the cannon. With focusing optics, a narrow, directed beam of electrons is produced, which must be aligned precisely with the origin of the expansion from the nozzle in order to produce the desired chemistry. The cannon offers less precision, but requires less optimization, as the electrons spray over a large area, nearly guaranteeing at least some of the desired chemistry occurring with less optimization. It is possible some new chemistry could be accessed through the cannon, since it offers easier variability of electron kinetic energy, but no such chemistry has been accessed at this point.

The electron cannon will be described first since it was built originally by merely removing the optics from the electron gun. Electrons are produced by heating a yttria- or thoria-coated iridium filament by running current over it from a Kepco 15-15M current supply. The electron glow is directed toward the interaction region by applying a negative potential to a cathode plate. Both the current supply and cathode power supply are floated to a potential between –100 and –1000 V by a Bertan 205B-03R power supply, and the cathode plate carries an additional potential between 0 and –200 V. The current run over the filament to produce an electron glow depends on numerous factors, including the float potential and the width of the filament. A 0.050"-wide ribbon filament requires between 10 and 15 A of current. A 0.028"-wide ribbon filament requires between 5 and 7 A of current. Higher float potentials require smaller current over the filament, while higher cathode potentials require higher current over the filament. A grounded washer could be

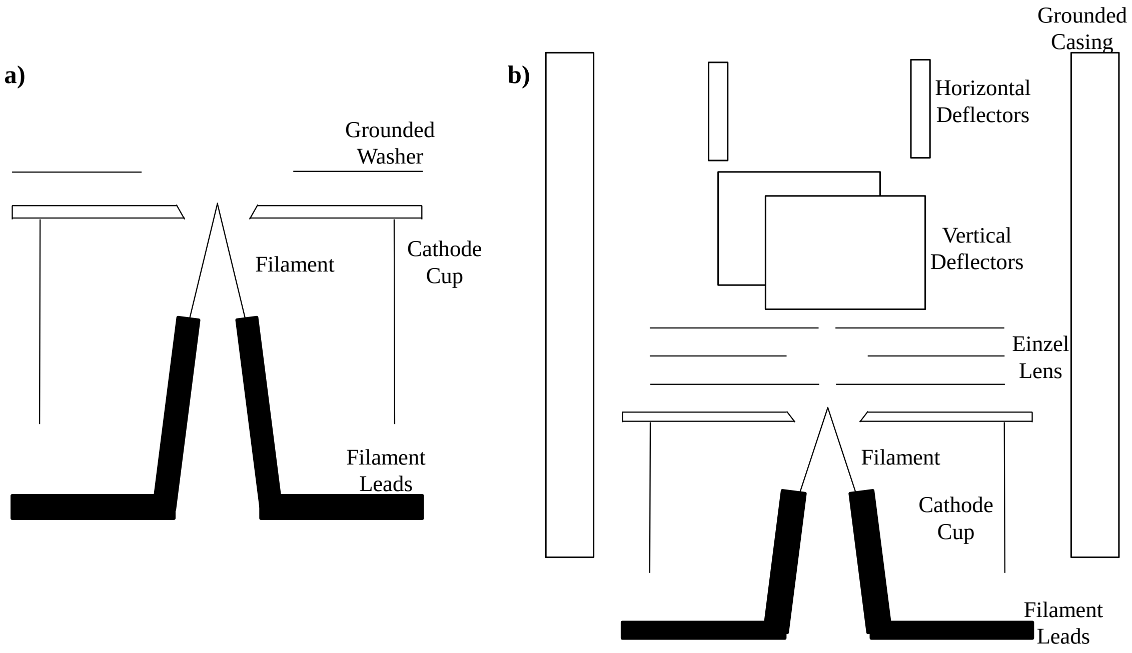

Figure 2.2. Line schematics of a) electron cannon, and b) electron gun. In each the gun and cannon, the filament and cathode cup are floated to the same potential. In the cannon, that potential varies from −100 V to −1000 V, whereas it is always −1000 V for the gun. The cathode cup then has an additional potential of 0 to -240 V applied to accelerate the electrons further. In the cannon, a grounded washer shields the expansion from the float potential of the cannon, and the nozzle from stray electrons. The gun is encased in a grounded shell. An Einzel lens with entrance and exit plates fixed to true ground, and a middle plate with floated to a potential of −500 V to −1200 V focuses the electrons into a beam, which is then directed toward the expansion by the two sets of deflectors.

placed near the cathode plate (~1 cm) to catch the widest edges of the electron output and reduce the heating of the nozzle, as well as blocking the ions produced in the expansion from the electric field produced by the cathode plate, but it was not a necessary piece, and no solid evidence exists either way on its effect on the experiment.

In the electron gun setup, the cannon is mounted into a grounded shell, where it is followed by a decelerating electron Einzel lens consisting of three electrodes. The outer two of these electrodes have 1 mm diameter apertures, and are held at true ground. The middle plate has a 1 cm diameter aperture, and holds an adjustable potential, typically between −500 V and −1200 V, produced by a Keithley 247 High Voltage power supply. After the electron beam is focused in the Einzel lens, two sets of deflectors—first vertical, then horizontal—direct the beam to the interaction region. An adjustable potential difference of 0 V to 135 V is put on each pair of plates by a pair of Agilent E3612A power supplies.

In the chemistry reported here, the chemistry accessed by each electron source appeared to be the same. In limited observation, the cannon seemed to more reliably produce greater numbers of ions, but the gun produced a much better resolved (more focused in time) TOF mass spectrum. Ultimately, we decided to return to the electron gun setup because the lifetime of filaments was considerably longer. Filaments lasted between two hours and one month, depending on various factors, in the electron cannon. In the gun setup, filaments lasted between one month and one year.

2.3 Time-of-Flight Mass Spectrometer

The negative ions formed in the expanding plasma are extracted by a pulsed repeller plate into a Wiley-McLaren[52] TOF-MS.[47,53] These ions are accelerated further with an acceleration stack, and the ion beam is directed by horizontal and vertical deflectors and focused with an Einzel lens. The ions are gated with a potential switch and pass through a field-free tube where they separate in time by mass to charge ratio.

Repeller plate voltages range from –200 to –800 V, adjusted to optimize ion focusing, and produced with a DEI PVM-4210 high voltage pulser (~10 ns rise time). The acceleration stack and all optics are encased in a metal casing floated to +1950 V with a 37 Hewlett Packard 6516A DC power supply. The acceleration stack consists of a series of 10 3" electrodes with 1" through-holes in the center connected in series by 1 MΩ resistors. The first plate is grounded, and the tenth plate is floated to +1950 V. The accelerated ions are directed by sets of each horizontal and vertical deflectors, which can be adjusted to ±135 V against the float voltage, and are operated by Agilent E3612A power supplies, also floated by the HP power supply. The ions are then focused by an ion Einzel lens consisting of three 1.5"×1.5" stainless steel electrodes, operated in a decelerating regime. The terminal electrodes are floated to +1950 V, and the middle electrode is varied between +500 to +1000 V with a Bertran Model 250B-03R power supply.

The ion beam is referenced to ground in a potential switch. The potential switch is a stainless steel tube floated to +1950 V by a DEI PVX-4140 high voltage pulser (~15 ns rise time), powered by the ion optics float power supply, when the repeller plate fires. It is then returned to ground after a 4-20 μs delay, depending on the mass of the ions of interest, referencing those ions to ground for their flight in the field-free tube.

The ions which pass through the potential switch gate are separated by mass to charge ratio in time in the field free tube before arriving at the ion detection region, where they strike the Chevron-type dual microchannel plate (MCP) detector.[23,46,47] The detector is separated from the TOF region by a grounded nickel mesh (33 lines/inch, 70% transmission, Buckbee-Mears, Inc.) to shield the ion beam from the potentials put on the detector. A split potential floats the detector by a Bertan 05B-03R power supply, typically applying 1 kV and 2.5 kV to the front and rear MCP plates, respectively, accelerating an electron cascade through the channels of the microchannel plates. This cascade strikes an anode floated to about 200 V above the back of the second MCP, generating the electric signal. The AC-coupled output is amplified ×100 by a Phillips Scientific Model 6931 amplifier, and read out by a Tektronix, Inc. 3032 oscilloscope, yielding a trace of ion intensity as a function of time.

In general, the mass-to-charge ratio, m/z, of any ion relates to time of flight, t_m, by Eq. 2.3:

$$\frac{m}{z} = \frac{(t_m - t_0)^2}{a^2} \tag{2.3}$$

where t_0 and a are calibration parameters. The former corrects for the start time of the experimental cycle on the oscilloscope, and is typically on the order of 0.2 μs. The a parameter collapses all factors in the construction and operation of the TOF-MS which determine the time of flight of a given ion into one calibration value. Its magnitude is typically on the order of 3 s/Da$^{1/2}$. These calibration parameters are determined through the identification of two known mass peaks, as shown in Eqs. 2.4a and 2.4b.

$$a = \frac{t_2 - t_1}{\sqrt{m_2 - m_1}} \tag{2.4a}$$

$$t_0 = t_1 - a \tag{2.4b}$$

Once the peak of interest is identified, the TOF-MS can be used to time a laser pulse to intersect that ion specifically, photodetaching an electron to be detected in the photoelectron VMI detector, the description of which follows.

2.4 Photoelectron Velocity Map Imaging Assembly

The axis of the photoelectron VMI assembly[15,16,54] is oriented perpendicular to the ion beam. The VMI lens (Figure 2.3) consists of three circular electrodes made of oxygen-free, high-conductivity copper. The plates are 4” in diameter, spaced 1” apart. The bottom plate is solid througout, while the middle and top plates have apertures 1” in diameter through which the electrons pass. The lens accelerates the photodetached electrons toward the detector, projecting the three-dimensional outgoing electron wave into two dimensions, and focusing all photoelectrons with the same velocity vectors to the same point on the detector, regardless of the *xy* position of the electron’s origin within the first VMI stage.

The bottom plate of the VMI is fixed at a potential between -110 V and 330 V, supplied by a Hewlett-Packard 6516A DC power supply, to extract electrons into the lens. The center plate is grounded. The top plate is floated to a potential of +300 V to +900 V, using a Bertan model 205B-03R power supply. The ratio of the top and bottom plate voltages is optimized to ensure maximum focusing—and, therefore, resolution—which is usually achieved at about a 2.7 top:bottom potential ratio. The voltages can be adjusted together, preserving the optimized ratio, to affect the size of the expansion projected on the detector; the smaller the voltages, the larger the image. Typically, images collected with lower VMI voltages have better resolution at the expense of detection efficiency.

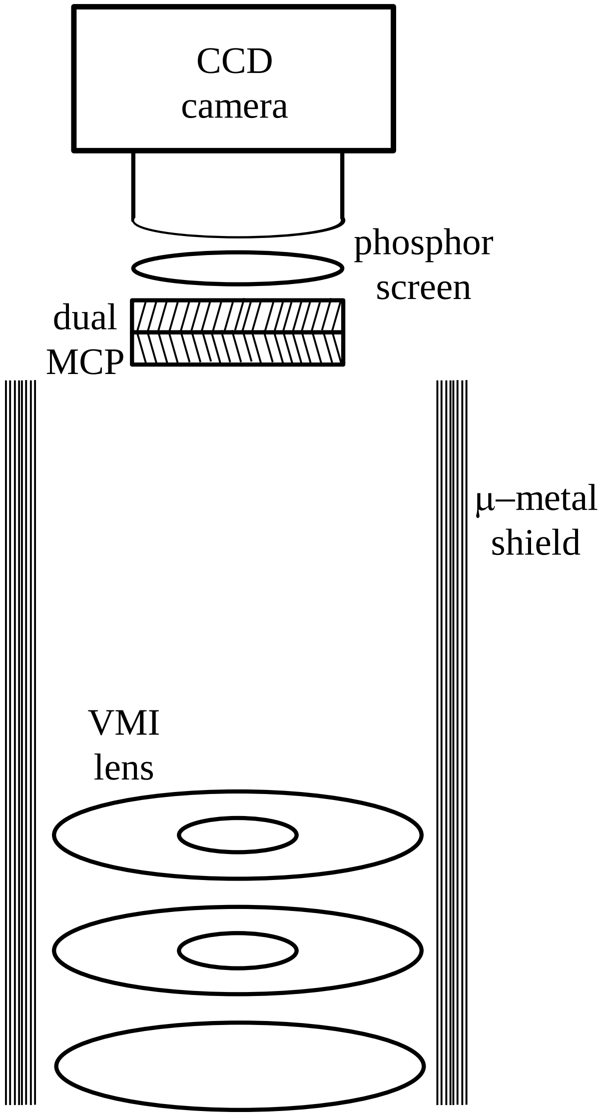

Figure 2.3. Schematic of the velocity map imaging detector. The VMI lens is constituted of three electrodes, floated to voltages of –110 V to –330 V for the bottom plate, 0 V for the middle plate, and +300 V to + 900 V for the top plate. The imaging assembly is encased in a μ–metal shield to protect it from external magnetic fields. The dual MCP amplifies the spatially-resolved photoelectron signal on collision, and the P47 phosphor screen converts the electron signal to photons, which are captured by the CCD camera.

The VMI lens is mounted in a tube encased by a μ-metal shield to protect it from external magnetic fields, floated to the same potential as the top electrode of the VMI assembly. The electrons traverse a field-free region from the top of the VMI lens to the photoelectron detector, shielded from the potentials on the detector by a nickel mesh (33 lines/inch, 70% transmission, Buckbee-Mears, Inc.) also floated to the top VMI plate potential.

Three main components comprise the detector: a dual-chevron MCP, a phosphor screen, and a CCD camera. The entrance of the first MCP is given a fixed 2.00 kV potential, and the exit of the second a fixed 3.00 kV potential by the divided 3.00 kV output of a Burle Model PF1054 power supply. There is a further 1.01 kV pulsed voltage applied to the exit MCP by a DEI PVM-4150 pulse generator during the 100-250 ns window over which the electrons arrive, increasing the potential across the two MCPs to 2.01 kV. The width of that pulse is optimized to maximize the signal to noise.

The MCP amplifies the electron signal, and that amplified signal strikes the P47 phosphor screen (Burle, Inc.) generating photons at the positions of impact, which are carried to an external window by a fiber optic bundle, where the image is collected by a CoolSnap HQ CCD camera (Roper Scientific), which is interfaced to a computer, the software of which will be described in Section 2.7.

2.5 Laser Systems

The experiments in this work were carried out using two separate laser systems: a Spectra Physics Quanta-Ray Lab 130-50 Nd:YAG, and a Continuum DCP6100 dye laser. Each system is described in detail in this section.

2.5.1 Nd:YAG Laser

A flashlamp-pumped neodymium-doped yttrium aluminum garnet (Nd:YAG) laser is used to generate four wavelengths. The fundamental output is 1064 nm, with an energy of 200 mJ/pulse, which can be frequency doubled to 532 nm (70 mJ/pulse) with a type II potassium dideuterium (KDP) crystal. This second harmonic can either be frequency mixed with residuals of the fundamental to generate the third harmonic output at 355 nm (30 mJ/pulse), or passed through a second KDP crystal and frequency doubled to 266 nm (15 mJ/pulse). The laser is Q-switched at 50 Hz with 10 ns output pulses.

2.5.2 Tunable Dye Laser

The dye laser output is produced by pumping an oscillator cell and two amplifier cells with the second harmonic of a Continuum Surelite II-20 Nd:YAG (532 nm, 270 mJ/pulse). The Nd:YAG is Q-switched at 20 Hz, with one nanosecond output pulses. The dye fluoresces a broad spectrum, with a single wavelength selected by the angle of a motorized diffraction grating.

Three dyes were used for this work. LDS 821 fluoresces in the range of 797 nm to 822 nm, with a peak output at 812 nm (40 mJ/pulse); Rhodamine 640 outputs in the range of 607 nm to 622 nm, with a peak at 612 nm (40 mJ/pulse); and Rhodamine 610 outputs a with a peak wavelength of 590 nm (40 mJ/pulse). The outputs from the two Rhodamine dyes can be frequency doubled with a DCC-1 doubling crystal, and the LDS 821 by a DDC-2 doubling crystal. The doubled Rhodamine 640 output peaks at 306 nm with an energy of 6 mJ/pulse; the doubled Rhodamine 610 at 295 nm (6 mJ/pulse), and the LDS 821 at 406 nm (2 mJ/pulse).

2.6 Pulse Timing

The experiment is controlled by two delay generators. One is a Stanford Research Systems Model DG535. The second was initially a Berkeley Nucleonics Corporation (BNC) Model 555, but was replaced with a BNC Model 575, which functioned identically in the experiment. The general pulse delay scheme is described elsewhere,[46] but here we address some small modifications made for this work.

The experiment with both lasers was triggered with the Stanford delay generator's internal timing. The flash lamps of the Nd:YAG were fired on the Channel A output of the Stanford delay generator, and the Q-Switch by Channel B, timed to the pulsing of the repeller plate. The Photoelectron detector VMI pulse was set by the Channel A output of the BNC delay generator, which was also referenced to the repeller plate pulse. This gave the advantage of neither the laser nor MCP timing changing when the repeller plate pulse timing was adjusted to optimize ion signal.

For triggering the dye laser, the MCP pulse and laser pulses had to be switched. The Channel A output of the BNC box signaled the flash lamps, its timing relative to Channel B, and Channel B fired the Q-switch, timed to the nozzle pulse. This allowed for easy control of the dye laser output power, which is determined by the delay between the lamps and the Q-switch. Setting the lamp output relative to the Q-switch directly permitted the laser timing to be adjusted directly without having to adjust the lamp timing separately to control the power. The MCP was driven off the Stanford delay generator Channel A, with Channel B setting the pulse width.

2.7 Data Collection and Analysis

The signal from the camera is processed by the Cool Image program.[55] Collection times varied from 1.25 to 5 minutes, depending on what collection time optimized background subtraction, with 5 second collection intervals. Background images were collected by changing the laser and MCP pulse timings by 100 ns, so the laser pulse passed through the detection region in between the arrival of ion packets of adjacent molecular mass. Background images were directly subtracted from photoelectron images of the ion of interest in the Cool Image program, and the background-subtracted images were summed until the desired signal to noise was achieved, typically in the range of 50-100 minutes of total collection time—on the order of 60,000-120,000 experimental cycles with the dye laser, or 150,000-300,000 experimental cycles with the Nd:YAG.

Raw photoelectron images correspond to a two-dimensional projection of the three-dimensional outgoing electron wave. The original three-dimensional distribution is recreated, and a cross section taken through the middle of that recreated distribution is taken using an inverse Abel transformation[19] carried out in the BASEX program.[56] From the Abel-inverted reconstructed image, the photoelectron speed distribution is generated. The angular distribution is analyzed in a MATLAB script written by Adam Wallace, based on the BetaCalc program,[55] which allows the user to identify peaks and choose the width over which each is integrated to determine anisotropy parameters for the full image at once.

CHAPTER 3: PHOTOELECTRON ANGULAR DISTRIBUTIONS OF HO_2^-:

The effect of symmetry-breaking chemical differences on photoelectron angular distributions in the context of the *p-d* case of the Generalized Mixed Character Molecular Orbital Model

3.1 Introduction

The hydroperoxy radical (HO_2) is as ubiquitous a molecule in atmospheric chemistry as there is, participating in myriad natural and pollutant-driven chemistry.[6] The corresponding hydroperoxide anion (HO_2^-) is an important intermediate in the solution-phase consumption of ozone, among other reactions.[57,58] Despite their clear and broad relevance—or, perhaps, because of it—and the extensive studies conducted on these species, their chemistry is not yet fully understood.

In this section, the relevance of these species and their various chemistries will be explored first, followed by a discussion of the fundamentals and history of the analysis of photoelectron angular distributions, (PADs) for photodetachment from negative ions, setting the stage for the analysis of the photoelectron imaging experiment on HO_2^-, as this work seeks not only to characterize another element of the electronic behavior of HO_2^-, but also to contribute to the academic understanding of PAD.

3.1.1 Chemical Relevance of the Hydroperoxy Radical and Hydroperoxide Anion

As discussed briefly in Section 1.1, HO_2 radicals are formed in the atmospheric oxidation of methoxy radicals (Eq. 1.1a)[7,8], while HO_2^- anions are formed in the oxidation of methoxide anions (Eq. 1.1b)[5,9].

In addition to the oxidation of alkoxy (RO) radicals, HO_2 is primarily formed through the reaction of carbon monoxide with hydroxyl radicals, photolysis of carbonyls, and oxidation of volatile organic compounds (VOCs) other than alkoxy radicals.[59] The hydroperoxy radical further engages in an array of important atmospheric cycles, including the production of secondary organic aerosols (SOAs) and tropospheric ozone, which have adverse impacts on public health; and the formation of OH radicals, which drive the oxidative capacity of the atmosphere.[6,59] This means HO_2 itself is a major driver of the oxidative capacity of the atmosphere, and understanding its chemistry is essential to understanding the atmosphere's complex network of reactions. Consequently, there is significant recent work on developing new methods for detecting and measuring its presence in the atmosphere, as well as understanding its chemistry to produce accurate models of its behavior.

The hydroperoxide anion, meanwhile, is produced through the deprotonation of hydrogen peroxide, and drives the solution-phase decomposition of ozone and production of OH radicals—called the peroxone process—and this chemistry has been applied as a means of disinfecting drinking water.[57,58] The mechanism of the peroxone process is a matter of recent investigation,[58] [57,58] as well as the chemistry's application to new industrial processes. These are complicated families of reactions, but Eqs. 3.1a and 3.1b provide examples of the role the hydroperoxide ion might play.[57,58]

$$O_3 + HO^- \rightarrow O_2 + HO_2^- \tag{3.1a}$$

$$O_3 + HO_2^- \rightarrow HO^\bullet + O_2^- + O_2 \tag{3.1b}$$

Analogous chemistry may be possible in the atmosphere, as well, though direct evidence of it is sparser. Studying the hydroperoxide anion directly in the gas phase is therefore of some interest in investigating the possibilities of hydroperoxide chemistry in the atmosphere.

3.1.2 *Photoelectron Spectroscopy of HO_2^-*

The photoelectron spectrum of HO_2^- has been studied previously.[60,61] Clifford, et al, performed the most recent of this work.[60] Two electronic states were observed, each with a single vibrational progression. The adiabatic electron affinity, EA, was determined to be 1.089 ± 0.006 eV, with a splitting between the ground and excited states, ΔE of 0.871 ± 0.007 eV, placing the onset of the excited state at 1.960 eV.[60] The vibrational progression in each state corresponded to the O–O stretching mode, with a frequency of 1097.63 cm^{-1} in the ground state and 929.068 cm^{-1} in the excited state.[60] These values were in excellent agreement with previous work on the system,[61-64] including the photoelectron spectrum collected by Oakes, *et al*, which found an EA of 1.078 ± 0.017 eV,[61] and near-IR emission, which found ΔE of 0.871 574 5 ± 0.000 000 2 eV).[63]

Because the spectral information is already well-characterized, in this work we focus on the PADs, which have not been explored in any detail to this point. The well-understood spectrum gives some advantage to this end, allowing for unambiguously separate characterizations of photodetachment from the ground and excited states. Additionally, its similarities to other well-characterized systems in O_2^- and NO^- afford the opportunity to explore the role of molecular symmetry in the robust, quantitative model our group has developed for understanding photodetachment from mixed-character molecular orbitals.

3.1.3 Connection between Symmetry and Photoelectron Angular Distributions

The development and derivation of the Generalized Mixed Character Model[44] underpinning the analysis presented in this chapter is described in detail in Section 1.3. Here, we develop that thinking specifically as it applies to symmetry considerations.

Qualitatively, it is straightforward to understand one-photon, one electron photodetachment from atomic orbitals. Applying the angular momentum quantum number selection rule, $\Delta l = \pm 1$, and $\Delta m_l = 0$, to, for example, photodetachment from the 1*s* orbital of H^- yields a p_z outgoing free electron wave aligned to the laser electric field vector—a parallel PAD with $\beta = 2$. Similarly, detachment from a 2*p* orbital yields a combination of *s*, d_{z^2}, d_{xz}, and d_{yz} outgoing waves. At very low ε, the s wave dominates, according to the Wigner threshold law,[29] leading to an isotropic PAD ($\beta = 0$), becoming perpendicular with increasing ε ($\beta < 0$) as the outgoing waves interfere, before becoming isotropic again at high ε as the outgoing *d* waves begin to dominate.

The same is true of mixed-character molecular orbitals, assuming the expansion in the basis set of atomic orbitals is good. In the case, for example, of an *s*-*p* mixed character orbital, the outgoing waves described above for each the *s* and *p* channels interfere—there are all three *s*, *p*, and *d* components in the outgoing free electron wave.[37,43] This is reflected in the anisotropy data for solvated H^-, where the 1*s* orbital is now polarized by interaction with the solvent molecule, introducing some effective *p*-character, with low-ε PADs being isotropic—dominated by the solvation-introduced *s* component of the outgoing electron wave—instead of the flat parallel PADs seen in detachment from just H^-.[38] Likewise, the sp^x hybrid orbitals in the σ system of deprotonated heterocyclic aromatic molecules yield p-like $\beta(\varepsilon)$ curves, which are made shallower (i.e. β is less negative at minimum) by the introduction of a p_z component to the outgoing wave.[39-42,46]

In case where the molecular orbital is difficult to model using a limited subset of atomic functions, an argument can sometimes be made using point group symmetry. Photodetachment from CS_2^-, for example, was effectively treated with only s and p outgoing waves[36] by determining the symmetry of outing electron waves in the laboratory frame from photodeatchment from each of the three principle orientations of the molecule, accurately predicting a parallel PAD for detachment to the CS_2 ground state, and perpendicular anisotropy for detachment to the excited states. The argument is summarized graphically in Figure 3.1.

CS_2^- is a bent triatomic with C_{2v} symmetry and a $^2A_1$ ground state. The original $s\&p$ model developed by our group[36] defines three principal orientations of the molecule in the laboratory frame (LF), as shown in Figure 3.1. Each principal orientation corresponds to a specific orientation of the light electric field vector in the molecular frame (MF). The corresponding irreducible representations of the field vector in the MF are indicated in the top row of Figure 3.1. Within the electric-dipole and molecular-orbital approximation, the symmetry character of the outgoing free electron wave, ψ_f, can be determined (separately for each of the principal orientations) by requiring:

$$\vec{\mu}_{MO\to f} = \langle \psi_f | \hat{\mu} | \psi_{MO} \rangle \neq 0 \qquad (3.2a)$$

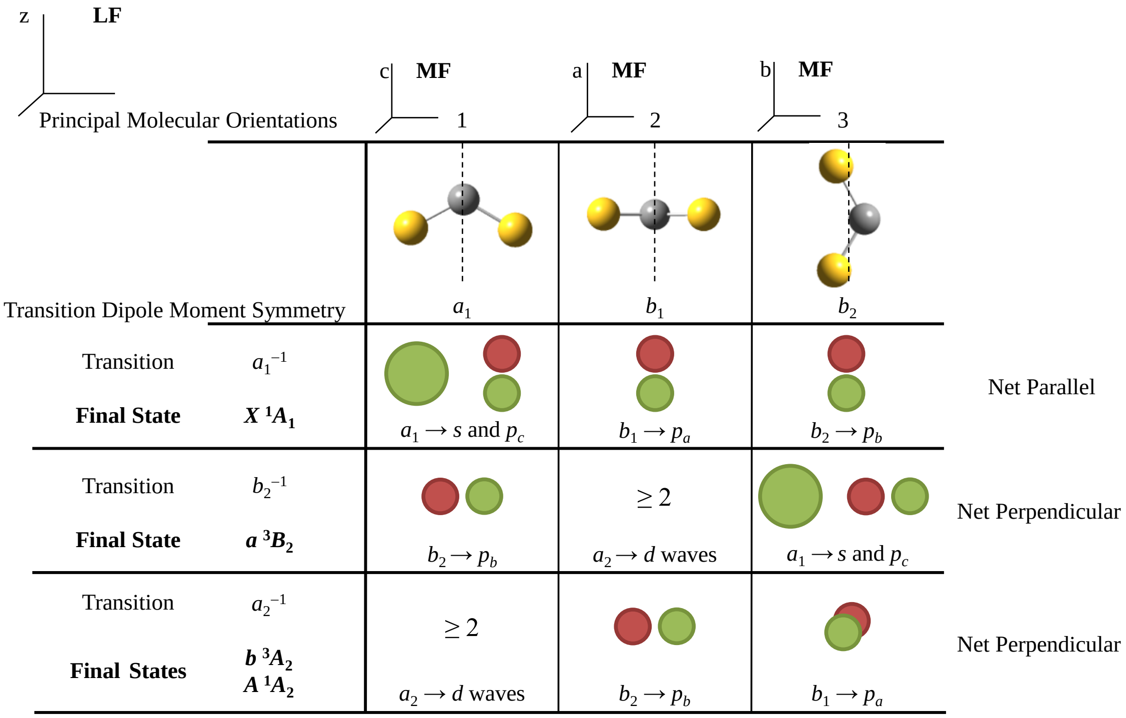

Figure 3.1. Schematic summary of the modeling of photodetachment from CS_2^- using the *s*&*p* model.

where $\vec{\mu}_{MO\to f}$ is the transition-dipole vector, $\hat{\mu} = -e\hat{r}$ is the dipole operator, and ψ_{MO} is the parent MO. Since the amplitude of a dipole-allowed transition is proportional to the scalar product of the transition dipole, $\vec{\mu}_{MO\to f}$, and the electric field vector, only the z component of $\vec{\mu}_{MO\to f}$, and therefore $\hat{\mu}$, needs to be considered and the non-zero requirement in Eq. 3.2a can be replaced by

$$\langle \psi_f | \hat{z} | \psi_{MO} \rangle \neq 0 \tag{3.2b}$$

For the integral in Eq. 3.2b to be non-zero, we must require that the direct product of the irreducible representations of ψ_f, the LF z axis, and ψ_{MO} contained the totally symmetric representation (A_1 for the C_{2v} symmetry point group):

$$\Gamma(\psi_f) \otimes \Gamma(z) \otimes \Gamma(\psi_{MO}) \subset \mathrm{A}_1 \tag{3.2c}$$

Since both ψ_f and ψ_{MO} are defined in the MF, while z is a LF axis, Eq. 3.2c is subject to the MF-to-LF transformation and will yield different results for the different principal orientations.

Specifically, in the one-electron molecular-orbital approximation, the photodetachment of CS_2^- accessing the ground state of CS_2 corresponds to removal of an electron from the a_1 HOMO of the anion, i.e. $\Gamma(\psi_{MO}) = A_1$. We define the MF with the c axis along the C_2 principal rotation axis, and the bc-plane containing the plane of the molecule. In the first principal orientation, the MF c-axis aligns with the LF z-axis, such that we have $\Gamma(z) = A_1$, and photodetachment from this orbital yields an A_1 symmetry outgoing wave. Limiting the discussion to s and p partial waves only, we conclude s and

p_c outgoing waves must be considered. Since the MF *c*-axis aligns with the LF *z*-axis in this principal orientation, the p_c wave becomes a p_z wave in the MF → LF transformation.

For the second principal orientation, the MF *a*-axis is aligned with the LF *z* axis, such that $\Gamma(z) = B_1$, and detachment yields a B_1 symmetry outgoing wave, corresponding to a p_a outgoing wave. This p_a wave becomes a p_z wave in the MF → LF transformation. Likewise, in the final principal orientation, the MF *b*-axis is aligned with the LF *z* axis, such that $\Gamma(z) = B_2$, and detachment yields a B_2 symmetry outgoing wave, corresponding to a p_b outgoing wave. Again, this p_b wave becomes a p_z wave on transformation to the laboratory frame.

In summary, each of the principal orientations yield LF p_z waves, while one orientation yields an isotropic *s* wave. Each of these p_z waves is aligned to the laser electric field vector, and in total, the model correctly predicts a net perpendicular PAD. The perpendicular PADs for detachment to the excited states of CS_2 can likewise be accurately modeled using this thinking, as summarized in Figure 3.1.

This model is qualitative and its applications must therefore be nuanced, but it has been shown to be a powerful tool for modeling photodetachment from molecular orbitals, which in some cases would be difficult to describe otherwise. Inspecting this thinking for insights into when, how, and why it works or fails for different molecules could prove useful in garnering further chemical insights from the quantitative model we've developed. The hydroperoxide anion provides a unique opportunity to explore the confluence of point group symmetry arguments and basis set expansion arguments, with photodetachment from two parent orbitals (shown in Figure 3.2) with different symmetry character but otherwise similar wavefunctions, which can be described with a *p*-*d* model function.

3.2 Specific Methods

The general operation of the experiment and means of extracting the spectra and angular information of interest from the photoelectron images have been described in detail already. This section deals with the experimental details specific to the project explored in this chapter.

3.2.1 Experimental Methods

All experiments reported in this chapter used the electron gun setup described in Section 2.2 in the ion source chamber. Methanol in the expansion is deprotonated (Equation 2.2a), and the resulting methoxide reacts with oxygen to form hydroperoxide *via* the known chemistry described in Equation 1.1b in Section 1.1.[5,9]

Photoelectron images of HO_2^- were collected at eight wavelengths: 306 nm, 355 nm, 406 nm, 607 nm, 612 nm, 622 nm, 797 nm, and 812 nm. Images at 607 nm, 612 nm, and 622 nm were collected with VMI voltages of (bottom plate, middle plate, top plate) -330 V, 0 V, and +900 V; images at 306 nm, 355 nm, 797 nm, and 812 nm were collected with VMI voltages of -220 V, 0 V, and +600 V; and images at 406 nm were collected with VMI voltages of -165 V, 0 V, and +450 V.

Images collected at 306 nm were slightly elliptically distorted. These elliptical distortions were corrected by the circularization tool in the PyAbel package.[65,66] The

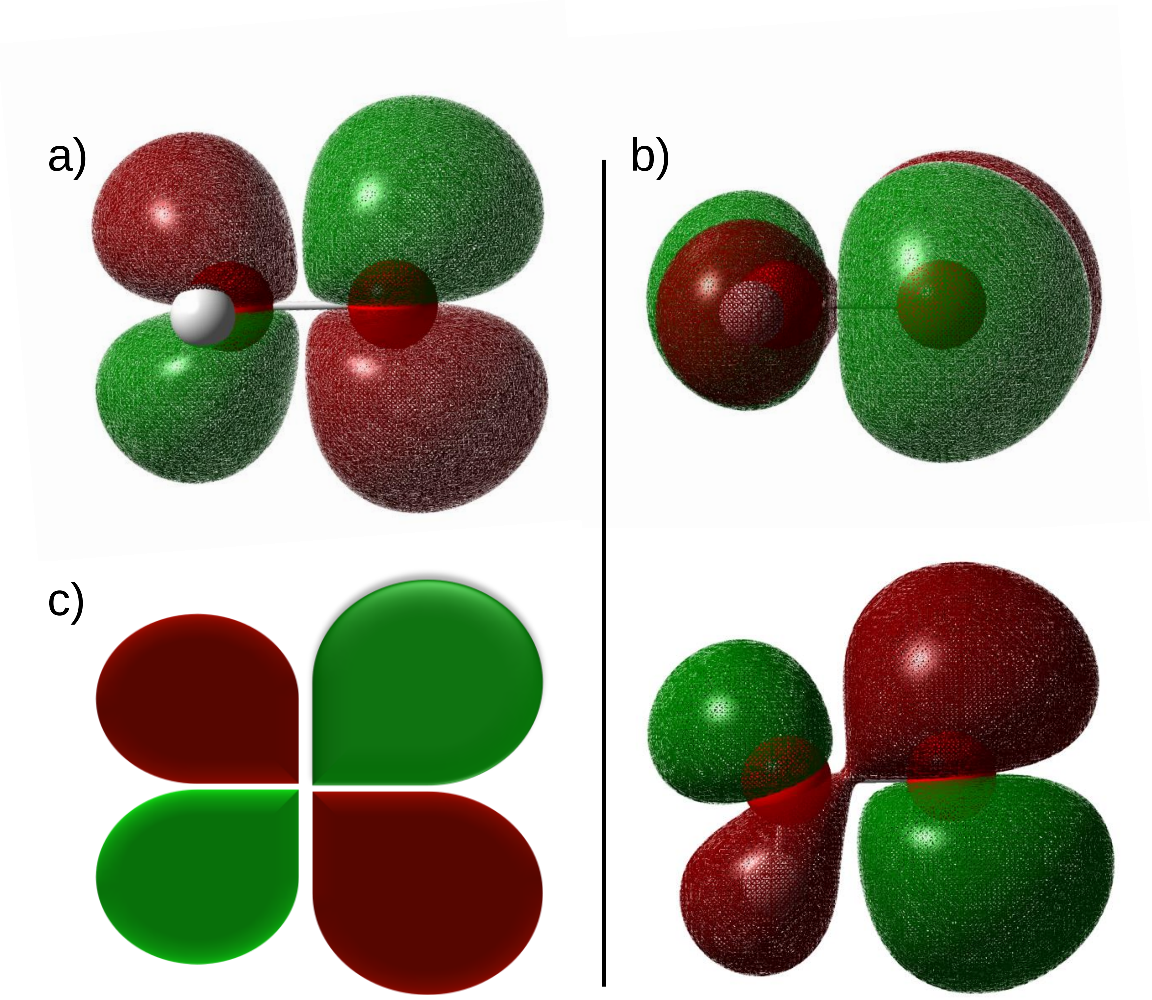

Figure 3.2. HO$_2^-$ a) HOMO and b) HOMO-1 in two molecular orientations calculated at the CCSD(T) level of theory with a d-aug-cc-pVQZ basis set, and c) a representation of the *p-d* model function fit to each molecular orbital, $|\psi_{pd}\rangle = (1-\gamma_d)|p\rangle + \gamma_d|d\rangle$.

image and spectrum collected at 306 nm which appear in Figures 3.3a, Figure 3.3i, and 3.4a have been subjected to the PyAbel circularization correction.

3.2.2 Computational Methods and Modeling

This section will be broken into two halves: first, the generation and explanation of the *p*-*d* case of the generalized mixed character model our group developed previously; and second, the methods used to fit the model to the data in order to extract the most meaningful chemical information.

The generalized mixed character model and generating the p-d case. In Section 1.3, the derivation of a general form for modeling photodetachment from mixed-character molecular orbitals[44] is described. Eq. 1.18 represents the case where the model function is comprised of two atomic orbitals with consecutive *l* quantum numbers. We define a model function for the *p*-*d* mixed case, shown in Eq. 3.3:

$$\left|\psi_{pd}\right\rangle = \sqrt{1-\gamma_d}\left|p\right\rangle + \sqrt{\gamma_d}\left|d\right\rangle \tag{3.3}$$

where γ_d is the fractional *d*-character of the molecular orbital. Writing Eq. 1.18 for this model function yields:

$$\beta_{pd}(\varepsilon) = \frac{(1-\gamma_d)B_2\varepsilon\left(2A_1^2\varepsilon^2-4A_1\varepsilon\cos\delta_{2,0}\right)+\gamma_d A_1^2\varepsilon^2\left(2+12A_2^2\varepsilon^2-36A_2\varepsilon\cos\delta_{3,1}\right)/5}{(1-\gamma_d)B_2\varepsilon\left(1+2A_1^2\varepsilon^2\right)+\gamma_d A_1^2\varepsilon^2\left(2+3A_2^2\varepsilon^2\right)} \tag{3.4}$$

The parameters are described in detail in Section 1.3.

The β values at specific ε are measured in the experiment, and we can fix the phase shift terms, $\delta_{2,0}$ and $\delta_{3,1}$, at reasonable values, by considering the physics leading the to the phases of the outgoing electron waves. Since the remaining core is a neutral molecule, the Coulombic interaction with the outgoing electron wave is weak, and the phase delays imparted are small. The radial functions of the outgoing waves are proportional to the spherical Bessel functions,[43,67,68] and, for all $l \geq 1$, have nodes at $r = 0$, corresponding to the expansion center. Because of the nodes, the phase delay values for outgoing *p*, *d*, and *f* waves are expected to be particularly small and the resulting phase differences between pairs of different waves can be assumed to be negligible. Therefore, we fix $\cos\delta_{3,1} = 1$. However, the *s* radial function does have density at $r = 0$, and we do expect some phase imparted to an outgoing *s* wave, if small. This effect has led to observed values of $\cos\delta_{2,0}$ between 0.88 and 0.98[39] in negative ion photoelectron spectroscopy experiments. For this work, we choose a plausible value close to the middle of that range, $\cos\delta_{2,0} = 0.95$, allowing our model to capture this physics without introducing an additional fitting parameter.

This leaves us with four adjustable fitting parameters in Eq. 3.4: the A_1, A_2, B_2, and γ_d. The relative scaling terms depend intrinsically on the spatial extent of the molecular orbital and how tightly the electron is bound to the molecule. We can take advantage of this fact, and collapse those three fitting parameters into two by expressing the A_l and B_l terms in terms of the effective charges, ζ_{2p} and ζ_{3d}, of the orbitals comprising our model function, reducing three fitting parameters into two.[44]

$$A_1 = \frac{16}{\zeta_{2p}^2}, \quad A_2 = \frac{144}{5\zeta_{3d}^2}, \quad B_2 = \frac{2^9 \zeta_{3d}^7}{5 \cdot 3^6 \zeta_{2p}^9} \tag{3.5}$$

With the center of the model function at the center of the O–O bond, rather than on any atom, these ζ parameters describe the spacial extents of the corresponding basis functions, rather than the actual charges on any atom in the molecule. As for atomic orbitals, smaller values of ζ corresponding to more diffuse functions/orbitals.

Using these relationships, we have a practical means of using this mixed-character model to describe photodetachment from each the HOMO and HOMO−1 of HO_2^-.

Fitting the model function to the molecular orbitals. The HOMO and HOMO−1 of HO_2^- were calculated using Gaussian09[69] at the CCSD(T) level of theory with the d-aug-cc-pVQZ basis set, chosen for its ability to capture most accurately the diffuse contributions to the orbitals. These *ab initio* calculated orbitals appear in Figure 3.2a-b, along with a representation of the *p-d* model function in Figure 3.2c. Formatted checkpoint files were used to generate custom 70x70x70 Cube files for each molecular orbital of interest, and these files were imported into a MATLAB program written initially by Lori Culberson for *s-p* hybrid orbitals, modified by Dmitry Khuseynov for the *p-d* case, and updated by Adam Wallace and myself for broad application to systems irrespective of molecular orientation in the Gaussian output files. The MATLAB program generates a 70x70x70 cube for the model function, and then performs a least squares fit to best match the model function to the *ab initio* molecular orbital. This program outputs the best-fit values: the fractional *d*-character, γ_d, and the effective charges of the two basis functions in the model function, ζ_{2p} and ζ_{3d}. The program also outputs a trace of the wavefunction amplitudes along one user-chosen axis to verify the model function and molecular orbital are centered on the same point.

The measured $\beta(\varepsilon)$ values are imported into a second MATLAB program, written specifically for this work, which fits the Equation 3.4, containing the definitions in Equation 3.5, to the experimental data. Fixing the values of $\cos\delta_{2,0}$ at 0.95 and $\cos\delta_{3,1}$ at 1, and using the value of γ_d determined in the fit of the model function to the *ab initio* calculated molecular orbital, the program runs a least-squares fit to determine the values of ζ_{2p} and ζ_{3d} which result in the best agreement between the model and the data.

3.3 Results

3.3.1 Photoelectron Spectra

Raw photoelectron images and the inverse Abel transformations for HO_2^- collected at 306 nm, 355 nm, 406 nm, 607 nm, 612 nm, 622 nm, 797 nm, and 812 nm appear in Figure 3a-h. Their corresponding photoelectron spectra are plotted together for easy comparison in Figure 3i, and separately for individual clarity in Figure 3.4.

At 622 nm and shorter wavelengths, two neutral electronic states are accessed, with vibrations in each state resolved either partially, as in the 306 nm and 355 nm spectra, or well in all others. These spectra are consistent with existing work on HO_2^-.[60-64] The adiabatic electron affinity (EA), of to the ground state of the neutral peroxy radical, $X\ ^2A''$, is 1.089 ± 0.011 eV, with a vibrational progression in the ground state with a frequency of 1042 ± 20 cm^{-1}, corresponding to the O–O stretching mode. The onset of the second electronic band, corresponding to the neutral excited state, $A\ ^2A'$, occurs at 1.951 ± 0.002 eV, and the excited state vibrational progression has a frequency of 908 ± 88 cm^{-1}, again corresponding to the O–O stretch.

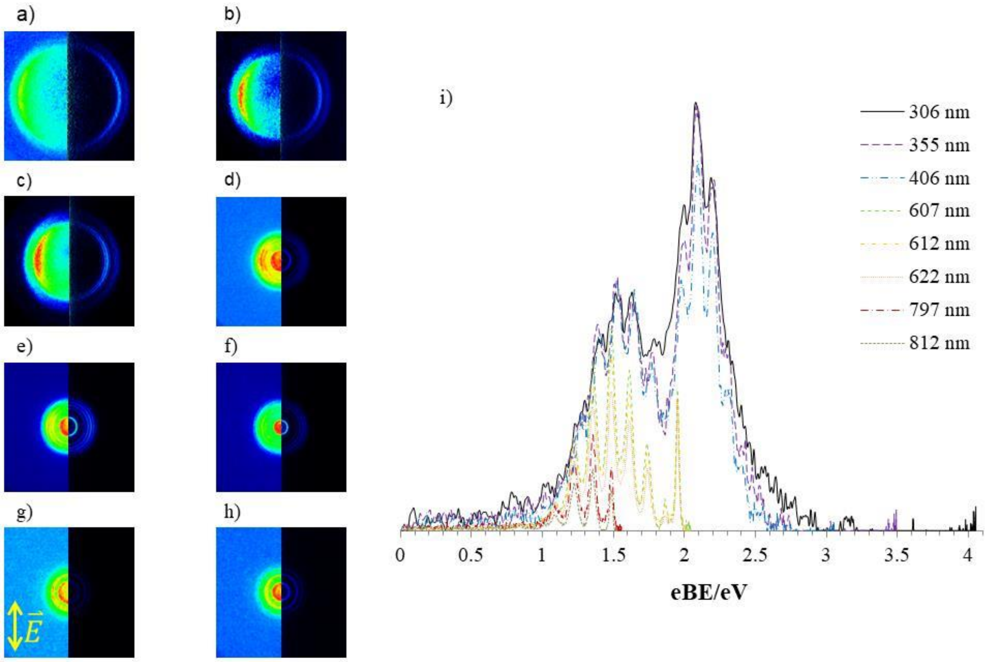

Figure 3.3. Raw (left) and inverse Abel transformed (right) photoelectron images of HO_2^- collected at a) 306 nm, b) 355 nm, c) 406 nm, d) 622 nm, e) 612 nm, f) 607 nm, g) 797 nm, and h) 812 nm. i) Photoelectron spectra corresponding to the photoelectron images collected at each wavelength.

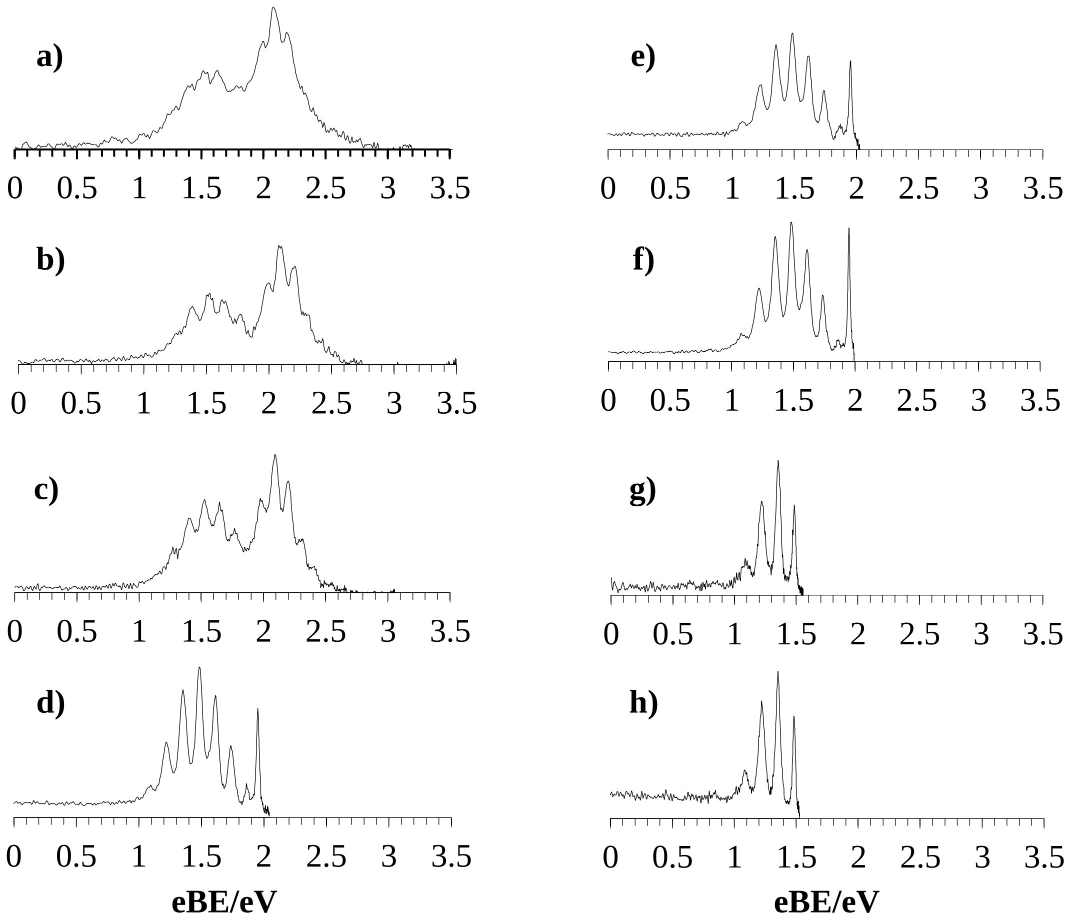

Figure 3.4. Photoelectron images at a) 306 nm, b) 355 nm, c) 406 nm, d) 607 nm, e) 612 nm, f) 622 nm, g) 797 nm, and h) 812 nm.

3.3.2 Photoelectron Angular Distributions

Since these spectra have already been well characterized, the focus of this work is on the photoelectron angular distributions. Detachment from each the HOMO and HOMO−1, yielding the ground and excited states of the neutral, respectively, exhibit nearly isotropic PAD at low ε, and become increasingly perpendicular with increasing photon energy. The anisotropy parameters, β, are plotted as a function of ε in Figure 3.5 for detachment to each the ground (3.5a) and excited (3.5b) states of the neutral molecule. For detachment from the HO_2^- HOMO, the PAD becomes increasingly perpendicular ($\beta < 0$) with increasing ε, beginning to flatten around 1.5 eV, with a minimum of −0.76 ± 0.02 at 2.54 eV. The trend in detachment from the HOMO−1 is slightly deeper, reaching an observed minimum of −0.802 ± 0.001 at 1.88 eV, though without higher ε data, it is not possible to declare unequivocally that this represents the bottom of the $\beta(\varepsilon)$ curve.

3.4 Discussion

3.4.1 Fitting the p-d Mixed Character Model to the Photoelectron Angular Distributions

Using the MATLAB program described above, the HOMO and HOMO−1 of HO_2^- are fit to the *p-d* model function defined in Equation 33. For the HOMO, this fit returns a γ_d of 0.979 (i.e. 97.9% *d*-character) and effective charges, ζ_{2p} of 1.59 and ζ_{3d} of 4.71. For the HOMO–1, a γ_d of 0.871 and effective charges, ζ_{2p} of 2.09 and ζ_{3d} of 4.54.

When fitting the model to the data, the fractional *d* character is fixed at the value determined in the fit of the model function to the *ab initio* molecular orbital, while the

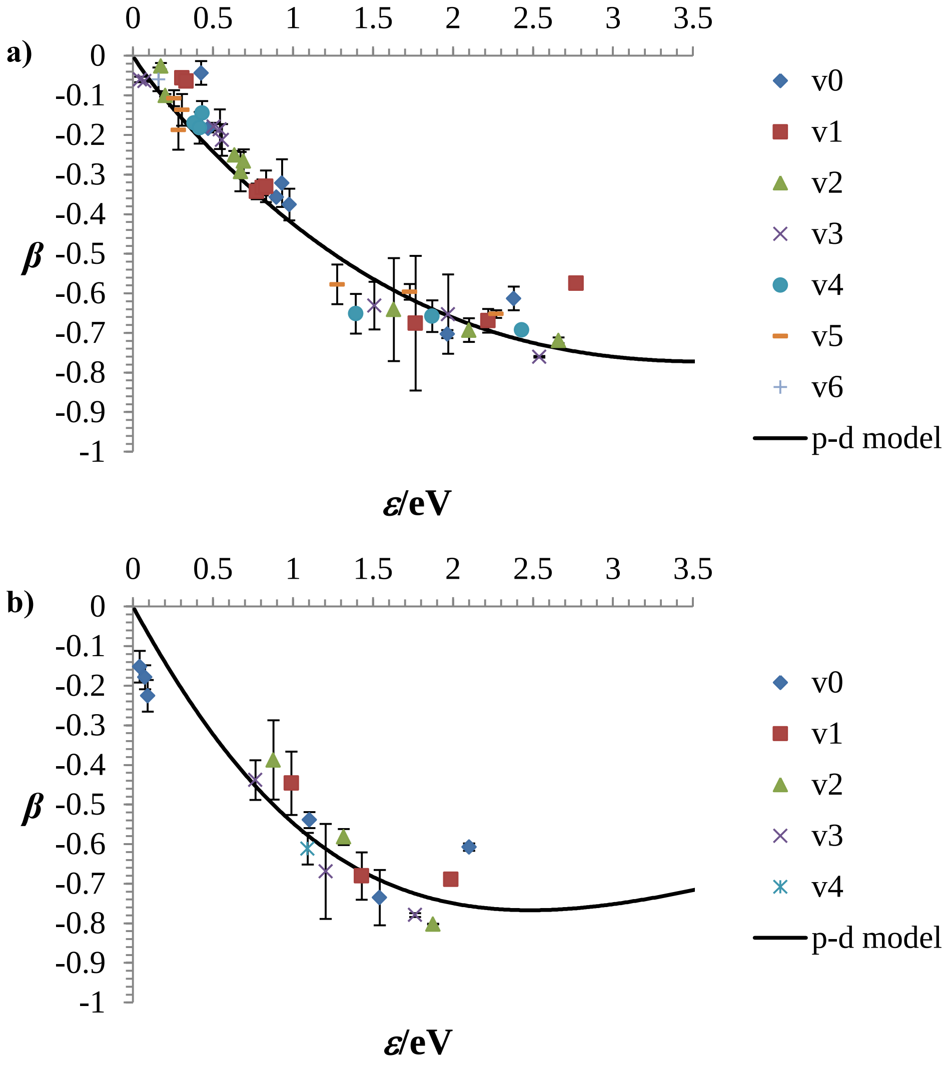

Figure 3.5. Anisotropy parameter, β, as a function of electron kinetic energy, ε, for photodetachment from the a) HOMO, and b) HOMO-1 of HO_2^-. The data are fit with a curve which models the molecular orbitals as a superposition of one *p* and one *d* orbital. In each curve, $\cos\delta_{2,0}$ is fixed at 0.95, and $\cos\delta_{3,1}$ at 1. The fractional *d*-character, γ_d, was determined by fitting the model function to the *ab initio* calculated molecular orbital, and ζ_{2p} and ζ_{3d} were adjusted as fit parameters. In a), γ_d is 0.979, ζ_{2p} is 1.05, and ζ_{3d} is 2.62. In b), γ_d is 0.871, ζ_{2p} is 1.06, and ζ_{3d} is 2.41.

effective charges are varied as parameters to fit Equation 3.4 and 3.5 to the data. This choice is made because the MATLAB fit is limited by the parameters of the molecular orbital Cube file, and it does not necessarily effectively capture the “size” of the orbital, reflected in the ζ values, as it does the “shape” of the orbital—which is the same largely irrespective of choices made when generating the Cube file—reflected in the γ_d value. The fit for detachment from the HOMO yields ζ_{2p} of 1.05 and ζ_{3d} of 2.62, and to the HOMO−1, ζ_{2p} of 1.06 and ζ_{3d} of 2.41. The fits can be seen in Figure 3.5, and the fit parameters are summarized in Table 3.1.

3.4.2 Comparison of Photoelectron Angular Distributions for Detachment to the Ground and Excited States

While the HOMO and HOMO−1 of HO_2^- are qualitatively similar, each appearing as a lopsided *d*-orbital, with the smaller lobes on the side of the hydrogen atom, the difference in γ_d between them is substantial. The two orbitals are perpendicular to each other, with the HOMO having A″ symmetry, with lobes out of the plane of the molecule, and the HOMO−1 with A′ symmetry and lobes in the plane of the molecule. There is clear σ-bonding character to the HOMO−1, with respect to the O−H bond. While this orbital is not a true *p*-*d* mixed orbital, it has clear *p*-*d*-mixed character.

The partial σ-bonding character of the HOMO−1 with respect to the O−H bond, versus the througout π-antibonding character of the HOMO, explains the energetic ordering of the orbitals, but is also consistent with the difference in fractional *d*-characters of the orbitals. With the hydrogen atom in the plane of the orbital rather than

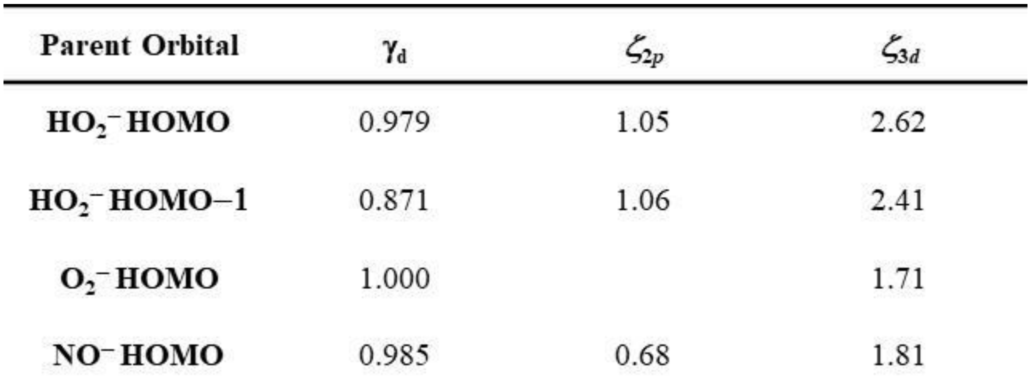

Parent Orbital	γ_d	ζ_{2p}	ζ_{3d}
HO_2^- HOMO	0.979	1.05	2.62
HO_2^- HOMO–1	0.871	1.06	2.41
O_2^- HOMO	1.000		1.71
NO^- HOMO	0.985	0.68	1.81

Table 3.1. Fitting parameters for applying the *p-d* case of the Generalized Mixed Character Model to HO_2^- and NO^-, and the $l = 2$ case of the Cooper-Zare Equation to O_2^-, assuming $\cos\delta_{2,0} = 0.95$ and $\cos\delta_{3,1} = 1$. Values of γ_d were determined by fitting the *p-d* model function to the *ab initio* calculated molecular orbital, while ζ_{2p} and ζ_{3d} were determined by fitting the model to the experimental data.

perpendicular to it, the effect it has on distorting the otherwise *d*-like orbital is increased, and the contribution of the polarizing 2*p* basis function is larger.

3.4.3 Comparison of Photoelectron Angular Distributions of HO_2^- to O_2^- and NO^-

The HOMO of each O_2^- and NO^- appear in Figure 3.6. While there is no true *d*-orbital in O_2^-, its PAD has been effectively modeled as detachment from a *d*-orbital using the Cooper-Zare equation with $l = 2$. As in using the *p-d* model for HO_2^-, $\cos\delta_{3,1}$ is set equal to 1 for the reasons described in section 3.2.3 above, leaving only A_2 (and thus ζ_{3d} via Equation 3.5) as a fitting parameter. Due to strong vibronic coupling in photodetachment from O_2^-, only the vertical transition, $O_2(X\ ^3\Sigma_g^-, v'=2) \leftarrow O_2^-(X\ ^2\Pi_g'', v=0)$, is considered. In previous work,[32-34] fitting the Cooper-Zare equation to the data yielded a value for A_2 of 0.42, corresponding to ζ_{3d} of 1.59, but that work allowed $\cos\delta_{3,1}$ to vary as a fit parameter. Performing a least-squares fit on these data without using $\cos\delta_{3,1}$ as a fitting parameter yields a ζ_{3d} value of 1.71, corresponding to a value of A_2 of 0.36.

There is also strong vibronic coupling in photodetachment from NO^-, so once again, only the vertical transition, $NO(X\ ^2\Pi, v'=2) \leftarrow NO^-(X\ ^3\Sigma^-, v''=0)$, is considered. Fitting the HOMO of NO^- to the *p-d* model function yields γ_d of 0.985, ζ_{2p} of 1.63, and ζ_{3d} of 5.20. In previous work,[44] a least squares fit of the *p-d* model to the data yields ζ_{2p} of 1.46 and ζ_{3d} of 5.94, fixing both cosine terms equal to 1. In the interest of being internally consistent in this work, the least squares fit was carried out again with $\cos\delta_{2,0} = 0.95$. The new parameters are ζ_{2p} of 0.68 and ζ_{3d} of 1.81. Molecular orbitals appear in

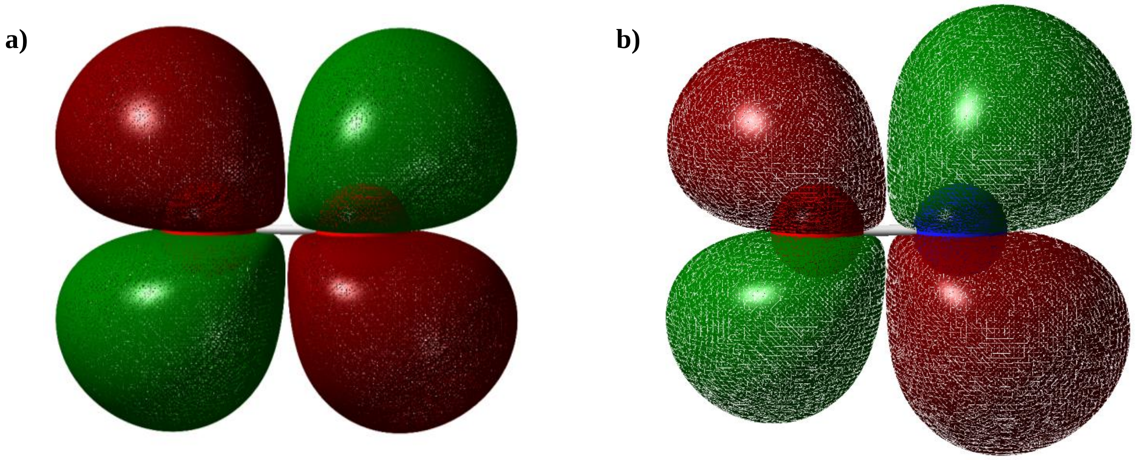

Figure 3.6. HOMO of a) O_2^- and b) NO^-. O_2^- is modeled as c) an atomic *d*-orbital, while NO^- is modeled as d) a *p*-*d* mixed-character orbital.

Figure 3.6, and the new fits carried out in this work in Figure 3.7. The fit parameters appear alongside those for HO_2^- in Table 3.1.

These three molecules afford the exploration of the effect of symmetry-breaking perturbations on the nature of molecular orbitals, reflected in their corresponding PADs. The highest symmetry molecule is O_2^-, with a $D_{\infty h}$ point group, and degenerate HOMO belonging to the Π_g irreducible representation, two perpendicular but otherwise identical *d*-like molecular orbitals. Perturbing that symmetry by changing one oxygen atom to a nitrogen atom drops the symmetry to another linear point group, $C_{\infty v}$, once again with a degenerate HOMO, this belonging to the Π irreducible representation. These are, again, orbitals perpendicular to each other, but otherwise identical; however, the removal of the σ_h reflection plane in the heteronuclear diatomic is manifest is the *p*-*d*-like distortion we see.

Adding a hydrogen atom to the O_2^- structure has an even more drastic effect reducing the symmetry to the C_s molecular point group, and breaking the degeneracy of the HOMO, splitting the O_2^- π_g orbital into an a'' HOMO and an a' HOMO−1—qualitatively similar, but no longer identical. The significantly lower symmetry is reflected in a slight increase in the perturbing *p*-character introduced into the out-of-plane HOMO as compared to the distortion in NO^-, and a significant, ~10% increase in *p*-character perturbing the in-plane HOMO−1.

The broad understanding of the magnitude of the A_l parameters is related to the eBE, with larger eBE corresponding to larger A_l values, and from that connection, we should be able to say the same of the values of all ζ_{nl}. This is a good interpretation of the

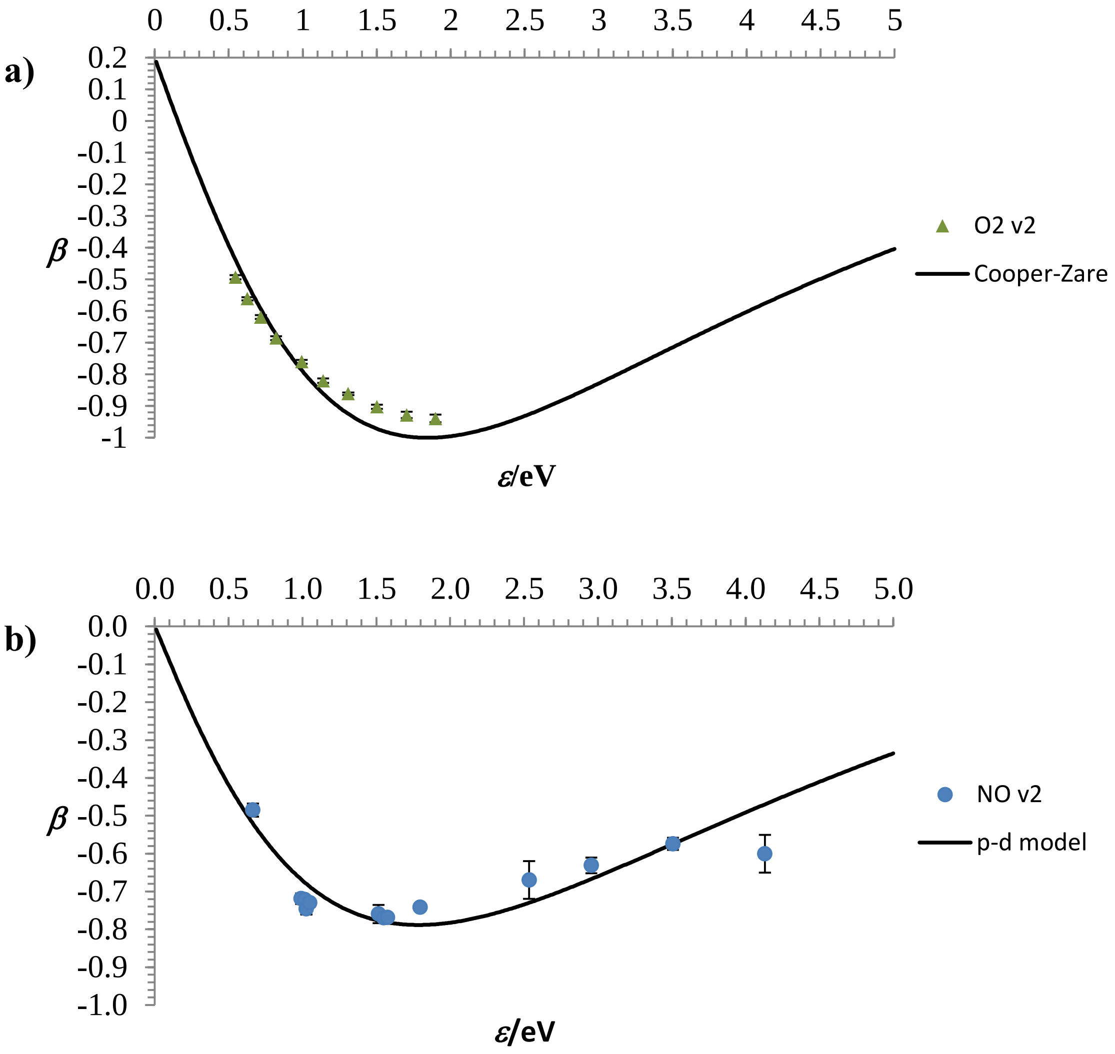

Figure 3.7. a) Fit of the $l = 2$ case of the Cooper-Zare equation to the experimental O_2^- anisotropy parameters, β, as a function of electron kinetic energy, ε. b) Fit of the *p-d* case of the mixed character orbital model to the experimental NO^- β values as a function of ε.

parameter for photodetachment from atomic anions, as well as from many molecules; however, molecular orbitals introduce new considerations which may be captured in the values of ζ_{nl} parameters, such as the bond length of a diatomic, or the number of atoms in a polyatomic molecule over which the parent orbital is delocalized. In the systems discussed here, this effect may be exaggerated by the fact that the center of the orbital—the point at which we are defining the effective charges—lies between atoms rather than being centered on one.

There are, however, two features of the ζ_{2p} and ζ_{3d} values determined in this work. The first is that, for every orbital treated, which should have comparable spatial extents based on the binding energies and the size the molecules. Secondly, in every *p*-*d* case, ζ_{2p} is smaller than ζ_{3d}, meaning the polarizing 2*p* term is more diffuse than the dominant 3*d* function. This means the polarizing effect is more significant on the diffuse region of the orbital. Since the diffuse regions of orbitals are especially important in the physics of photodetachment, a fit to the data consistent with a model function most polarized in the large-*r* portion is an expected result, giving confidence to the quality of the experimental fitting done here.

3.4.4 Results in the Context of Symmetry Arguments

In order to complete the arguments made here about the role symmetry plays in PADs, we apply to detachment each from the HOMO and HOMO−1 of HO_2^- the *s&p*[36] symmetry model outlined briefly in Section 3.1.3 above. We define the MF(*abc*) coordinate system such that the MF *c* axis is perpendicular to the σ_h reflection plane and the molecular plane is contained in the *bc* plane, as shown in Figure 3.8. Because HO_2^-

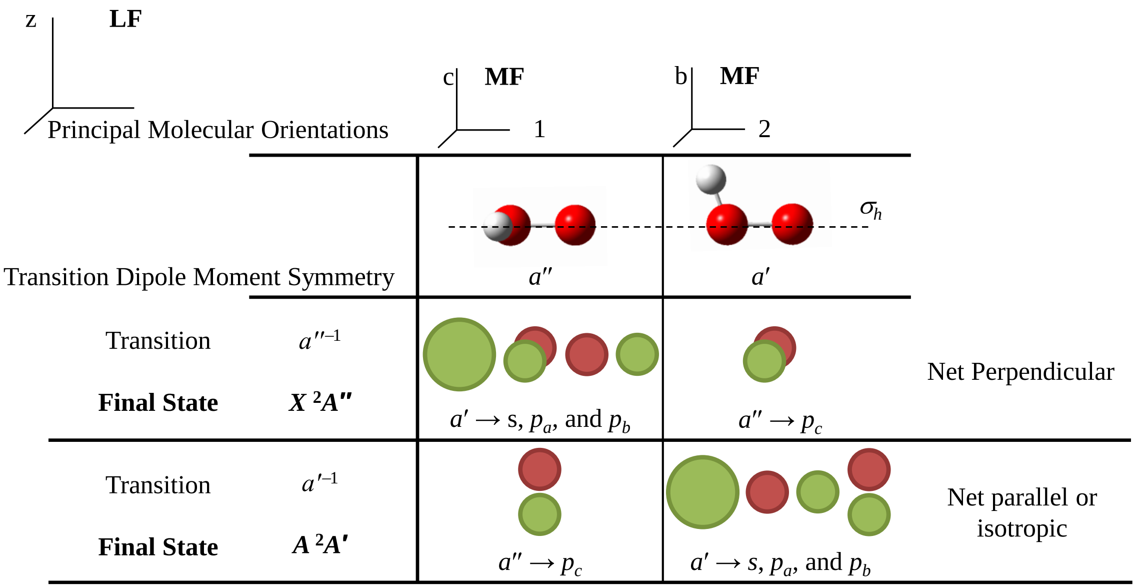

Figure 3.8. Schematic detailing the prediction of the *s* and *p* symmetry model on photodetachment each from the HOMO and HOMO–1 of HO_2^-. Outgoing orbitals and their symmetry correspond to the molecular frame.

has C_s point group symmetry, there are only two unique principal orientations: the first in which the MF c-axis is aligned to the LF z-axis, and the second in which the MF c-axis is perpendicular to the LF z-axis. In the first principal orientation, $\Gamma(z)$ = A″, and in the second, $\Gamma(z)$ = A′.

Photodetachment from the a'' HOMO of HO_2^- in the first principal orientation yields an A′ symmetry outgoing wave, corresponding to s, p_a, and p_b waves in the MF frame, the latter two of which transform into p_x and p_y waves in the LF. Photodetachment from the second principal orientation yields an A″ symmetry outgoing wave, corresponding to a p_c wave in the MF, which becomes a p_x wave in the LF. In total, the *s*&*p* model accurately predicts a perpendicular PAD for detachment from the ground state, with all outgoing waves either isotropic or oriented perpendicular to the laser polarization direction.

We can apply the same thinking to photodetachment from the a' HOMO−1. Detachment from the first principal orientation yields an A″ symmetry outgoing wave, corresponding to a p_c wave, which becomes a p_z wave in the LF. Detachment from the second principal orientation yields an A′ symmetry outgoing wave, corresponding to s, p_a, and p_b waves in the MF, the latter of which become p_y and p_z waves, respectively, in the LF. Overall, in the LF one isotropic wave, one wave perpendicular to the laser polarization axis, and two waves parallel to the laser polarization axis are predicted, which sum to an outgoing wave with isotropic or slightly parallel anisotropy. This is inconsistent with the perpendicular anisotropy observed in the experiment.

One of the approximations of the *s*&*p* symmetry model is that it ignores all outgoing waves of $l \geq 2$,[36] but since the PAD can be described completely with the parallel and perpendicular electron density, the addition of *d*-waves, which are symmetric with respect to these two axes, does not change the predictions or account for the discrepancy between the model and the data. Likewise, the contributions of outgoing *f*-waves in this symmetry argument align with the *p*-waves, again failing to account for the error in predicting the PAD for detachment from the HOMO−1. This means the model does not fail to accurately model HO_2^- on grounds only of the simplifying assumption of only considering *s* and *p* outgoing waves, but in reducing orbitals only to their symmetry character, and treating two orbitals whose wavefunctions have very similar character as entirely different.

3.5 Conclusions

This chapter has outlined the analysis of PADs of HO_2^-, modeling each detachment from the HOMO and the HOMO−1 using the *p*-*d* case of the generalized mixed character model. The fractional *d* character, γ_d, for the HOMO was 0.979, and for the HOMO−1 was 0.871. These results were compared each to O_2^- and NO^- photodetachment to explore how symmetry-breaking chemical modifications are reflected in the PAD, and the results of the *p*-*d* case of the generalized mixed character model were compared to that of the *s*&*p* symmetry model described for its use on CS_2^- in previous work. The C_s point group symmetry of HO_2^- lifted the degeneracy of the HOMO in each O_2^- and NO^-, yielding the most polarized *d*-like HOMO of the three molecules, and an even further distorted HOMO−1. The generalized mixed character model also captured the similarity of the HOMO and HOMO−1 of HO_2^-, which the *s*&*p* symmetry model could not.

CHAPTER 4: PHOTOELECTRON IMAGING OF THE FORMATE ANION

4.1. Introduction

The formyloxyl radical (CHO_2) is an intermediate in the reaction between OH and CO, relevant in both atmospheric and combustion chemistry.[70-74] The radical is difficult to fully characterize because of both its instability with respect to the C–H bond, decomposing into H and CO_2;[75,76] and because its ground and first excited electronic states are nearly degenerate, and strongly mix due to the pseudo-Jahn-Teller coupling.[77,78] Both *ab initio* calculations and experimental studies have produced contradictory assignments of the symmetry of the ground state.[77-79]

High-resolution slow photoelectron velocity-map imaging (SEVI) experiments[77] have unambiguously assigned the ground state of CHO_2 to be $X\ ^2A_1$, with an EA of 3.4961 ± 0.0010 eV, and the first excited state, $A\ ^2B_2$, to have a term energy, T_0, of 318 ± 8 cm^{-1} (0.0394 ± 0.0010 eV). These studies also include comprehensive modeling of the vibronic structure of the photoelectron spectrum. A second excited electronic state, $B\ ^2A_2$, with T_0 of 0.536 eV, was also accessed in previous photoelectron spectroscopy work. While no specific photoelectron anisotropy parameters were reported, it was noted in both of these experiments that detachment of the anion to the ground electronic state of the neutral radical corresponded to parallel PADs, while detachment to each excited state gave rise to perpendicular PADs.

Detachment from each of the three highest occupied molecular orbitals (HOMO, HOMO−1, HOMO−2) of formate provides further opportunity for modeling photodetachment from mixed-character molecular orbitals, if sufficient resolution can be achieved to separate their contributions to the photoelectron image. These MOs appear in Figure 4.1, along with the mixed-character model functions proposed to model the PADs for detachment from each. The a_1 orbital has predominant d_{z^2} character, perturbed by an *s* term; the b_2 orbital is modeled as an *f* orbital perturbed by a polarizing p term; and the a_2 orbital can be modeled as a predominantly d-like orbital.

4.2. Specific Methods

Calculations were performed using Gaussian09.[69] Geometries of each the formate anion and the corresponding neutral radical were optimized at the CCSD level of theory with the aug-cc-pVDZ basis set, and the three highest occupied molecular orbitals of the anion were included in the analysis.

Ions for the experiments reported here were generated using the electron gun setup described in Section 2.2.1. Photoelectron images were collected at 306 nm, at two different sets of VMI voltages: -110 V, 0 V, +300 V to achieve the best spectral resolution; and -220 V, 0 V, +600 V to capture the fastest photoelectrons (low eBE regime) on the CCD camera field. The images were corrected for elliptical distortion with the PyAbel[65] circularization tool.[66]

4.3. Results

The circularized image collected at 306 nm, its inverse Abel transformation, and the corresponding photoelectron spectrum using each of the VMI field conditions described above appear in Figure 4.2. Even after circularization, the spectrum appears unresolved, which is due to the spectral congestion, rather than poor experimental

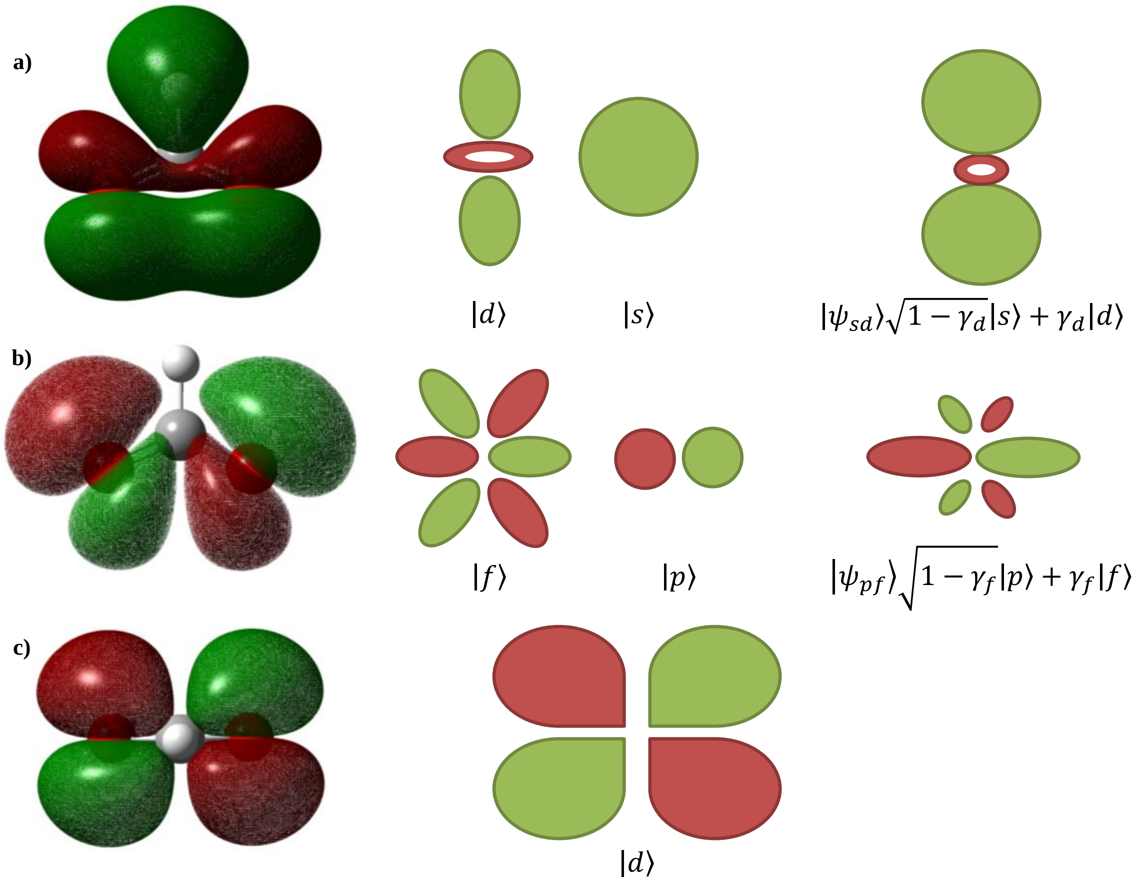

Figure 4.1. The a) a_1, b) b_2, and c) a_2 MOs of CHO_2^-, as well as cartoon representations of the *s*-*d* model function for a), the *p*-*f* model function for b), and the *d*-like model function for c).

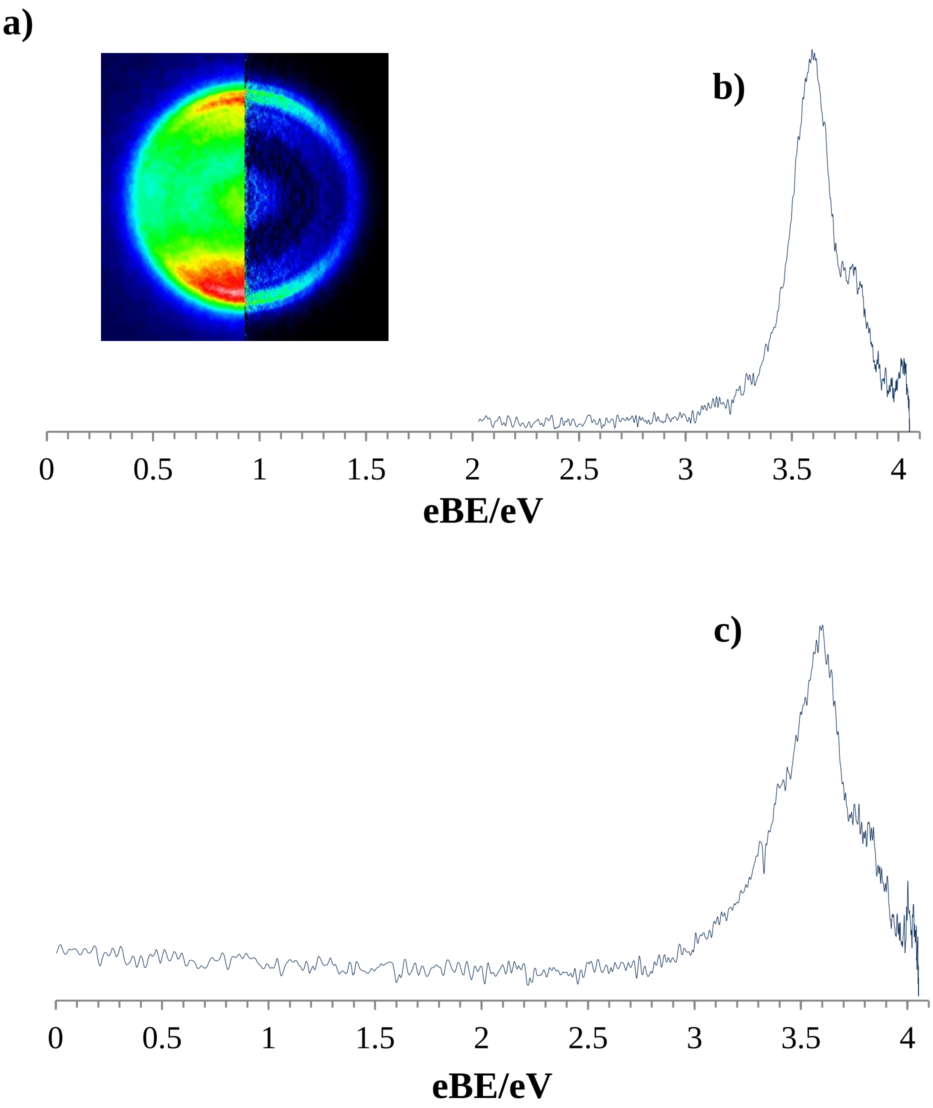

Figure 4.2. a) Circularized photoelectron image (left) and inverse Abel transformation (right) and b) photoelectron spectrum of CHO_2^- at 306 nm with VMI voltages of -110 V, 0 V, and 300 V. c) Photoelectron spectrum of CHO_2^- at 306 nm with VMI voltages of -220 V, 0 V, and 600 V.

resolution. The onset of the spectrum appears at approximately 3.3 eV, peaking at 3.59 eV, consistent with the position of the highest intensity peak observed in the previous work, assigned to the combination of $3^1_0(^2A_1)$ and $6^1_0(^2A_1)$ transitions, at an eBE of 3.5660 eV.[77,78]

Also consistent with previous work on photodetachment from formate,[77] a clear parallel PAD is observed in the photoelectron image, as well as an apparent more isotropic transition appearing at higher eBE relative to the dominant band. The photoelectron anisotropy parameters values were determined for narrow slices every 100 meV, starting on the leading edge of the onset at 3.29 eV, are plotted as a function of ε in Figure 4.3, illustrating the predominantly parallel character of the most intense region of the spectrum, with a β value of 0.61 ± 0.10 at the peak at 3.59 eV. The high-eBE tail of the band has even greater parallel anisotropy, with β of 0.85 ± 0.07 at 3.69 eV. The beginning of the apparent second band yielded drastically different values of β in each image analyzed, likely due to the general difficulty of accurately calculating β at threshold.

4.4. Discussion

The spectrum observed here is consistent with previous the previously collected photoelectron spectra of CHO_2^-.[77,78] While the onset we observe in this work at ~3.3 eV is lower eBE than the reported EA of 3.4961 eV, hot bands have been observed in photodetachment from CHO_2^- which could account for the discrepancy, especially when considered alongside the lower resolution in the spectrum reported in this chapter. The positive identification of the formyloxyl spectrum can be made through the anisotropy

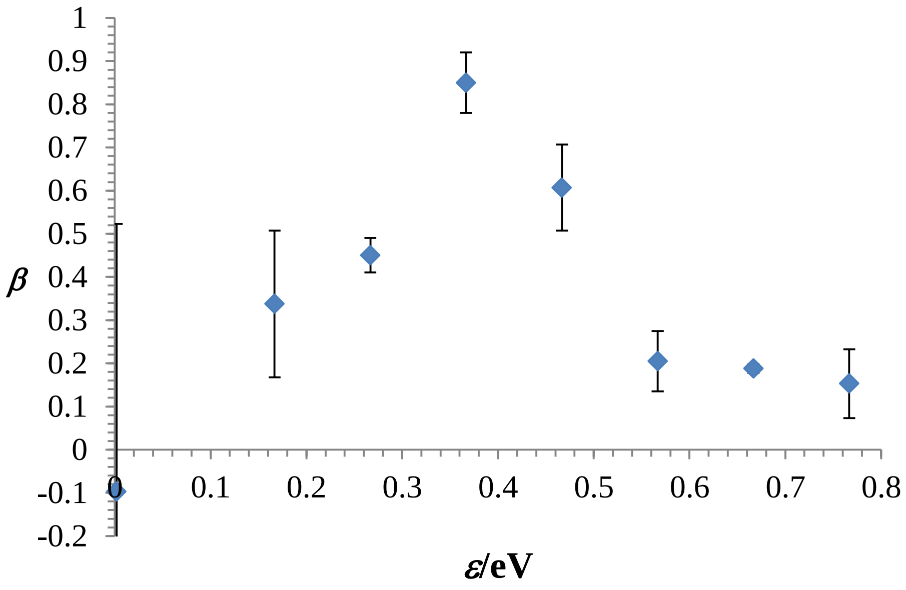

Figure 4.3. Photoelectron anisotropy parameter, *β*, as versus electron kinetic energy, *ε*.

analysis, which indicates that two states contribute to the band we see, with the apparent onset of a third near the zero-kinetic-energy threshold. The predominantly parallel anisotropy is consistent with detachment to the $X\ ^2A_1$ ground state of CHO_2, as previously reported. Evidence of a more isotropic band convoluted with the ground state band is seen in the more isotropic β values observed on the tails of the band.

Unfortunately, because the electronic states cannot be resolved from each other in the photoelectron images collected in this work, modeling the anisotropy parameters with the model functions described in Figure 4.1 is not possible. With two different electronic states contributing to each slice of the spectrum, state-specific β values cannot be determined.

Correcting for the field distortions which led to the elliptical distortions in the image will improve the resolution somewhat, but likely not enough to adequately resolve the vibronic structure to distinguish peaks from different electronic states from one another. Modifications to the instrument will be necessary to achieve the resolution observed in the photoelectron spectroscopy and SEVI spectra discussed in the introduction of this chapter.

4.5. Conclusions and Future Directions

A photoelectron image of CHO_2^- at 306 nm is reported in this chapter, with the identity of the molecule confirmed with an analysis of each the photoelectron spectrum and the PAD, matching each the position of the vertical transition observed at 3.59 eV, and the parallel PAD consistent with previous work[77,78] on the molecule. However, because of the spectral overlap of two different electronic bands in the image, it is not possible to model β as a function of ε using the Generalized Mixed Character Model and the model functions described in Figure 4.1.

To allow such analysis in the future, it will be necessary to resolve individual vibrational/electronic transitions, which requires performing the experiment in a high-resolution regime. In order to achieve this regime, it will first be essential to correct the VMI field distortions which led to the ellipticity of the raw images reported here. This ellipticity spreads individual transitions over wider radial ranges, reducing the resolution. While the images reported here were circularized, the process of circularization requires the program to identify rings in the image corresponding to transitions to work effectively,[66] and the congested photoelectron spectrum of CHO_2^- reduces the efficacy of this approach. Collecting images which require no correction for VMI field distortions would provide better resolution than correcting a distorted image.

The resolution gains from correcting this field distortion will likely be small, however, and a significant modification of the instrument or data collection software may be necessary. These modifications include: aligning the VMI in the line of the ion beam rather than perpendicular to it, reducing the spectral convolution imparted by the velocity spread in the ion packet;[80] and skimming the expansion and/or the ion beam to narrow both the spatial and velocity distributions of the ion packet. These modifications will be discussed in more detail in Chapter 6. Even these straightforward changes to the apparatus may not be sufficient, however, requiring the experiment to be performed with a scannable laser in the slow-photoelectron VMI regime, which would in turn limit our ability to study the behavior of β as a function of electron kinetic energy, ε.

In the context of the thesis of the full dissertation, however, the unambiguous identification of formate in the mass spectrum produced by methanol seeded in an oxygen carrier gas is significant evidence of unexplored gas-phase chemistry between methoxide and oxygen, and informs the work reported in Chapter 5, which follows.

CHAPTER 5: INVESTIGATING THE CHEMISTRY OF METHOXIDE AND OXYGEN THROUGH THE $CH_3O_3^-$ INTERMEDIATE

5.1 Introduction

In this chapter, we focus on the reactivity of the methoxide anion with oxygen. A brief overview of the known chemistry involving these species was provided in Section 1.1. Here we delve deeper into this chemistry, building on the previous work, and highlight the unanswered questions which arose in the process of these present investigations.

The known reaction of methoxide and oxygen produces the hydroperoxide anion and formaldehyde (Equation 1.1b), proceeding by hydride transfer.[5,9] The potential energy surfaces of this reaction, each for reaction of methoxide with each the triplet ground state ($X\ ^3\Sigma_g^-$) and the singlet excited state ($a\ ^1\Delta_g$) of oxygen were calculated by Lin, *et al* in order to better elucidate the mechanism of this reaction from kinetic data.[5] The energies of alternate products, summarized in Equation 5.1 below, were also calculated.

$$CH_3O^- + O_2^- \rightarrow CH_2O + HO_2^- \qquad (5.1a)$$

$$\rightarrow e^- + CH_2O + HO_2 \qquad (5.1b)$$

$$\rightarrow CH_3O + O_2^- \qquad (5.1c)$$

$$\rightarrow CH_2OH + O_2^- \qquad (5.1d)$$

$$\rightarrow CH(O)OH^{-} + OH \qquad (5.1e)$$

$$\rightarrow CH_2(O)OH^{-} + O \qquad (5.1f)$$

$$\rightarrow \textit{trans}\text{-}CH(O)O_2^{-} + H_2 \qquad (5.1g)$$

$$\rightarrow \textit{cis}\text{-}CH(O)O_2^{-} + H_2 \qquad (5.1h)$$

$$\rightarrow CH_3 + O_3^{-} \qquad (5.1i)$$

In addition to these products, the properties of several intermediates were also calculated, some of which are further explored in this work.

The reactions of various small anions, including CH_3O^{-}, with oxygen were previously studied by selected ion flow tube mass spectrometry (SIFT-MS) by Midey *et al.*[9] Two reaction paths for methoxide with oxygen were observed, those described in Equations 5.1a and 5.1b, in a nearly even split slightly favoring the products in Equation 5.1a, 52% to 48%.

On the neutral surface, the methoxy radical ($CH_3O^{\bullet}$) reacts with oxygen in an analogous process, forming the hydroperoxy radical and formaldehyde by hydrogen abstraction (Equation 1.1a).[7,8] An alternate mechanism was proposed, which proceeds through a $CH_3OOO^{\bullet}$ trioxy radical intermediate; however, this species has never been observed, and the most recent computational work suggests the energy barrier to form the trioxy radical is much larger than the barrier for hydride transfer.[8]

Atmospheric oxidation reactions of VOCs are often complex reactions with multiple branches, and are notoriously difficult to completely characterize.[2,3,6] Methoxide is unlikely to be an exception to this rule, and there is considerable work to be done in identifying and characterizing alternate reaction paths for this species with oxygen. The work of this chapter explores the potential for either an unexpected intermediate in the known reaction described in Equation 5.1a, or a new reaction path altogether.

5.2 Specific Methods

5.2.1 Experimental Methods

Each the electron gun and electron cannon were used for this work. The species with mass 63 amu was observed in the mass spectrum using both methods. Photoelectron images were collected at 406 nm and 355 nm for the anion produced by the electron gun, and at 306 nm and 296 nm using the electron cannon. Additionally, mass spectrometry of fully deuterated methanol (CD_3OD) seeded in O_2 was performed using the electron cannon.

5.2.2 Computational Methods

All calculations were completed in the Q-Chem 5.1 program.[81] Geometries of all structures considered in this work were optimized for both the neutral and the anion using the coupled-cluster theory with single and double excitations (CCSD), with the aug-cc-pVDZ basis set. Electron affinities (EAs) were calculated by subtracting the energy of the geometry-optimized anion from the energy of the geometry-optimized neutral molecule. No zero-point vibrational energy corrections are included in the reported calculated values. For neutral clusters, the usual assumption was made that the van der Waals interactions are negligible in strength, compared to the ion-neutral solvations interactions, and hence the energy of the neutral was assumed to be the sum of that of the two non-interacting molecules.

Vertical detachment energies (VDEs) were calculated using the Equation-of-Motion (EOM), where the "motion" is through Fock space, Ionization-Potential (IP) method,[82] combined with the coupled cluster theory (CCSD), i.e. EOM-IP-CCSD, with the aug-cc-pVDZ basis set. Additionally, excited states of the dihydoxymethanolate and $1\lambda^1,2\lambda^3,3\lambda^1$-trioxidane anions were explored with the EOM-EE-CCSD/aug-cc-pVDZ method, where EE denotes the Excitation Energy variant of the EOM approach.[82]

5.3 Results

5.3.1 Mass Spectra

The mass-spectra of the negative ions generated using a CH_3OH precursor seeded in O_2 carrier gas are shown in Figure 5.1a and b. These spectra, collected using the electron cannon and electron gun, respectively, indicate that the gun and the cannon produced largely the same ion chemistry. There are some differences in relative intensities between the electron-gun and electron-cannon mass-spectra, but these can be attributed to the different focusing conditions required in order to fully capture the mass ranges shown. Limiting the data collection to a narrower mass window achieves similar relative intensities in those windows for both ion-generation methods.

The mass spectra are calibrated using the O_2^- and O_4^- peaks at 32 amu and 64 amu, respectively. Other noteworthy peaks include those at mass-to-charge 31 amu, corresponding to the methoxide anion (CH_3O^-); 33 amu, corresponding to the hydroperoxide anion (HO_2^-) discussed in the Chapter 3; 45 amu, corresponding to the

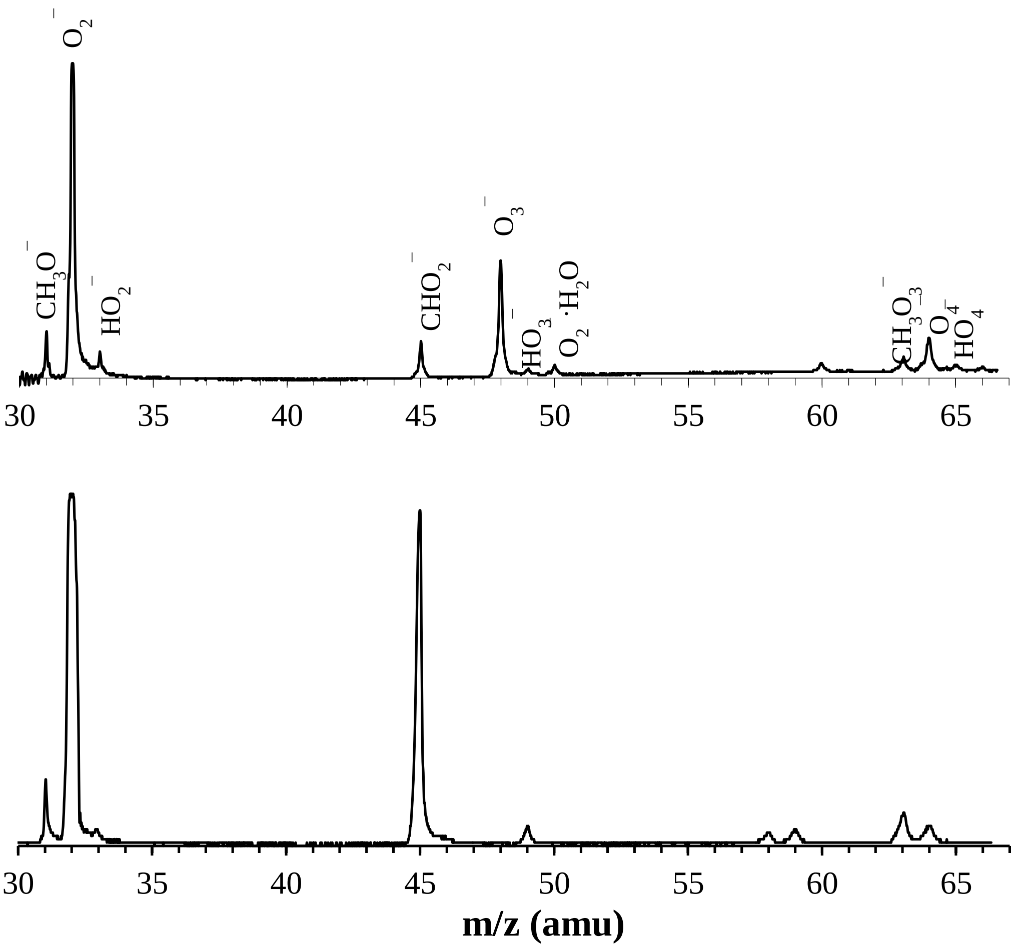

Figure 5.1. Mass spectra of CH_3OH seeded in O_2 carrier gas collected with a) the electron cannon setup, and b) the electron gun setup. Relevant mass peaks are labeled on the mass spectrum in a).

formate anion (CHO_2^-), discussed in Chapter 4; 48 amu, corresponding to O_3^-; 49 amu, corresponding to HO_3^- and/or CH_3O^- monosolvated by water; 50 amu, corresponding to O_2^- monosolvated by water; 65 amu, corresponding to HO_4^-; and the peak of interest at 63 amu, corresponding to an unknown molecule with the molecular formula $CH_3O_3^-$.

In order to confirm the above molecular formula of the mass-63 anion, the ions were also generated using a fully deuterated methanol, CD_3OD, seeded in O_2 carrier gas. The corresponding mass spectrum produced using the electron cannon as the source of high kinetic energy electrons, is shown in Figure 5.2, focused on the mass region of interest. Some residual undeuterated methanol from previous experiments was persistent in the expansion, resulting in peaks at both 63 amu and 65 amu, but the peak at 66 amu ($CD_3O_3^-$), as well as the absence of peaks at 70 amu ($C_2D_7O_2^-$), 74 amu ($C_3D_{11}O^-$), and 78 amu ($C_4D_{15}^-$), confirms the molecular formula of the anion studied here as $CH_3O_3^-$/$CD_3O_3^-$, excluding any other species with the same molar mass and containing only carbon, hydrogen, and oxygen.

5.3.2 Photoelectron Spectra

The photoelectron images and corresponding photoelectron spectra of $CH_3O_3^-$ collected at each 295 nm, 306 nm, 355 nm, and 406 nm appear in Figure 5.3, shown on the same graph for comparison. For clarity, the same spectra are reproduced individually in Figure 5.4.

The adiabatic electron affinity (EA) is assigned at the onset of the photoelectron signal at 2.65 ± 0.10 eV, as determined from the 406 nm spectrum, for which the EA transition is best resolved (due to the lowest photon energy). In all spectra, two

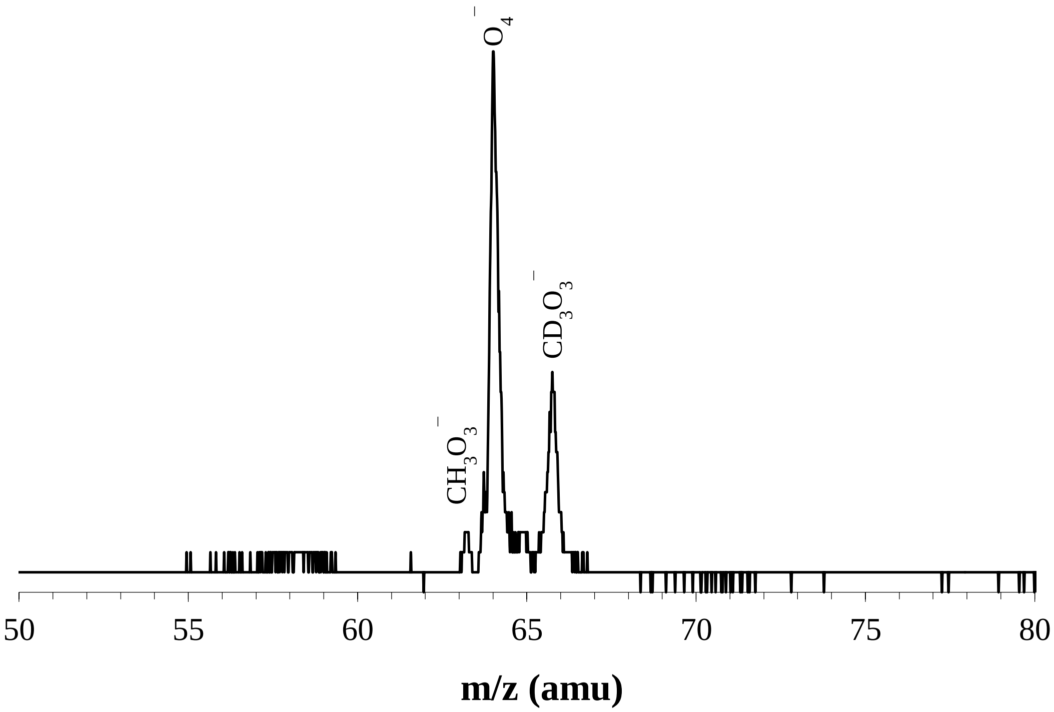

Figure 5.2. Mass spectrum of CD_3OD seeded in O_2 carrier gas collected with the electron cannon setup. Relevant mass peaks are labeled.

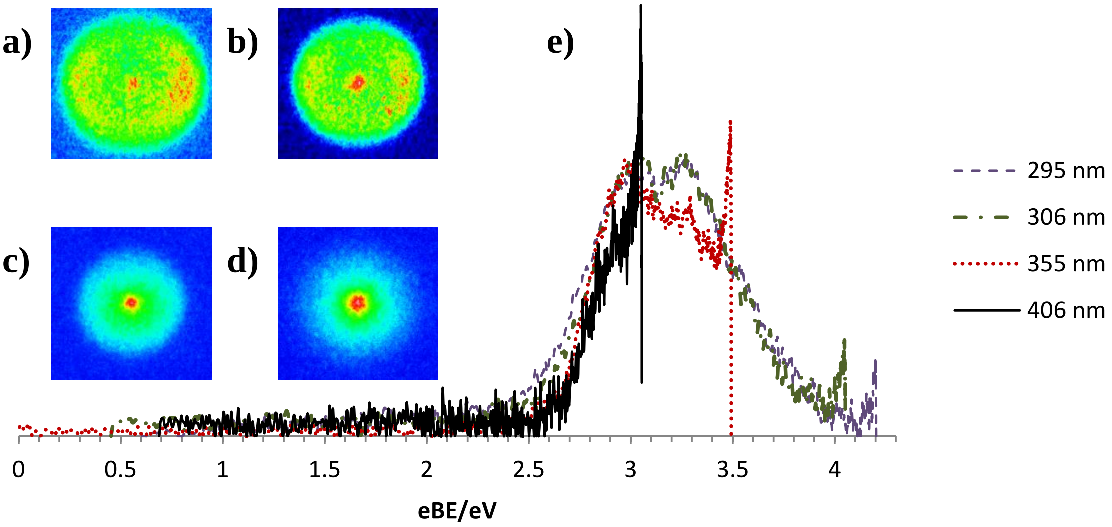

Figure 5.3. Photoelectron images collected at a) 295 nm, b) 306 nm, c) 355 nm, and d) 406 nm, and e) the corresponding photoelectron spectra. Onset of the spectrum, corresponding to the adiabatic electron affinity, is 2.65 eV, and two electron bands are observed, with vertical detachment energies of 2.93 eV and 3.20 eV. There is also an autodetachment feature observed at the zero kinetic energy threshold of each spectrum.

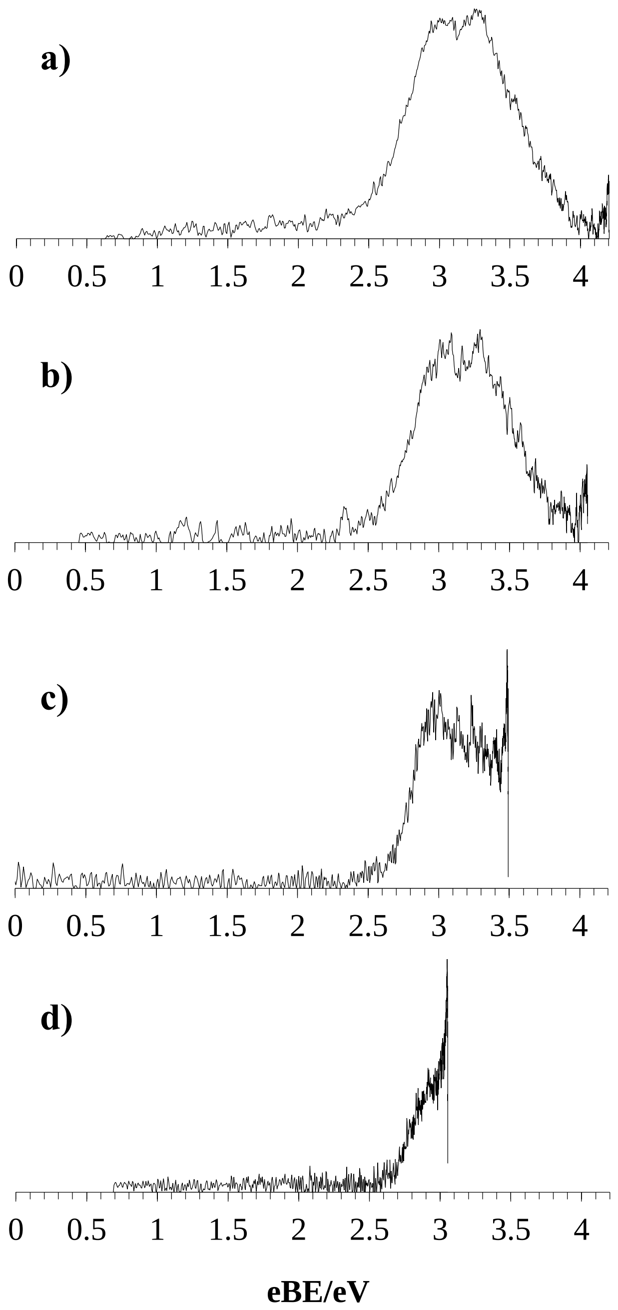

Figure 5.4. Photoelectron spectra collected at a) 295 nm, b) 306 nm, c) 355 nm, and d) 406 nm.

photodetachment bands can be discerned observed, with vertical detachment energies (VDEs) assigned at 2.93 ± 0.01 eV, and 3.20 ± 0.03 eV. These VDE values were determined by fitting the 295 nm and 306 nm spectra with two Gaussian functions and assuming that the position of each Gaussian's maximum corresponds to the VDE of one transition. The 355 nm spectrum was similarly modeled using three Gaussian functions, to account for the additional intense feature near the photon-energy spectral cutoff. This slow-electron feature appears in all four spectra, and is assigned to autodetachment. Relative to the other spectral bands, assigned to direct photodetachment transitions, the autodetachment feature has the largest intensity in the 406 nm and 355 nm spectra.

The photoelectron angular distributions, determined from the photoelectron images in Figure 5.3, become increasingly perpendicular with increasing electron kinetic energy, ε, which can be observed visually, comparing the nearly-isotropic image collected at 406 nm with the clearly perpendicular distributions in the 306 nm and 295 nm images. The corresponding ε-dependent anisotropy parameters, β, are plotted against ε in Figure 5.5, with the data corresponding to the first direct photodetachment band represented in blue, and those for the second in red. The $\beta(\varepsilon)$ values for both bands are plotted together on the same graph in order to demonstrate that both transitions appear to follow the same anisotropy trend.

5.4 Discussion

A survey of anionic structures corresponding to the molecular formula CH_3O_3 is presented in Figure 5.6. Without a clear difference in the β trends for the two bands, it is not possible to unambiguously assign them to different electronic states, leaving open the

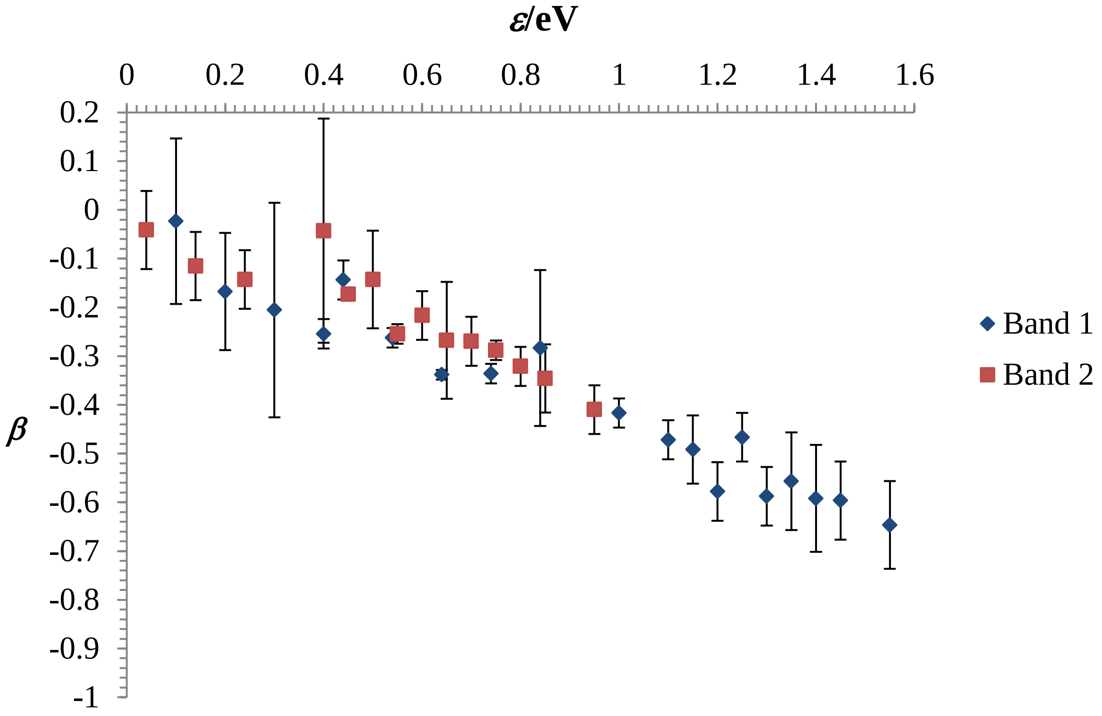

Figure 5.5. Photoelectron anisotropy parameters, *β*, against electron kinetic energy, *ε*. The band corresponding to the ground state is plotted in blue, and the excited state in red.

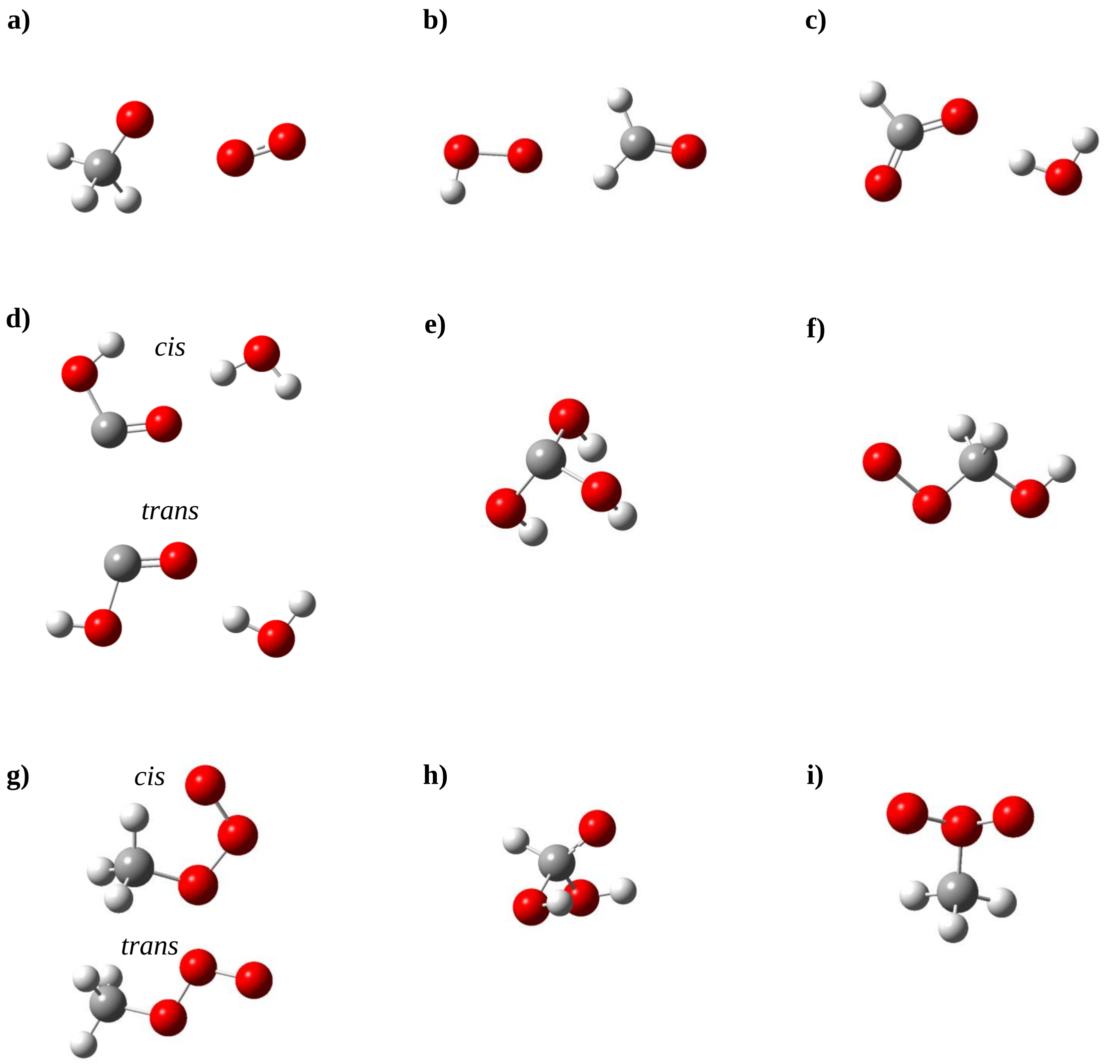

Figure 5.6. Survey of molecules tested for match to the observed photoelectron spectrum.

possibility of a vibrational progression broadened by interactions with a solvent molecule. These possibilities are explored in the species represented in Figure 5.6a-d. The six structures in Figure 5.6e-i, meanwhile, would represent detachment to two electronic states of the neutral, broadened by vibrations which cannot be resolved in this experiment. This work has narrowed the identity of the mass-63 species to two possibilities: the anion of dihydroxymethanolate (Figure 5.6h) and the anion of 2-methyl-$1\lambda^1,2\lambda^3,3\lambda^1$-trioxidane (Figure 5.6i). In this section, first the process by which the identity was narrowed to these two species is described, and then the evidence for each species—including the shortcomings of each in reasonably explaining the observed spectrum—are explored.

5.4.1 Elimination of Implausible Structures

Estimates of EAs and VDEs for the nine molecules proposed to account for the observed spectra are summarized in Table 5.1. For solvated species, a range for the EA is estimated by adding a typical solvation energy for the specific solvent molecule in the structure—accounting for potential cases of especially weak interaction, and setting a plausible upper limit based on previous work—to the previously measured electron affinity of the anion. Typical solvation energy for nonpolar solvents is ~0.3 eV, so we chose a range from a lower limit of 0.1 eV[83] to an upper limit of 0.5 eV for solvation by O_2. Likewise, solvation by the polar formaldehyde could be as weak as 0.5 eV (based on solvation of I^- by water, 0.45 eV)[84] and as strong as 0.8 eV (solvation of Cl^- by water, 0.76 eV),[84] but we set an upper limit in this work of 1 eV to account for the possibility of especially strong polar interactions. Finally, the solvation energy consequent of hydrogen-bonding interactions is given a range of 0.7 eV to 1.4 eV, the former based on

Structure	Anion Ground State	Energy wrt Reactants /eV	Exp.[a] EA/eV	EA/eV	VDE1/eV State	VDE2/eV State
a	$X\,^{3}\mathrm{A}$	–0.1197	1.7-2.1[83,85,86]	1.8660	1.5878 $X\,^{2}\mathrm{A}$	1.6040 $A\,^{2}\mathrm{A}$
b	$X\,^{1}\mathrm{A}$	–1.2762	1.6-2.1[60,61,87]	1.5284[b]	2.0013 $X\,^{2}\mathrm{A}$	2.7035 $A\,^{2}\mathrm{A}$
c	$X\,^{1}\mathrm{A}'$	–6.4966	4.2-4.9[77,78,88]	4.2540[b]	4.3169 $X\,^{2}\mathrm{A}'$	4.5164 $A\,^{2}\mathrm{A}'$
d ***cis***	$X\,^{1}\mathrm{A}'$	–4.9258	2.2-2.9[88-90]	1.5128	2.5779 $X\,^{2}\mathrm{A}'$	5.5982 $A\,^{2}\mathrm{A}''$
trans	$X\,^{1}\mathrm{A}'$	–4.8775	2.0-2.7[88-90]	1.6614	2.4188 $X\,^{2}\mathrm{A}'$	5.5167 $A\,^{2}\mathrm{A}''$
e	$X\,^{1}\mathrm{A}_1$	–3.1895		0.7558	1.7175 $X\,^{2}\mathrm{A}_1$	4.7006 $A\,^{2}\mathrm{A}_2$
f	$X\,^{1}\mathrm{A}$	–1.4847		1.1781	1.7161 $X\,^{2}\mathrm{A}$	2.4816 $A\,^{2}\mathrm{A}$
g ***cis***	$X\,^{1}\mathrm{A}'$	0.3847		1.3777	2.0330 $X\,^{2}\mathrm{A}''$	3.5453 $A\,^{2}\mathrm{A}''$
trans	$X\,^{1}\mathrm{A}'$	0.6808		1.1189	1.9898 $X\,^{2}\mathrm{A}''$	3.1194 $A\,^{2}\mathrm{A}'$
h	$X\,^{1}\mathrm{A}'$	–5.2971		2.8997	3.2845 $X\,^{2}\mathrm{A}'$	3.3832 $A\,^{2}\mathrm{A}''$
i	$X\,^{1}\mathrm{A}'$	1.6861		2.5741	2.7638 $X\,^{2}\mathrm{A}'$	3.1105 $A\,^{2}\mathrm{A}''$

	EA/eV	VDE1/eV	VDE2/eV
Experimental Spectra	2.65(10)	2.93(1)	3.20(3)

Table 5.1. Summary of proposed structures. EA calculations were completed in Q-Chem with anion and neutral geometries optimized at the CCSD/aug-cc-pVDZ level of theory. VDE calculations were completed in Q-Chem at the EOM-IP-CCSD/aug-cc-pVDZ level of theory.

[a]Estimated by adding 0.1-.05 eV for solvation by O_2, 0.5-1.0 eV for solvation by CH_2O, and 0.7-1.4 eV for solvation by H_2O to th epreviously measured electron affinity of the anion.

[b]Calculation on neutral dimer did not converge, so estimated EA by assuming zero interaction energy in the neutral dimer.

solvation of acetate ($CH_3CO_2^-$) by water (0.70 eV),[91] and the latter by the strong hydrogen-bonding dimer between OH^- and water (1.39 eV).[88] Computational results summarized in Table 5.1 were calculated in Q-Chem, with details described in Section 5.2.2.

The dimers in Figure 5.6a and 5.6b can be ruled out based on the mismatch of their estimated EAs and the observed spectra. The measured EA of CH_3O is 1.5690 ± 0.0019,[85,86] and a typical first solvation energy by O_2 is ~0.3 eV, which would correspond to an electron affinity of ~1.9 eV. This is consistent with the electron affinity calculated in Q-Chem of 1.8660 eV. Even allowing for atypically strong solvation which the calculation could not capture, it is unlikely the EA of this dimer would exceed 2.1 eV. The same argument applies to hydroperoxide solvated by formaldehyde. The EA of HO_2 measured in Chapter 3 and consistent with previous work[60,61] is 1.089 ± 0.011 eV. The calculation in Q-Chem predicts an EA for the solvated species of 1.5284 eV, and allowing for especially strong dipole-ion interaction[87] not captured in this calculation, the upper limit on the EA can be set at 2.1 eV, again inconsistent with the observed spectrum.

The formate anion (Figure 5.6c) corresponds to a measured electron affinity of 3.498 ±0.010 eV of the formyloxyl radical,[77-79] without even accounting for further stabilization of the anion by a solvent molecule. Solvation of the molecule by H_2O could shift the onset of the spectrum as high as 4.9 eV in the case of the formation of a strongly hydrogen-bonded dimer.[88] The Q-Chem prediction for the EA is 4.2540 eV, which is consistent with the first solvation energy of the structurally similar acetate anion ($CH_3CO_2^-$) by water, which has been measured at 0.70 eV.[91] Irrespective of the strength of the solvation interaction, though, the EA of formate being higher than the EA revealed in the spectra reported here allows us to rule it out.

The last solvated species explored here is $HOCO^-$ solvated by a single water molecule, i.e. $HOCO^-\bullet H_2O$ (Figure 5.6d). The calculated EAs for each the *cis* and *trans* isomer of HOCO are 1.5128 eV and 1.6614 eV, respectively—considerably below the onset of the observed anion photoelectron spectrum—but comparing these results to previous experiments suggests the calculations conceivably may not adequately capture these species. The measured EA of *cis*-HOCO is 1.51 ± 0.01 eV, and for *trans*-HOCO is 1.38 ± 0.01 eV,[89,90] and so the estimated range of possible EAs of these isomers in the presence of a solvent water molecule are 2.2-2.9 eV and 2.0-2.7 eV, respectively.[87,91] It is not unreasonable, therefore, to expect the actual EA to fall in the vicinity of 2.65 eV, the assigned EA of the spectra observed in this work. However, the previously reported vibrational progression does not account for the two-band structure observed in this work, with contributions from the v_3, v_4, and v_5 vibrational modes of each isomer combing into six peaks with < 100 meV spacing.[89]

Furthermore, β values are reported at various ε for each isomer, and they are predominantly positive, corresponding to a PAD with larger intensity parallel to the laser polarization direction.[89] While solvent interactions can affect photoelectron anisotropy by polarizing the parent orbital, such a complete change in the character of the outgoing electron wave is unlikely for interaction with a single solvent molecule.[38]

Finally, while a peak is observed in the mass spectrum (Figure 5.1) at 45 amu, consistent with the molecular formula CHO_2, photoelectron imaging of this peak yielded only evidence of the formate anion, with no indication of the HOCO spectrum, as shown in Chapter 4 (Figure 4.2). Since $HOCO^-$ is by itself a stable anion, the presence of $HOCO^-{\bullet}(H_2O)$ in the mass spectrum should coincide with the presence of unsolvated $HOCO^-$ in some significant quantity, yet this is not the case. The combination of these factors leads us to rule out $HOCO^-{\bullet}H_2O$ as a possible explanation for the observed spectra.

The molecules represented in Figure 5.6e-i do not have past experimental work to reference, so our *ab initio* calculations provide the entire argument regarding their plausibility. Trihydroxymethanide (Figure 5.6e) has a calculated EA of 0.7558 eV and first VDE of 1.7175 eV, neither or which are consistent with the measured spectrum. Likewise, methanolperoxide (Figure 5.6f) has a predicted EA of 1.1781 eV and first VDE of 1.7161 eV—again inconsistent with the observed photoelectron spectrum. Two isomers of 1-methyl-3λ^1-trioxidane (Figure 5.6g) also have calculated EA (1.3777 eV *cis*, 1.1189 eV *trans*) and first VDE (2.0330 eV *cis*, 1.9898 eV *trans*) inconsistent with the spectrum, and are also less energetically stable than the methoxide anion plus an oxygen molecule, which would have to react to form it. Therefore these three molecules can also be ruled out, leaving only dihyroxymethanolate (Figure 5.6h) and 2-methyl-1λ^1,2λ^3,3λ^1-trioxidane (Figure 5.6i) as two plausible candidates for the reported spectra. These species are discussed in detail in the following sections.

5.4.2 Dihydroxymethanolate

The dihydroxymethanolate anion, shown in Figure 5.6h, is energetically more stable than any of the structures explored in this work, except for the formate-and-water dimer species. It is calculated to be 5.2971 eV lower in energy that the methoxide and oxygen reactant molecules. The calculated EA of 2.8997 eV is in reasonable agreement with the assignment of the experimental EA of 2.65 eV. Similarly, the first two VDEs calculated, 3.2845 eV for detachment to the neutral ground state, $X\ ^2\mathrm{A}'$, and 3.3832 eV for detachment to the first neutral excited state, $A\ ^2\mathrm{A}''$, agree well with the spectrum. The EA and VDE calculations are summarized alongside those for $1\lambda^1,2\lambda^3,3\lambda^1$-trioxidane in Table 5.2, for ease of comparison.

The proposed structure of the dihydroxymethanolate anion (Figure 5.6h) is the conjugate base of trihydroxymethane, a hypothetical molecule also referred to as orthoformic acid. The dihydroxymethanolate anion is obtained by deprotonating one of the hydroxy groups of the acid. Trihydroxymethane itself has never been detected, and is expected to rapidly decompose into formic acid and water.[92,93] If analogous chemistry can be expected in the deprotonated species, i.e. the anion dihydroxymethanolate, then the presence of a strong formate signal in the mass spectrum—appearing at mass-to-charge 45 amu in the mass spectrum and confirmed through photoelectron imaging (Chapter 4)—may be evidence to the identity of the species observed at mass-to-charge 63 amu corresponding to dihydroxymethanolate. Further evidence could be gleaned from a higher photon energy experiment, not just to exceed the EA of the formate-and-water dimer, but to distinguish it from the autodetachment peak which appears at threshold. As explained in Section 5.4.1, the electron affinity of $CHO_2^-\bullet(H_2O)$ is likely in excess of 4.2 eV, based on both photoelectron spectroscopy work on CHO_2^- itself[76-79] and water-solvated species in general,[87,88,91] and on the computations completed in this work. In our lab, the highest photon energy available at present is 4.66 eV (the fourth harmonic of the

Experimental Results		**dihydroxymethanolate**				**$1\lambda^1,2\lambda^3,3\lambda^1$-trioxidane**			
		Calculations from Table 4.1		**EOM-EE-CCSD/ aug-cc-pVDZ**		**Calculations from Table 4.1**		**EOM-EE-CCSD/ aug-cc-pVDZ**	
	E/eV	Transition	Excitation Energy/eV	State	Excitation Energy/eV	Transition	Excitation Energy/eV	State	Excitation Energy/eV
EA	2.65(10)	EA	2.8997	$A\ ^{1}\mathrm{A}'$	4.1387	EA	2.5741	$A\ ^{1}\mathrm{A}'$	3.4709
VDE 1	2.93(1)	VDE $X\ ^{2}\mathrm{A}'$	3.2845	$B\ ^{1}\mathrm{A}''$	4.1560	VDE $X\ ^{2}\mathrm{A}'$	2.7638	$B\ ^{1}\mathrm{A}''$	3.8102
VDE 2	3.20(3)	VDE $A\ ^{2}\mathrm{A}''$	3.3832	$C\ ^{1}\mathrm{A}'$	4.4691	VDE $A\ ^{2}\mathrm{A}''$	3.1105	$C\ ^{1}\mathrm{A}''$	3.9958
		VDE $B\ ^{2}\mathrm{A}''$	5.1533	$D\ ^{1}\mathrm{A}''$	4.6123	VDE $B\ ^{2}\mathrm{A}''$	3.6917	$D\ ^{1}\mathrm{A}'$	4.0974
		VDE $C\ ^{2}\mathrm{A}'$	5.8326			VDE $C\ ^{2}\mathrm{A}'$	3.8423		

Table 5.2. Summary of calculations for dihydroxymethanolate and $1\lambda^1,2\lambda^3,3\lambda^1$-trioxidane.

Nd:YAG laser), which could both access this dimer and distinguish it from the autodetachment feature from the $CH_3O_3^-$ species observed in the spectra reported in this work, provided the strength of the hydrogen-bonding interaction does not approach that observed in the OH^- and water dimer. However, when this experiment was attempted, no signal for either species (the spectra reported here, or the formate-and-water dimer) was observed above the noise level.

The good agreement between the calculations and experimental spectrum, as well as the potential connection to the formate peak in the mass spectrum are compelling evidence to the assignment of the spectrum to dihydroxymethanolate; however, these arguments must be weighed against the chemical feasibility of generating the ion in the first place, and this inspection weakens the argument considerably.

Since none of the anion, neutral radial, or protonated neutral species (conjugate acid) has been observed, the evidence of its existence must be unambiguous, but the chemistry to produce the anion has never been observed in our experiment previously. The chemistry in the supersonic expansion favors reactions which require as few collisions as possible, which casts doubt on the possibility of forming two new carbon-oxygen bonds and two more oxygen-hydrogen bonds at the expense of carbon-hydrogen bonds. This would either correspond to multiple reactive collisions to break apart the methanol/methoxide and reform the dihydroxymethanolate anion, or the insertion of two oxygen atoms into carbon-hydrogen bonds in methoxide. Neither process is kinetically likely, and especially challenges the efficiency of its formation as borne out in the favorable relative intensity of $CH_3O_3^-$ to CH_3O^- in the mass spectrum, despite the latter only requiring a single deprotonation reaction to form.

Additionally, using the EOM-EE-CCSD method with the aug-cc-pVDZ basis set to elucidate anion excited states, which could explain the autodetachment peak, no states consistent with intense autodetachment in the 406 nm and 355 nm spectra were found. These results are also summarized in Table 5.2.

5.4.3 $1\lambda^1,2\lambda^3,3\lambda^1$-trioxidane

The second structure for which the calculations match well with the observed spectrum is $1\lambda^1,2\lambda^3,3\lambda^1$-trioxidane (Figure 5.6i). The corresponding electron affinity of the neutral molecule calculated at the CCSD/aug-cc-pVDZ level of theory is 2.5741 eV, a good match to the experimental result. Likewise, the first two VDEs of the $X\ ^1\mathrm{A}'$ anion match the spectrum well: 2.7638 eV for detachment to the ground $X\ ^2\mathrm{A}'$ state of the neutral, and 3.1105 eV for the excited $A\ ^2\mathrm{A}''$ state. Furthermore, in order to explain the presence of the autodetachment peak, a calculation to identify excited states of the anion at the EOM-EE-CCSD/aug-cc-pVDZ level of theory returned four spin-allowed transitions accessible with the photon energies used in this work, summarized in Table 4.2. The first excited state, $A\ ^1\mathrm{A}'$, is nearly resonant with the 355 nm photon, with an excitation energy of 3.4709 eV, and if this state is dissociative, it would be consistent with the autodetachment observed in the photoelectron spectra reported here.

While it has never been detected, this structure has also been proposed in previous computational work as an intermediate on the potential energy surface of the reaction between methoxide and oxygen in its excited state, $a\ ^1\Delta_g$.[5]

Despite the strong agreement between the *ab initio* calculations and the observed photoelectron spectrum, there are two persuasive counter-arguments to acknowledge, as well. The first is the prediction of two more excited states accessible with the photon energies used in this work which were not observed clearly in our photoelectron spectra. These states of the neutral, $B\ ^2A''$ and $C\ ^2A'$, have calculated VDEs of 3.6917 eV and 3.8423 eV, respectively. The first of these transitions may be obscured by the tail of the first excited state, but the VDE of the second lies in the region between the second band and the autodetachment peaks in the 295 nm and 306 nm spectra, and should be observable, in principle. To be sure, its signal may be suppressed by Wigner scaling of the electronic cross-sections, for lying so close to the zero electron kinetic energy threshold. With that in mind, the absence of these predicted excited states in the observed spectra is not disqualifying in itself, but it must be considered alongside other evidence contradicting the assignment of the spectrum to this species.

The second, more substantial element of the calculations, which casts doubt on the proposal of $1\lambda^1,2\lambda^3,3\lambda^1$-trioxidane as the observed mass-63 anion is the relative energy of this anion with respect to the reactants needed to form it. The calculations predict that this anion species is uphill in energy by 1.6861 eV from methoxide and oxygen in its triplet ground state. However, a spin-conserving reaction of methoxide (singlet) with triplet oxygen would yield the $1\lambda^1,2\lambda^3,3\lambda^1$-trioxidane anion in the excited triplet state. As discussed before by Lin, *et al*,[5] a spin-conserving process yielding singlet $1\lambda^1,2\lambda^3,3\lambda^1$-trioxidane would have to proceed on a singlet potential energy surface, most plausibly corresponding to the reaction between methoxide and oxygen in its excited state, $a\ ^1\Delta_g$. In the supersonic expansion of O_2 bombarded by high-energy electrons from the electron gun/cannon, it is conceivable to generate a significant density of the $O_2(a\ ^1\Delta_g)$ reactants, so such a process cannot be ruled out. However, the triplet→singlet excitation energy in O_2 is well known to be 0.977 eV, indicating that even the reaction of $O_2(a\ ^1\Delta_g)$ with methoxide to yield the $1\lambda^1,2\lambda^3,3\lambda^1$-trioxidane anion in its ground singlet state is still endothermic by about 0.7 eV.

The above analysis agrees with the calculations of Lin, *et al*, which place $1\lambda^1,2\lambda^3,3\lambda^1$-trioxidane higher in energy even than methoxide and oxygen in its excited singlet state,[5] making its formation in the observed intensity thermodynamically unlikely. Additionally, the $1\lambda^1,2\lambda^3,3\lambda^1$-trioxidane anion seems likely to decompose into a methyl radical plus O_3^-. To this end, the lack of consistent presence of O_3^- in the mass spectrum, compared to the consistently-intense mass-to-charge 63 amu peak, suggests that different chemistry may be accessed.

5.4.4 Answering the Question

In Figure 5.1a, where the electron cannon setup is used, there is a significant amount of O_3^-, and a small formate peak, whereas these two species have the opposite relative intensities in the mass spectrum collected with the electron gun setup in Figure 5.1b. This is true even when the mass region where these peaks appear is focused specifically. Meanwhile, focusing on $CH_3O_3^-$ yields roughly the same relative intensity in both experimental setups, suggesting either a chemical pathway inconsistent with both species proposed in this work, or decomposition processes more sensitive to the source conditions than the formation chemistry. As such, finding other species to explore to explain the observed spectrum may prove necessary. The anisotropy data in Figure 5.5, which show no significant difference in the PADs of detachment to the ground and excited states, may also indicate these two bands belong to a vibrational progression in the same electronic state, which makes dimer species especially promising for this direction.

If one of the two structures explored in this work does account for the spectrum, however, which is the species observed may be determined through a photofragmentation experiment. This was attempted, but no photofragments were conclusively detected, and the instrument capable of fragmentation is currently being operated in a configuration which does not allow the experiment to be attempted again. However, with successful photofragmentation, the masses of these fragments would give insight into the connectivity of the molecule. For example, a photofragment with mass-to-charge 48 amu would correspond to O_3^-, clear evidence of $1\lambda^1,2\lambda^3,3\lambda^1$-trioxidane, which contains that motif. Absent evidence specific to either of these structures, the observed photofragments could also provide clues to propose new structures to explore, as well.

5.5 Conclusions

The photoelectron spectrum of an unknown molecule with the formula $CH_3O_3^-$ is reported here. The EA is assigned to 2.65 ± 0.10 eV, and the VDEs of the two bands observed are 2.93 ± 0.01 eV, and 3.20 ± 0.03 eV. Nine species, four of them dimer anions, and the other five molecular anions, were explored as possibilities to explain the observed spectrum, with only dihydroxymethanolate and $1\lambda^1,2\lambda^3,3\lambda^1$-trioxidane producing computational results consistent with the measured spectrum. Neither of these species could be assigned unambiguously as the molecule corresponding to the photoelectron spectrum, however, and further investigation will be necessary to make a robust molecular identification and spectral assignment.

CHAPTER 6: SUMMARY AND FUTURE DIRECTIONS

6.1. Summary of this Work

In this dissertation, I explored the chemistry of methoxide and oxygen. This chemistry first produced and allowed for the study of HO_2^- in Chapter 3, modeling photoelectron angular distributions for photodetachment from each the a'' HOMO and a' HOMO−1 as *p*-*d* mixed-character orbitals. The photodetachment anisotropy was investigated as a function of electron kinetic energy, in the context of the mixed-state model[44] for detachment to each the ground, $X\ ^2A''$, and excited, $A\ ^2A'$, states of the neutral HO_2 radical. These results provided insight into the chemical bonding within the anion and radical species, which is intrinsically related to their respective electronic structures. The most reactive molecular orbitals of the anion (HOMO and HOMO−1) were explored in the context of symmetry arguments, with the observed ε-dependence of the photoelectron anisotropy parameter, β, modeled using the *p*-*d* variant of the mixed-state model. Comparison of the results for HO_2^-, which belongs to the C_s point group, to those for O_2^- ($D_{\infty h}$) and NO^- ($C_{\infty v}$) tested the limit of the model approach and provided insight into the effects of breaking symmetry the bonding structures, photodetachment process, and PADs, in particular. Additionally, the quantitative description using the *p*-*d* case of the Generalized Mixed Character Model was compared to the qualitative *s*&*p* model, which models PADs as symmetry-allowed transitions to *s* and *p* outgoing free electron waves.[36]

The *p*-*d* model function was fit to the observed anisotropy trends for each the HOMO and HOMO−1 of HO_2^-, yielding a quantitative estimate of their fractional *d*-

character, γ_d. The deviations of γ_d from the "perfectly" d-like case of O_2^- provide an important measure of the effects of the additional H–O bond in HO_2^- on the structures of the predominantly oxygen-based orbitals. To this end, γ_d values of 0.979 for the a'' HOMO and 0.871 for the a' HOMO−1 provide a clear indication of the degeneracy lifting for the (predominantly) π^* orbital localized on O_2^-. The in-plane HOMO−1 is more perturbed by the bond to the neighboring H-atom than the out-of-plane HOMO, due to the increased contribution of the hydrogen atom and the partial bonding character of the orbital with respect to the O–H bond. Such degeneracy lifting is often discussed in terms of orbital energies only; our work shed additional light on the lifting of the degeneracy in terms of the MO structures (shapes) themselves. It is also instructive to note that the polarization of the HOMO in HO_2^- is also greater compared to the degenerate HOMO of NO^-, for which γ_d was previously determined to be 0.985.[44] At an all-important conceptual level, this dual pairwise comparison (HO_2^- versus O_2^- and HO_2^- versus NO^-) demonstrates that additional chemical bonds are more disruptive to the electronic structure than a slight mismatch in the electronegativities of two atoms.

While the mixed-state model provides a quantitative account for rather small—in some cases, even perturbative—differences between orbitals, the *s*&*p* model takes into account the absolute symmetry labels only,[36] thus failing to consider the great similarity of different-symmetry MOs in some cases. A perfect tutorial example of this is given by the application of the *s*&*p* model to the above a'' HOMO and a' HOMO−1 of HO_2^-. Within the context of a strictly symmetry-based description, these two orbitals are opposite in character, and therefore predicted to yield different-character PADs. In reality, however, despite the different symmetry species within the C_s point group, both orbitals are of predominantly π^* (*d*-like) character, and one needs to adopt the quantitative mixed-state description to adequately describe the differences between the respective detachment channels.

In Chapter 4, we demonstrated evidence of previously unexplored chemistry between methoxide and oxygen. A mass-to-charge peak of 45 amu was observed in the mass spectrum, and through analysis of its photoelectron image determined to be formate (CHO_2^-). The peak of the spectrum observed at 3.59 eV is consistent with the most intense peak observed in previous SEVI work on the system, corresponding to the combination of $3_0^1(^2A_1)$ and $6_0^1(^2A_1)$ transitions, at an eBE of 3.5660 eV.[77,78] Additionally, the parallel PAD of this main feature, consistent with detachment from the a_1 MO of CHO_2^-, and the sharp drop to more isotropic anisotropy on the tails of the feature is consistent with the nearly-degenerate detachment to the excited electronic state of CHO_2, $A\ ^2B_2$, provides further evidence the observed photoelectron image is consequent of photodetachment from the formate anion. The onset of a third electronic band, $B\ ^2A_2$, can be seen near the photon energy threshold.

While the PADs resulting from photodetachment from the two highest-lying occupied MOs of CHO_2^- lend themselves to analysis using the Generalized Mixed Character Model, and the third MO by the $l = 2$ case of the Cooper Zare Equation (Eq. 1.6), the energy resolution was in this case was insufficient to determine state-specific values of β for detachment to the ground and first excited electronic states of CHO_2, and the photon energy used in this work was insufficient to study detachment to the second excited electronic state of CHO_2. This state could be accessed using the fourth harmonic of the Nd:YAG laser (266nm), but photoelectron signal was not found at that wavelength. However, the unambiguous assignment of the spectrum is significant in itself, as it both demonstrates a new method for generating formate anions in the gas phase, and provides unambiguous evidence of new chemistry between CH_3O^- and O_2.

The final project reported in this dissertation is described in Chapter 5, in which the photoelectron spectrum of a mass-63 anion with the molecular formula $CH_3O_3^-$ is reported. Photoelectron images were collected at 406 nm, 355 nm, 306 nm, and 295 nm. The EA was assigned to the onset of the spectrum collected at 406 nm, 2.65 ± 0.10 eV, and the VDEs of the two bands were determined to be 2.93 ± 0.01 eV and 3.20 ± 0.03 eV, respectively, by fitting Gaussian functions to the spectra collected at 355 nm, 306 nm, and 295 nm. Additionally, an autodetachment feature was observed in all four spectra, and was most intense in the 406 nm and 355 nm spectra. A mass spectrometry experiment using CD_3OD in O_2 confirmed the molecular formula, and the photoelectron spectrum of $CH_3O_3^-$ was compared to both past experimental results and computations completed for this work to determine the identity of the molecule.

Of the numerous bonding structures explored in for the $CH_3O_3^-$ anion, two were most consistent with the observed photoelectron spectrum. They are dihydroxymethanolate, and $1\lambda^1,2\lambda^3,3\lambda^1$-trioxidane. Neither of these molecules have been observed experimentally in the past.[5,92,93] Calculations provided a fair match of the EA and anion VDEs for dihydroxymethanolate to the experimentally observed values, but no excited states of the anion consistent with the observed autodetachment were found.

Moreover the anion itself, while energetically stable, would require kinetically unlikely chemistry to be formed.

Meanwhile, the calculations provided a near-perfect match between theory and experiment for the EA and first two anion VDEs for $1\lambda^1,2\lambda^3,3\lambda^1$-trioxidane. Additionally, an excited state of the anion predicted to lie 3.4709 eV above the ground state, was consistent with the observed autodetachment feature. However, this molecule is also energetically unstable with respect to the CH_3O^- and O_2 reactants, which is inconsistent with the efficiency with which it is formed as born out in the intensity of the peak in the mass spectrum. Therefore, we hesitate to provide an unambiguous assignment of the photoelectron spectrum to either of these molecules. More work will need to be completed in order to positively identify the molecule observed in these photoelectron images.

Overall, this work has leveraged the power of photoelectron imaging both to better understand the process of photodetachment through quantitative analysis of PADs, as well as to explore both known and previously undiscussed chemistry being the methoxide anion and oxygen gas.

6.2. Projects with Preliminary Data

Some preliminary data were collected on two systems not reported on in the body of this dissertation. These are presented in this section so their questions can be pursued further in the future.

6.2.1. HO_4^-

Superoxide adduct species, HO_3^-, HO_4^-, and HO_5^-, are proposed as intermediates in the peroxone process,[57,58] briefly discussed in Subsection 3.1.1. Two of these species, HO_3^- and HO_4^-, were observed in the mass spectrum in Figure 5.1. While no photoelectron signal could be found for HO_3^-, some images were collected of HO_4^- at 406 nm, but the signal was too weak to properly analyze, and the ions could not be generated in sufficient quantity to detect photoelectron signal again. The image and the corresponding photoelectron spectrum are shown in Figure 6.1. Due to the weak signal and the significant contribution of noise to the measured spectrum, no spectral features can be adequately discerned.

6.2.2. Mass-62 amu Anion

While conducting the experiments on $CH_3O_3^-$ described in Chapter 5, a peak was observed in the mass spectrum at 62 amu (Figure 6.2). Photoelectron images were collected of this species 306 nm, 355 nm, and 532 nm, and these images and their corresponding photoelectron spectra are shown together in Figure 6.3, and the spectra are presented separately in Figure 6.4. The spectrum appears to have an onset at about 1.3 eV, with the maximum of the band around 2.4 eV, as determined from the 306 nm spectrum. The PAD is predominantly parallel throughout the entire band in the images collected at each wavelength, though photoelectron anisotropy parameters were not calculated.

In order to determine the identity of the molecule which produced these photoelectron spectra, the experiment was attempted with deuterated methanol, CD_3OD,

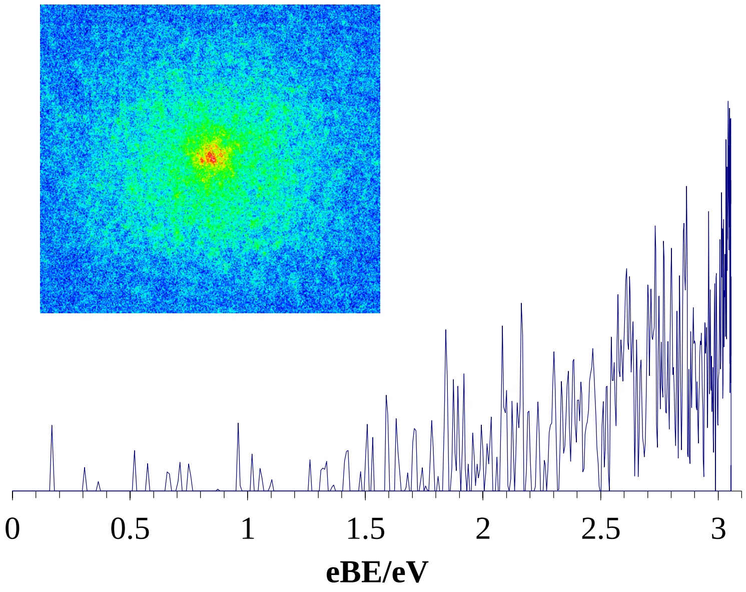

Figure 6.1. Photoelectron image and the corresponding photoelectron spectrum of HO_4^- at 406 nm.

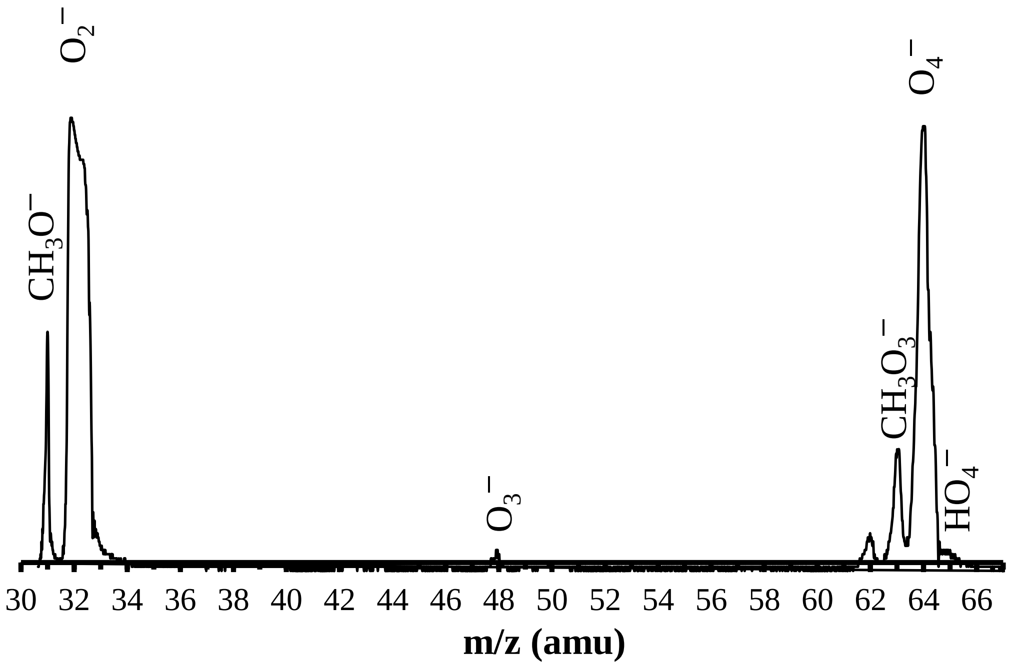

Figure 6.2. Mass spectrum in which the peak at 62 amu appears. Known peaks are labeled for reference.

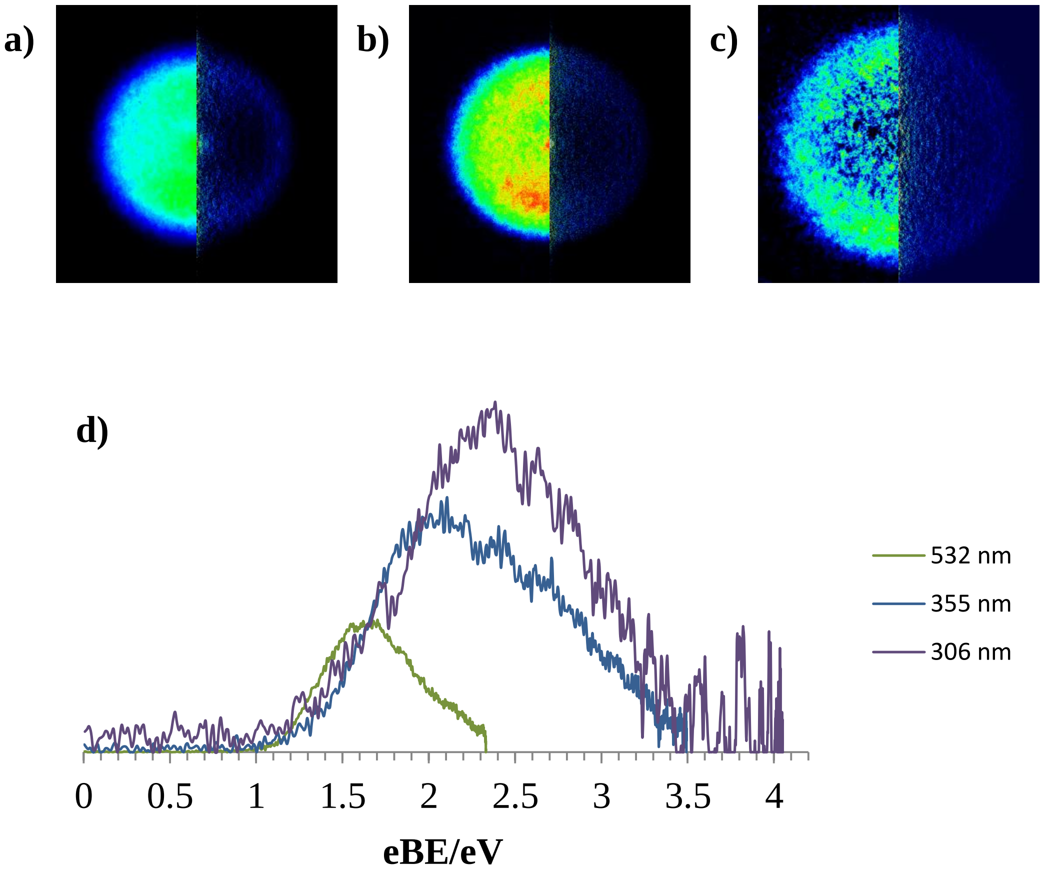

Figure 6.3. Raw photoelectron images (left) and inverse Abel transformed images (right) of the species at mass-to-charge 62 amu collected at a) 532 nm, b) 355 nm, and c) 306 nm, and d) corresponding photoelectron spectra.

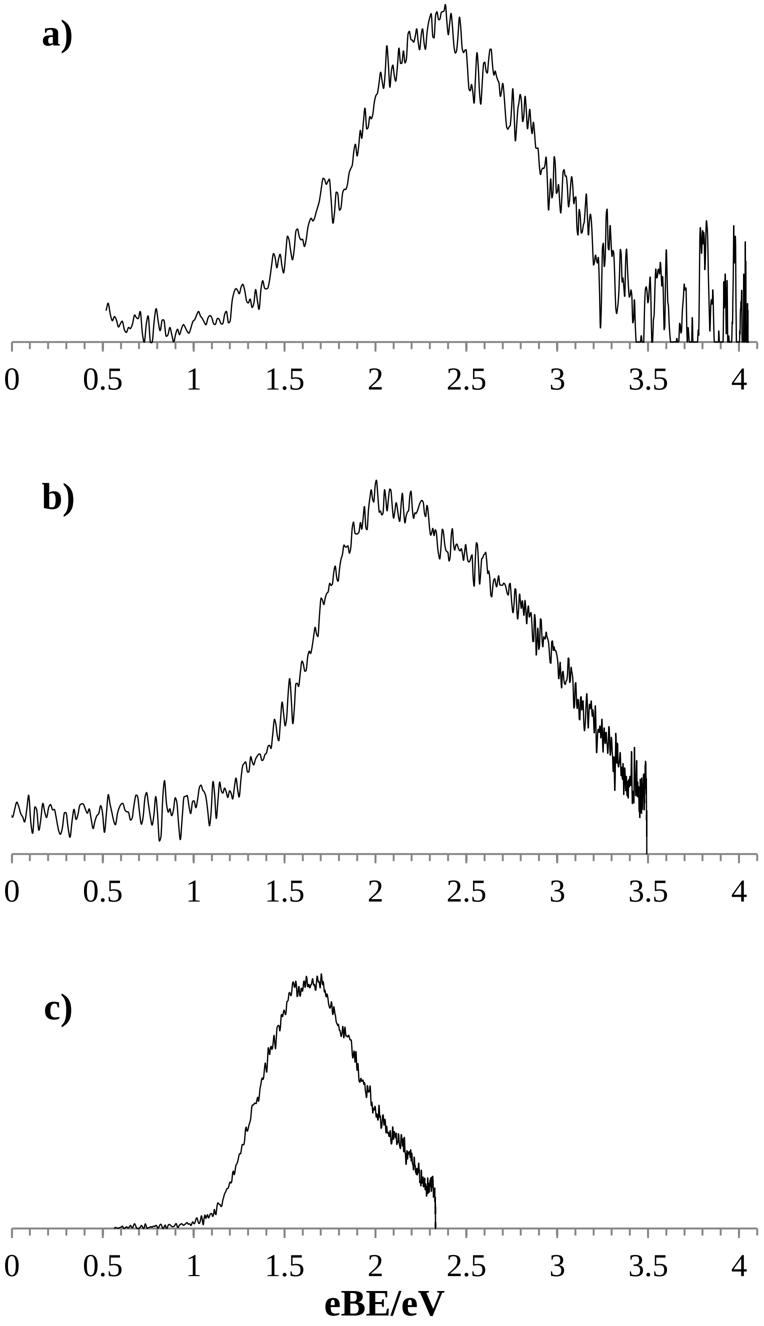

Figure 6.4. Photoelectron spectra of the species at mass-to-charge 62 amu at a) 306 nm, b) 355 nm, and c) 532 nm.

seeded in oxygen carrier gas. The mass spectrum for this experiment is shown in Figure 6.5. Residual methanol in the backing line resulted in both the original peak at 62 amu to remain, as well as opened the possibility for mixed hydrogen-deuterium species, either from isotope exchange, or clustering of CH_3OH- and CD_3OD-related species. New peaks were observed at mass-to-charge 65 amu, 66 amu, 67 amu, 68 amu, and 69 amu, with the peak at 67 amu the most intense.

Photoelectron signal could not be found for the peak at 69 amu, and the peak at 66 amu produced a photoelectron image consistent with that observed for $CH_3O_3^-$, as described in Chapter 5, but photoelectron images were collected of the other species at 306 nm. These are presented together in Figure 6.6, along with the original 62 amu spectrum and the spectrum collected at 64 amu, in which there was no indication of a deuterated species coincident with the expected O_4^- peak in the mass spectrum. The spectra collected at 65 amu and 68 amu appear to be clearly related to each other and to the original spectrum collected at 62 amu, but evidence of a second band appears in the spectrum collected at 67 amu. It is difficult to determine from these data if that second band is a real feature, or if it was a consequence of noise overlaying with the spectrum. The PADs for these new species were inconsistent with the original photoelectron images of the species observed at mass-to-charge 62 amu, having predominantly isotropic or slightly perpendicular anisotropy, making assigning them as a deuteration series of the peak at 62 amu impossible, despite the agreement of the spectra.

Unfortunately, before the CH_3OH components of the mass spectrum could be cleared from the apparatus, and further data collected on the deuterated species, the nozzle became clogged and required cleaning. A brown residue was removed from the

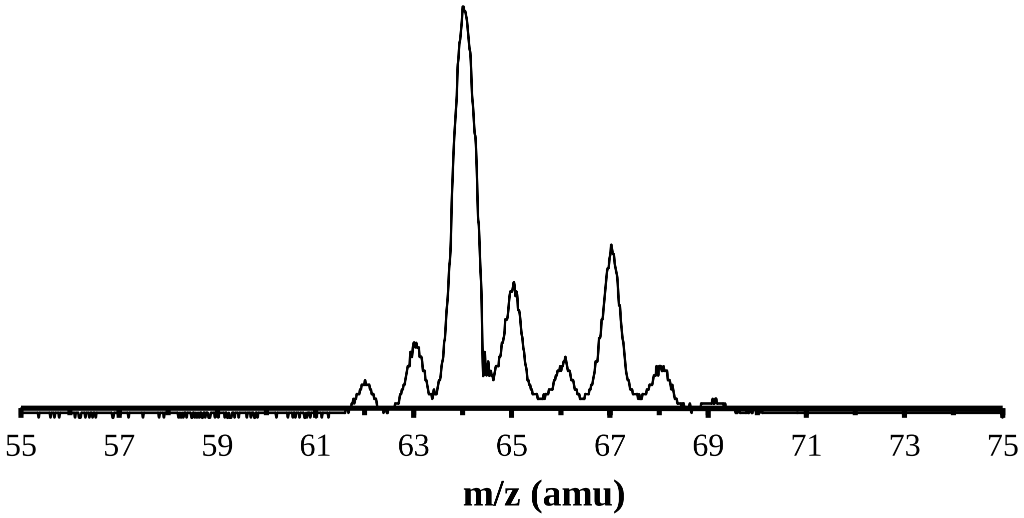

Figure 6.5. Mass spectrum of CD_3OD in O_2 focused on the mass region of interest. The peak at 65 amu, originally corresponding to HO_4^- increases considerably in size, and new peaks appear at 66 amu ($CD_3O_3^-$), 67 amu, 68 amu, and 69 amu.

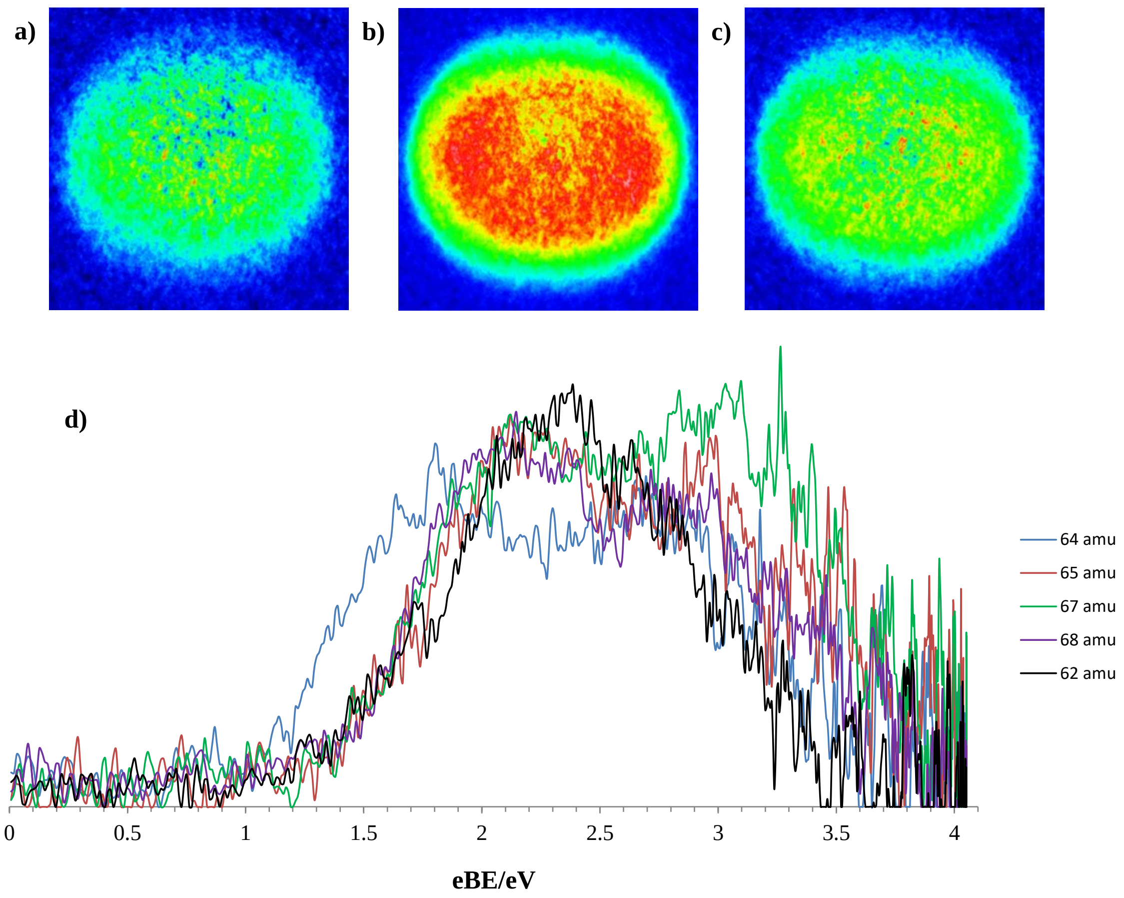

Figure 6.6. Photoelectron images collected at 306 nm of the species at m/z a) 65 amu, b) 67 amu, and c) 68 amu, and d) their corresponding photoelectron spectra, as well as the spectra at 64 amu (O_4^-) and 62 amu, for reference.

nozzle, and black soot from the carrier gas line. Upon starting the experiment again, neither the peak at 62 amu nor the series of deuterated species could be observed. Weak signal at 62 amu could be seen intermittently in future experiments, but photoelectron signal could not be found, and it is unclear what conditions favor its formation in the mass spectrum.

6.3. Future Directions

The work reported in this dissertation both inspires new chemical directions to pursue, and highlights the benefit of a significant change to the instrument. This section will explore both of these directions.

6.3.1. New Chemical Projects

I propose two avenues to expand on the systems studied in this work: a complete exploration of the superoxide adduct intermediates in the peroxone process, and the extension of the chemistry which produced $CH_3O_3^-$ to higher-mass species.

Peroxone Intermediates. The mechanism of the peroxone process, discussed briefly in Section 3.1.1., is proposed to involve in part the formation of superoxide adduct species as intermediates, described in part in the reactions:[57,58]

$$HO_2^- + O_3 \rightarrow O_2 + HO_3^- \tag{6.1a}$$

$$HO_3^- + H^+ \rightarrow H_2O_3 \tag{6.1b}$$

$$O_3 + HO^- \rightarrow HO_4^- \tag{6.2a}$$

$$O_2^- + HO_2 \rightarrow HO_4^- \tag{6.2b}$$

$$O_3 + HO_2^- \rightarrow HO_5^- \qquad (6.3)$$

There have been no experimental detections to date of any of HO_3^-, HO_4^-, or HO_5^-, though *trans*-HO_3 radicals have been studied in connection to chemistry in the interstellar medium,[94] and HO_4^+ has been studied by infrared dissociation spectroscopy.[95] Detection and study of the anions would be an important experimental step to support the computational work underpinning these proposed mechanisms. Additionally, the *cis*-HO_3 radical may be accessed by photoelectron spectroscopy through the *cis*-HO_3^- anion,[96] to inform the astrochemical search for the *cis* isomer of the radical, which is predicted to be stable by computational work.[97-100] Finally, successful gas-phase studies of these species could support the exploration of their potential roles in atmospheric chemistry.

As described in Section 6.2.1 above, each HO_3^- and HO_4^- have been observed in our mass spectrometer, and HO_4^- was briefly studied by photoelectron imaging, giving confidence to the viability of this project. Additionally, preliminary calculations have been completed using Gaussian09 at the CCSD level of theory with the aug-cc-pVDZ basis set to predict the EAs of the species observed in the mass spectrum, and these results are reported in Table 6.1. The calculated EAs for the *cis*- and *trans*-HO_3^- isomers are 1.3158 eV and 1.0741 eV, respectively, while the EAs for the pseudo-ring structure HO_4^- is 1.9680 eV (roughly consistent with the apparent onset of the spectrum in Figure 6.1, near 2 eV), and the non-ring "*trans*" isomer is 1.3421 eV.

If a reliable ion generation method is discovered for these superoxide adduct species, exploring the effects on their photoelectron images by water solvation would allow this work to be further connected to the study of the peroxone process, as well.

Molecule	**EA/eV**
cis-HO_3^-	1.3158
trans-HO_3^-	1.0741
HO_4^- (ring)	1.9680
HO_4^- *("trans")*	1.3421

Table 6.1. *Ab initio* calculated electron affinities for two isomers of each HO_3^- and HO_4^- using Gaussian09 at the CCSD level of theory with the aug-cc-pVDZ basis set.

Previous computational work on HO_4^- suggests drastic changes in geometry upon water solvation,[57] from a planar, pseudo-five-member ring structure of the gas-phase anion, to a various puckered hydrogen-bonded dimer structures with a single water molecule, to solution-phase structures in which the molecule is more "stretched" than ring, to maximize interactions between the oxygen atoms and the solvent. Exploring these interactions through both the solvation energy and the polarization of the MOs as reflected in the PADs would be illuminating.

Further Methoxide-Oxygen Chemistry and Clusters. This work did not explore higher-mass species produced from the reaction of methoxide and oxygen, whether they be solvated or new covalent molecules. Searching the mass spectrum for species such as $CH_3O_4^-$ and $CH_3O_5^-$, and then studying these species by photoelectron imaging spectroscopy could provide some insight into the identity of $CH_3O_3^-$, as well as further elucidating the range of chemistry possible in the reaction of CH_3O^- and O_2.

6.3.2. Modifications to the Apparatus: High Resolution Photoelectron Imaging

In the work on the formate anion described in Chapter 4, it was noted that the existing experimental resolution was insufficient to distinguish electronic bands from each other in the congested spectrum. If a proper study on the photoelectron anisotropy parameters is to be completed on this species, the experimental resolution will need to be improved considerably. Additionally, some of the projects proposed in Section 6.3.1 above will benefit from improved resolution, especially in identifying both *trans*- and *cis*-HO_3^- if both contribute to the spectrum.

Two key adjustments will be necessary to achieve improved spectral resolution. The first is identifying the cause of the VMI field distortions and correcting it. The most likely possible sources are a deterioration of the μ-metal shielding, which protects the VMI assembly from external magnetic fields or a breakdown in the separation of the VMI electrodes. Each of these possibilities will be explored, among others, to repair the photoelectron imaging assembly.

The resolution gain from this correction will likely be small, however, and a change to the apparatus will be necessary to improve the resolution enough to properly study CHO_2^- and other ions with congested spectra. This can be achieved by moving the VMI from its current perpendicular position to one coaxial with the ion beam, removing the broadening of the spectrum due to the velocity spread of the ion packet.[80] This setup is described in the schematic in Figure 6.7. The coaxial setup also allows the position of the interaction region to be optimized, using the MCP, phosphor screen, and CCD camera to detect the impact position of the ions and adjust their position in the VMI using the ion optics to best center the ion packet and optimize the focus of the photoelectron image on the detector. In order to preserve the PAD information, it will also be necessary to rotate the laser polarization direction to be perpendicular to the floor rather than parallel to it.

Further resolution gains can be made through the use of centroiding, in which the detection software identifies the center of each photoelectron event to sub-pixel resolution.[80] However, this may require the purchase of a new CCD camera, as the software which executes the centroiding process can be taxing to the computer, and the current camera hardware is only compatible with Windows XP and older operating systems, severely limiting the available processors and processing power.

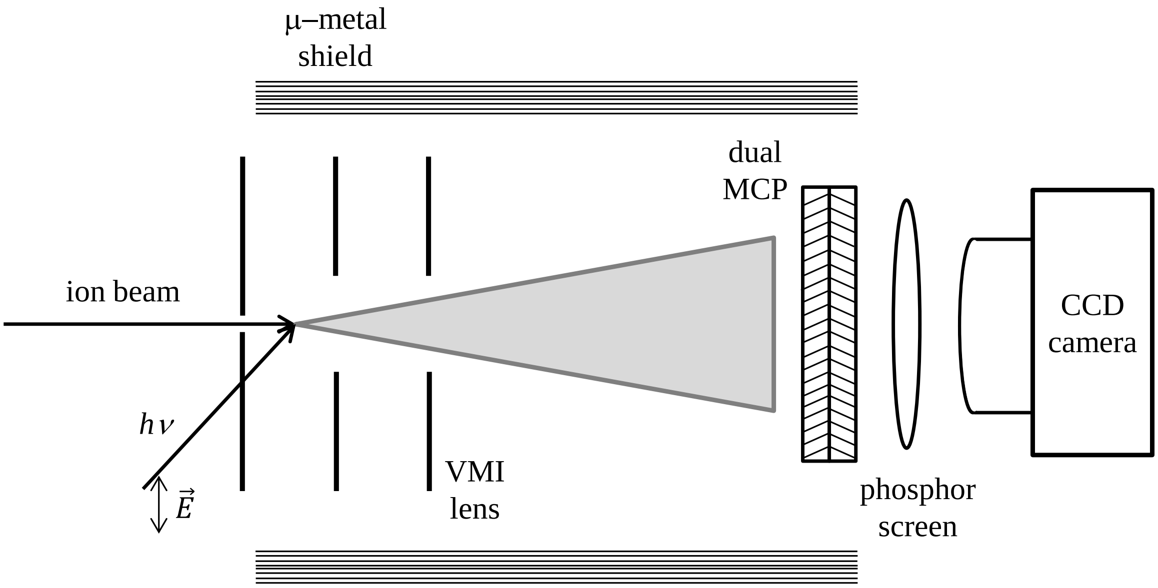

Figure 6.7. Line schematic of the proposed in-line VMI detector to improve the experimental resolution.

A combination of a perfectly-focused coaxial VMI and centroiding can achieve resolution on the order of 3 meV for electrons with kinetic energy of about 1 eV, as reported by the Gibson group, a considerable upgrade over the current optimum experimental resolution of ~20 meV for slow (< 1eV) photoelectrons, and ~120 meV for fast (> 2 eV) photoelectrons reported for this work in Chapter 2.[80]

6.4. Final Word

While some questions remain about the work reported in this dissertation, we have successfully achieved two key research goals: deepened our understanding of PADs in the context each of molecular symmetry arguments, and the quantitative Generalized Mixed Character Model; and found evidence of previously unexplored chemistry between methoxide and oxygen. This latter point, in particular, begets further exploration and inspires future research projects to find answers to the questions this dissertation raised, in particular in Chapters 4 and 5. Methanol seeded in oxygen proved a reliable source of the formate anion, and the unexpected and unexplained species $CH_3O_3^-$ was observed. Pursuing this thread may provide new insights into the role of alkoxides in the atmosphere.

REFERENCES

(1) Orlando, J. J.; Tyndall, G. S. *Chemical Reviews* **2003**, *103*, 4657-4689.

(2) Atkinson, R.; Baulch, D. L.; Cox, R. A.; Crowley, J. N.; Hampson, R. F.; Hynes, R. G.; Jenkin, M. E.; Rossi, M. J.; Troe, J. *Atmospheric Chemistry and Physics* **2006**, *6*, 3625-4055.

(3) Jenkin, M. E.; Clemistshaw, K. C. *Atmospheric Environment* **2000**, *34*, 2499-2527.

(4) Lim, Y. B.; Ziemann, P. J. *Environmental Science and Technology* **2005**, *39*, 9229-9236.

(5) Lin, H.-x.; Liang, H.-l.; Chen, G.-h.; Gu, F.-l.; Liu, W.-g.; Ni, S.-f. *The Journal of Physical Chemsitry A* **2012**, *116*, 11656-11667.

(6) Monks, P. S. *Chemical Society Reviews* **2004**, *34*, 376-395.

(7) Zellner, R. *Journal de Chimie Physique et de Physico-Chimie Biologique* **1987**, *84*, 403-407.

(8) Mallick, S.; Kumar, A.; Kumar, P. *Physical Chemistry Chemical Physics* **2019**, *21*, 6559-6565.

(9) Midey, A.; Dotan, I.; Seeley, J. V.; Viggiano, A. A. *International Journal of Mass Spectrometry* **2009**, *280*, 6-11.

(10) Einstein, A. *Ann. Physik* **1905**, *17*, 132-148.

(11) Ervin, K. M.; Lineberger, W. C. In *Advances in Gas Phase Ion Chemistry*; Adams, N. G., Babcock, L. M., Eds.; JAI Press: Greenwich, **1992**; Vol. 1, p 121-166.

(12) Reid, K. L. *Annual Review of Physical Chemistry* **2003**, *54*, 397-424.

(13) Sanov, A. *Annual Review of Physical Chemistry* **2014**, *65*, 341-363.

(14) Chandler, D. W.; Houston, P. L. *Journal of Chemical Physics* **1987**, *87*, 1445-1447.

(15) Eppink, A. T. J. B.; Parker, D. H. *Review of Scientific Instruments* **1997**, *68*, 3477-3484.

(16) Parker, D. H.; Eppink, A. T. J. B. *Journal Of Chemical Physics* **1997**, *107*, 2357-2362.

(17) Suzuki, T. *Annual Review of Physical Chemistry* **2006**, *57*, 555-592.

(18) Ashfold, M. N. R.; Nahler, N. H.; Orr-Ewing, A. J.; Vieuxmaire, O. P. J.; Toomes, R. L.; Kitsopoulos, T. N.; Garcia, I. A.; Chestakov, D. A.; Wu, S. M.; Parker, D. H. *Physical Chemistry Chemical Physics* **2006**, *8*, 26-53.

(19) Heck, A. J. R.; Chandler, D. W. *Annual Review of Physical Chemistry* **1995**, *46*, 335-372.

(20) Davies, J. A.; Continetti, R. E.; Chandler, D. W.; Hayden, C. C. *Physical Review Letters* **2000**, *84*, 5983-5986.

(21) Houston, P. L. *Accounts Of Chemical Research* **1995**, *28*, 453-460.

(22) Alconcel, L. S.; Deyerl, H. J.; Continetti, R. E. *Journal of the American Chemical Society* **2001**, *123*, 12675.

(23) Surber, E.; Ananthavel, S. P.; Sanov, A. *Journal of Chemical Physics* **2002**, *116*, 1920-1929.

(24) Hanstorp, D.; Bengtsson, C.; Larson, D. J. *Physical Review A* **1989**, *40*, 670-675.

(25) Zare, R. N. *Molecular Photochemistry* **1972**, *4*, 1-37.

(26) Bethe, H. A.; Salpeter, E. E. *Quantum Mechanics of One- and Two-Electron Atoms*; Springer-Verlag; Academic Press Inc.: Berlin; New York, **1957**.

(27) Cooper, J.; Zare, R. N. *J. Chem. Phys.* **1968**, *48*, 942-943.

(28) Cooper, J.; Zare, R. N. *J. Chem. Phys.* **1968**, *49*, 4252.

(29) Wigner, E. P. *Physical Review* **1948**, *73*, 1002-1009.

(30) Fano; Dill, D. *Physical Review A* **1972**, *6*, 185-192.

(31) Park, H.; Zare, R. N. *Journal of Chemical Physics* **1996**, *104*, 4554-4567.

(32) Reed, K. J.; Zimmerman, A. H.; Andersen, H. C.; Brauman, J. I. *Journal of Chemical Physics* **1976**, *64*, 1368-1375.

(33) Akin, F. A.; Schirra, L. K.; Sanov, A. *Journal of Physical Chemistry A* **2006**, *110*, 8031-8036.

(34) Van Duzor, M.; Mbaiwa, F.; Wei, J.; Singh, T.; Mabbs, R.; Sanov, A.; Cavanagh, S. J.; Gibson, S. T.; Lewis, B. R.; Gascooke, J. R. *Journal of Chemical Physics* **2010**, *133*, 174311.

(35) Oana, C. M.; Krylov, A. I. *Journal of Chemical Physics* **2009**, *131*, 124114.

(36) Surber, E.; Mabbs, R.; Sanov, A. *J. Phys. Chem. A* **2003**, *107*, 8215-8224.

(37) Grumbling, E. R.; Sanov, A. *Journal of Chemical Physics* **2011**, *135*, 164302.

(38) Grumbling, E. R.; Sanov, A. *Journal of Chemical Physics* **2011**, *135*, 164301.

(39) Culberson, L. M.; Blackstone, C. C.; Sanov, A. *Journal of Physical Chemistry A* **2013**, *117*, 11760-11765.

(40) Culberson, L. M.; Blackstone, C. C.; Wallace, A. A.; Sanov, A. *Journal of Physical Chemistry A* **2015**, *119*, 9770-9777.

(41) Culberson, L. M.; Blackstone, C. C.; Wysocki, R.; Sanov, A. *Physical Chemistry Chemical Physics* **2014**, *16*, 527-532.

(42) Culberson, L. M.; Sanov, A. *Journal of Chemical Physics* **2011**, *134*, 204306.

(43) Sanov, A.; Grumbling, E. R.; Goebbert, D. J.; Culberson, L. M. *Journal of Chemical Physics* **2013**, *138*, 054311.

(44) Khuseynov, D.; Blackstone, C. C.; Culberson, L. M.; Sanov, A. *Journal of Chemical Physics* **2014**, *141*, 124312.

(45) Culberson, L. M.; Wallace, A. A.; Blackstone, C. C.; Khuseynov, D.; Sanov, A. *Physical Chemistry Chemical Physics* **2014**, *16*, 3964-3972.

(46) Culberson, L. M. Ph.D. dissertation, University of Arizona, **2013**.

(47) Mabbs, R.; Surber, E.; Sanov, A. *Analyst* **2003**, *128*, 765-772.

(48) Johnson, M. A.; Lineberger, W. C. In *Techniques for the Study of Ion Molecule Reactions*; Farrar, J. M., Saunders, W. H., Eds.; Wiley: New York, **1988**, p 591-635.

(49) Klots, C. E. *J. Chem. Phys.* **1985**, *83*, 5854.

(50) Klots, C. E.; Compton, R. N. *Journal of Chemical Physics* **1978**, *69*, 1636-1643.

(51) Alexander, M. L.; Levinger, N. E.; Johnson, M. A.; Ray, D.; Lineberger, W. C. *Journal of Chemical Physics* **1988**, *88*, 6200-10.

(52) Wiley, W. C.; McLaren, I. H. *Review of Scientific Instruments* **1955**, *26*, 1150.

(53) Johnson, M. A.; Alexander, M. L.; Lineberger, W. C. *Chemical Physics Letters* **1984**, *112*, 285-290.

(54) Bordas, C.; Paulig, F.; Helm, H.; Huestis, D. L. *Review of Scientific Instruments* **1996**, *67*, 2257-2268.

(55) Pichugin, K. Ph.D. dissertation, University of Arizona, **2010**.

(56) Dribinski, V.; Ossadtchi, A.; Mandelshtam, V. A.; Reisler, H. *Review of Scientific Instruments* **2002**, *73*, 2634-2642.

(57) Anglada, J. M.; Torrent-Sucarrat, M.; Ruiz-Lopez, M. F.; Martins-Costa, M. *Chemistry European Journal* **2012**, *18*, 135435-13445.

(58) Merenyi, G.; Lind, J.; Naumov, S.; von Sonntag, C. *Chemistry European Journal* **2010**, *16*, 1372-1377.

(59) Duncianu, M.; Lahib, A.; Tomas, A.; Stevens, P. S.; Dusanter, S. *Atmospheric Environment* **2020**, *222*.

(60) Clifford, E. P.; Wenthold, P. G.; Gareyev, R.; Lineberger, W. C.; DePuy, C. H.; Bierbaum, V. M.; Ellison, G. B. *Journal of Chemical Physics* **1998**, *109*, 10293-10310.

(61) Oakes, J. M.; Harding, L. B.; Ellison, B. G. *Journal of Chemical Physics* **1985**, *83*, 5400-5406.

(62) Jacox, M. E. *Journal of Physical and Chemical Reference Data* **1994**, 1-461.

(63) Tuckett, R. P.; Freedman, P. A.; Jones, W. J. *Molecular Physics* **1979**, *37*, 379-401.

(64) Becker, K. H.; Fink, E. H.; Langen, P.; Schurath, U. *Journal of Chemical Physics* **1974**, *60*, 4623-4625.

(65) Gibson, S.; Hickstein, D. D.; Yurchak, R.; Ryanzanov, M.; Dhrubajyoti, D.; Gilbert, S.; GitHub: **2019**.

(66) Gascooke, J. R.; Gibson, S. T.; Lawrance, W. D. *Journal of Chemical Physics* **2017**, *147*.

(67) Landau, L. D.; Lifshitz, E. M. *Quantum Mechanics: Nonrelativistic Theory*; 3rd ed. ed.; Pergamon Press: Oxford, **1977**.

(68) Cohen-Tannoudji, C.; Diu, B.; Laloë, F. *Quantum Mechanics*; John Wiley & Sons: New York, London, Sydney, Toronto, **1977**; Vol. 2.

(69) Frisch, M. J.; Trucks, G. W.; Schlegel, H. B.; Scuseria, G. E.; Robb, M. A.; Cheeseman, J. R.; Scalmani, G.; Barone, V.; Mennucci, B.; Petersson, G. A.; Nakatsuji, H.; Caricato, M.; Li, X.; Hratchian, H. P.; Izmaylov, A. F.; Bloino, J.; Zheng, G.; Sonnenberg, J. L.; Hada, M.; Ehara, M.; Toyota, K.; Fukuda, R.; Hasegawa, J.; Ishida, M.; Nakajima, T.; Honda, Y.; Kitao, O.; Nakai, H.; Vreven, T.; Montgomery, J., J. A.; Peralta, J. E.; Ogliaro, F.; Bearpark, M.; Heyd, J. J.; Brothers, E.; Kudin, K. N.; Staroverov, V. N.; Kobayashi, R.; Normand, J.; Raghavachari, K.; Rendell, A.; Burant, J. C.; Iyengar, S. S.; Tomasi, J.; Cossi, M.; Rega, N.; Millam, N. J.; Klene, M.; Knox, J. E.; Cross, J. B.; Bakken, V.; Adamo, C.; Jaramillo, J.; Gomperts, R.; Stratmann, R. E.; Yazyev, O.; Austin, A. J.; Cammi, R.; Pomelli, C.; Ochterski, J. W.; Martin, R. L.; Morokuma, K.; Zakrzewski, V. G.; Voth, G. A.; Salvador, P.; Dannenberg, J. J.;

Dapprich, S.; Daniels, A. D.; Farkas, Ö.; Foresman, J. B.; Ortiz, J. V.; Cioslowski, J.; Fox, D. J.; Revision A.1 ed.; Gaussian, Inc.: Wallingford, CT, **2009**.

(70) Bradley, K. S.; Schatz, G. C. *Journal of Chemical Physics* **1997**, *106*, 8464-8472.

(71) Yu, H.-G.; Muckerman, J. T.; Sears, T. J. *Chemical Physics Letters* **2001**, *349*, 547-554.

(72) Schatz, G. C.; Fitzcharles, M. S. *Faraday Discussions* **1987**, *84*, 359-369.

(73) Duncan, T. V.; Miller, C. E. *Journal of Chemical Physics* **2000**, *113*, 5138-5140.

(74) Song, X.; Li, J.; Hou, H.; Wang, B. *Journal of Chemical Physics* **2006**, *125*.

(75) Ray, A. W.; Shen, B. B.; Poad, B., L.J.; Continetti, R. E. *Chemical Physics Letters* **2014**, *592*, 30-35.

(76) Ma, J.; Guo, H. *Chemical Physics Letters* **2011**, *511*, 193-195.

(77) Garand, E.; Klein, K.; Stanton, J. F.; Zhou, J.; Yacovitch, T. I.; Neumark, D. M. *Journal of Physical Chemistry A* **2010**, *114*, 1374-1383.

(78) Kim, E. H.; Bradforth, S. E.; Arnold, D. W.; Metz, R. B. *Journal of Chemical Physics* **1995**, *103*, 7801-7814.

(79) Zou, L.; Li, J.; Wang, H.; Ma, J.; Guo, H. *Journal of Physical Chemistry A* **2015**, *119*, 7316-7324.

(80) Cavanagh, S. J.; Gibson, S. T.; Gale, M. N.; Dedman, C. J.; Roberts, E. H.; Lewis, B. R. *Physical Review A* **2007**, *76*, 052708.

(81) Shao, Y. H.; Gan, Z. T.; Epifanovsky, E.; Gilbert, A. T. B.; Wormit, M.; Kussmann, J.; Lange, A. W.; Behn, A.; Deng, J.; Feng, X. T.; Ghosh, D.; Goldey, M.; Horn, P. R.; Jacobson, L. D.; Kaliman, I.; Khaliullin, R. Z.; Kus, T.; Landau, A.; Liu, J.; Proynov, E. I.; Rhee, Y. M.; Richard, R. M.; Rohrdanz, M. A.; Steele, R. P.; Sundstrom, E. J.; Woodcock, H. L.; Zimmerman, P. M.; Zuev, D.; Albrecht, B.; Alguire, E.; Austin, B.; Beran, G. J. O.; Bernard, Y. A.; Berquist, E.; Brandhorst, K.; Bravaya, K. B.; Brown, S. T.; Casanova, D.; Chang, C. M.; Chen, Y. Q.; Chien, S. H.; Closser, K. D.; Crittenden, D. L.; Diedenhofen, M.; DiStasio, R. A.; Do, H.; Dutoi, A. D.; Edgar, R. G.; Fatehi, S.; Fusti-Molnar, L.; Ghysels, A.; Golubeva-Zadorozhnaya, A.; Gomes, J.; Hanson-Heine, M. W. D.; Harbach, P. H. P.; Hauser, A. W.; Hohenstein, E. G.; Holden, Z. C.; Jagau, T. C.; Ji, H. J.; Kaduk, B.; Khistyaev, K.; Kim, J.; Kim, J.; King, R. A.; Klunzinger, P.; Kosenkov, D.; Kowalczyk, T.; Krauter, C. M.; Lao, K. U.; Laurent, A. D.; Lawler, K. V.; Levchenko, S. V.; Lin, C. Y.; Liu, F.; Livshits, E.; Lochan, R. C.; Luenser, A.; Manohar, P.; Manzer, S. F.; Mao, S. P.; Mardirossian, N.; Marenich, A. V.; Maurer, S. A.; Mayhall, N. J.; Neuscamman, E.; Oana, C. M.; Olivares-Amaya, R.; O'Neill, D. P.; Parkhill, J. A.; Perrine, T. M.; Peverati, R.; Prociuk, A.; Rehn, D. R.; Rosta, E.; Russ, N. J.; Sharada, S. M.; Sharma, S.; Small, D. W.; Sodt, A. *Molecular Physics* **2015**, *113*, 184-215.

(82) Krylov, A. I. *Annual Review of Physical Chemistry* **2008**, *59*, 433-462.

(83) Goebbert, D. J.; Sanov, A. *Journal of Chemical Physics* **2009**, *131*, 104308.

(84) Markovich, G.; Perera, L.; Berkowitz, M. L.; Cheshnovsky, O. *Journal Of Chemical Physics* **1996**, *105*, 2675-2685.

(85) Nee, M. J.; Osterwalder, A.; Zhou, J.; Neumark, D. M. *Journal of Chemical Physics* **2006**, *125*, 014306.

(86) Weichman, M. L.; Cheng, L.; Kim, J. B.; Stanton, J. F.; Neumark, D. M. *Journal of Chemical Physics* **2017**, *146*, 224309.

(87) Markovich, G.; Pollack, S.; Giniger, R.; Cheshnovsky, O. *Journal Of Chemical Physics* **1994**, *101*, 9344-9353.

(88) Arnold, D. W.; Xu, C. S.; Neumark, D. M. *Journal Of Chemical Physics* **1995**, *102*, 6088-6099.

(89) Johnson, C. J.; Harding, M. E.; Poad, B., L.J.; Stanton, J. F.; Continetti, R. E. *Journal of the American Chemical Society* **2011**, *133*, 19606-19609.

(90) Wang, J.; Li, J.; Ma, J.; Guo, H. *Journal of Chemical Physics* **2014**, *140*.

(91) Wang, X.-B.; Jagoda-Cwiklik, B.; Chi, C.; Xing, X.-P.; Zhou, M.; Jungwirth, P.; Wang, L.-S. *Chemical Physics Letters* **2009**, *477*, 41-44.

(92) Bohm, S.; Antipova, D.; Kuthan, J. *International Journal of Quantum Chemistry* **1995**, *60*, 649-655.

(93) Bohm, S.; Senf, I.; Schadler, H.; Kuthan, J. *Journal of Molecular Structure-Theochem* **1992**, *85*, 73-82.

(94) Zou, L.; Hays, B. M.; Widicu Weaver, S. L. *Journal of Physical Chemistry A* **2016**, *120*, 657-667.

(95) Franke, P. R.; Duncan, M. A.; Douberly, G. A. *Journal of Chemical Physics* **2020**, *152*.

(96) Varandas, A. J. C. *Physical Chemistry Chemical Physics* **2010**, *16*, 16997-17007.

(97) Trabelsi, T.; Francisco, J. S. *Journal of Chemical Physics* **2020**, *152*, 064304-064311.

(98) Suma, K.; Sumiyoshi, Y.; Endo, Y. *Journal of Chemical Physics* **2013**, *139*, 094301-094307.

(99) Hu, X.; Zuo, J.; Xie, C.; Dawes, R.; Guo, H.; Xie, D. *Physical Chemistry Chemical Physics* **2019**, *21*, 13766-13775.

(100) Zhou, Y.; Hu, H.; Li, L.; Hou, H.; Wang, B. *Computational and Theoretical Chemistry* **2013**, *1026*, 24-30.